

Modeling and Performance Evaluation of Avalanche Detector Structures for Low Dose Medical X-ray Imaging

Salman Moazzem Arnab

A Thesis
In the Department
of
Electrical and Computer Engineering

Presented in Partial Fulfillment of the Requirements
For the Degree of
Doctor of Philosophy (Electrical and Computer Engineering) at
Concordia University
Montréal, Quebec, Canada

November 2019

© Salman Moazzem Arnab, 2019

CONCORDIA UNIVERSITY
SCHOOL OF GRADUATE STUDIES

This is to certify that the thesis prepared

By: **Salman Moazzem Arnab**

Entitled: **Modelling and Performance Evaluation of Avalanche Detector Structures for Low Dose Medical X-ray Imaging**

and submitted in partial fulfillment of the requirements for the degree of

Doctor Of Philosophy (Electrical and Computer Engineering)

complies with the regulations of the University and meets the accepted standards with respect to originality and quality.

Signed by the final examining committee:

_____ Chair
Dr. Roch Glitho

_____ External Examiner
Dr. Alla Reznik

_____ External to Program
Dr. Saifur Rahaman

_____ Examiner
Dr. Hassan Rivaz

_____ Examiner
Dr. Steve Shih

_____ Thesis Supervisor
Dr. M. Zahangir Kabir

Approved by _____
Dr. Rastko Selmic, Graduate Program Director

January 24, 2020

Dr. Amir Asif, Dean
Gina Cody School of Engineering & Computer Science

ABSTRACT

Modeling and Performance Evaluation of Avalanche Detector Structures for Low Dose Medical X-ray Imaging

Salman Moazzem Arnab, Ph.D.
Concordia University, 2019

The flat-panel x-ray detectors based on large area integrated circuit called active matrix array ensure excellent image quality and provide wide dynamic range. As a result, active matrix flat panel imagers (AMFPIs) are now commercially available for chest radiography and mammography. However, at low level exposures, most of the AMFPIs are not quantum noise limited due to the electronic noise of the readout circuitry. Therefore, AMFPIs are not fully commercialized for x-ray fluoroscopy (used for interventional procedures and deployment of endovascular devices) which requires maintaining a very low x-ray exposure. An active research is underway to make AMFPIs quantum noise limited at fluoroscopic exposure level. This work investigates the feasibility of avalanche gain as a solution.

At high electric field, avalanche multiplication of charge carrier improves the signal strength to overcome the effects of electronic noise in both direct and indirect conversion x-ray detectors. Indirect conversion detectors are suitable for the avalanche multiplication. It is because the gain fluctuation is minimum since the x-ray absorption and electric charge collection occur in two separate layers. However, in indirect conversion detectors, the image resolution in terms of modulation transfer function (MTF) deteriorates due to depth dependent x-ray absorption (Lubberts effect) and omni-directional propagation of light photons in the phosphor. In this research work, a cascaded linear-system model is proposed to calculate the image quality of CsI-based indirect conversion a-Se avalanche x-ray detectors in terms of spatial frequency dependent detective quantum efficiency (DQE). The depth dependent MTF and noise power spectrum (NPS) are modeled by incorporating the Lubberts effect. The theoretical model also considers MTF due to *K*-fluorescence reabsorption. The model is then compared with experimentally determined $DQE(f)$ and shows a better fit than previously published models.

On the other hand, direct conversion detectors show a better performance in terms of image resolution as the x-ray photons are directly converted into electron and hole pairs. However, the

direct conversion detectors are still vulnerable to the electronic noise at low exposures. Utilization of mesh electrode in order to separate the x-ray absorption and gain region has been proposed in the literature to reduce the avalanche gain fluctuation in direct conversion detectors. This work includes a cascaded linear-system model to calculate the $DQE(f)$ of an a-Se based direct conversion avalanche x-ray detector. The proposed model evaluates charge collection efficiency using the Ramo-Shockley theorem and the actual weighting potential of an individual pixel. A 2-Dimensional simulation is performed to calculate the actual weighting potential in the presence of a mesh electrode. The optimal design parameters and operational condition for a-Se based direct conversion multilayer avalanche x-ray detectors are described in this work.

In order to ease the fabrication process and eliminate the need of applying two different voltages to the aforementioned mesh electrode based direct conversion avalanche detector, a novel structure for direct conversion avalanche detector is proposed. The proposed structure contains a hole trapping layer instead of a mesh electrode to separate the absorption layer from the gain region. A numerical model is developed using Semiconductor Module of COMSOL Multiphysics to analyze the device performance. The electric field profile as a function of various device parameters is calculated. A detailed analysis on the transient behavior of the dark current in presence of blocking and trapping layers is performed. A modified cascaded linear-system model that considers the effect of reabsorption of K -fluorescent x-rays, carrier trapping in different layers and avalanche multiplication of charge carrier is used to calculate the $DQE(f)$ and the MTF of the proposed structure. The $DQE(f)$ of the proposed structure is then compared with published experimental results of a commercially available detector at low x-ray exposures (e.g., exposures used in tomosynthesis).

The relative performance of these detector structures influences their clinical effectiveness. Therefore, a comparison of the performance of these detectors for different x-ray imaging modalities is also presented in this research work.

ACKNOWLEDGEMENTS

I would like to express my earnest gratitude to my research supervisor Dr. M. Zahangir Kabir for his continuous support, guidance, and financial assistance. His door was always open for me and he always had the time to attend queries and requests. Without his help and support, completing this work would not have been possible.

I would like to express my profound gratitude to all my family members who have supported me throughout my years of study. I am grateful to them for providing me with their unfailing supports.

I am also thankful to my friend Oussama and Anthony for helping me with simulations. I am indebted to my friends, Kaveh, Mahsa, Parsoua, Anthony, Ingrid, Pouya, Golia, Arshi and Mehran who have helped me on numerous occasions to complete this work. They were always there to provide joyful distraction to rest my mind outside of my research work. I would also like to thank Mithun Roy for the meaningful discussions and the other members of my research group.

My sincere thanks to my wife, Kritee for supporting me through thick and thin over the past years.

TABLE OF CONTENTS

LIST OF FIGURES	ix
LIST OF TABLES	xiii
LIST OF ABBREVIATIONS	xiv
LIST OF SYMBOLS	xvii
Chapter 1	1
Introduction	
1.1 Radiological Imaging Methods	3
1.2 Active Matrix Flat Panel Imagers	6
1.2.1 Direct Conversion Detector	10
1.2.2 Indirect Conversion Detector	12
1.3 AMFPI for Fluoroscopy	14
1.4 Requirements of Radiographic and Fluoroscopic Imaging Systems	16
1.5 Electronic Noise	17
1.6 Possible Solutions to Overcome Electronic Noise	19
1.6.1 Active Pixel Sensor Based X-Ray Detector	20
1.6.2 High Gain Photoconductors	22
1.6.3 Avalanche Gain	25
1.7 Research Objective	28
1.7.1 Imaging Performance of Amorphous Selenium Based Indirect Conversion Avalanche X-Ray Detector	28
1.7.2 Charge Trapping in Direct Conversion Avalanche Detector	30
1.7.3 Novel Amorphous Selenium Avalanche Detector	31
1.8 Thesis Outline	32
Chapter 2	33
Background Theory	
2.1 X-Ray Spectra from X-Ray Tube	33
2.2 X-Ray Interaction in a-Se And CsI	36
2.3 Electron and Hole Pair Creation Energy (W_{\pm})	37
2.3.1 W_{\pm} In Photoconductors	37
2.3.2 W_{\pm} In Scintillators Or Phosphors	40

2.4 Impact Ionization	41
2.5 Shockley-Ramo Theorem	42
2.6 Dark Current	45
2.7 Modulation Transfer Function	48
2.8 Noise Power Spectrum	52
2.9 Detective Quantum Efficiency	54
Chapter 3	56
Impact of Lubberts Effect on Amorphous Selenium Indirect Conversion Avalanche Detector for Medical X-Ray Imaging	
3.1 Introduction	57
3.2 Structure of Indirect Conversion Avalanche X-Ray Detector	59
3.3 Theory	60
3.3.1 MTF Due to <i>K</i> -Fluorescence Reabsorption	61
3.3.2 MTF Due to Optical Scattering with Lubberts Effect	63
3.3.3 Signal and Noise Propagation	64
3.3.4 X-Ray Photon Attenuation (Selection)	67
3.3.5 Conversion Gain	67
3.3.6 Quantum Yield	68
3.3.7 Avalanche Gain	68
3.3.8 DQE Calculation	69
3.4 Results And Discussion	71
3.5 Summary	79
Chapter 4	81
Impact of Charge Carrier Trapping on Amorphous Selenium Direct Conversion Avalanche X-Ray Detectors	
4.1 Introduction	82
4.2 Structure of Direct-Conversion Multilayer Avalanche X-Ray Detector with Grid Electrode	83
4.3 Theory	85
4.3.1 Signal and Noise Propagation	85
4.3.2 Mathematical Models for Stages	88
4.3.3 Detective Quantum Efficiency (DQE)	95
4.4 Results and Discussion	97

4.5 Summary.....	105
Chapter 5.....	106
A Novel Amorphous Selenium Avalanche Detector Structure for Low Dose Medical X-Ray Imaging	
5.1 Introduction	107
5.2 Structure of Direct-Conversion Multilayer Avalanche X-Ray Detector with Trapping Layer.....	110
5.3 Modeling by Numerical Calculations.....	112
5.3.1 Carrier Injection.....	113
5.3.2 Carrier Trapping in Different Layers.....	114
5.3.3 Electric Field Profile.....	116
5.3.4 Avalanche Gain.....	116
5.3.5 Blurring Due to Charge Carrier Trapping.....	117
5.4 Cascaded Linear System Model	118
5.5 Results And Discussion.....	120
5.6 Summary.....	130
Chapter 6.....	131
Comparison between Different Detector Structures	
6.1 Performance Comparison of Detectors for Fluoroscopic Applications.....	133
6.2 Performance Comparison of Detectors for Tomosynthesis	138
6.3 Summary.....	142
Chapter 7.....	143
Conclusions, Contributions and Future Work	
7.1 Conclusions	143
7.1.1 Effect of Depth Dependent X-Ray Absorption in Indirect Conversion Avalanche Detector.....	144
7.1.2 Carrier Trapping in a-Se Based Direct Conversion Avalanche Detector	145
7.1.3 Novel Structure for a-Se Based Direct Conversion Avalanche Detector	146
7.1.4 Performance Comparison of Different Detectors	148
7.2 Contributions	148
7.3 Future Work.....	150
References.....	152

LIST OF FIGURES

Figure 1.1 (a) Standard digital mammography and (b) 2D synthetic mammography images show a speculated mass in breast [20]..... 5

Figure 1.2 X-ray imaging process with a flat panel x-ray image detector [24] 7

Figure 1.3 Direct and indirect conversion x-ray detectors with readout TFT array. 8

Figure 1.4 Simplified schematic of active matrix array with few pixels [24]. The electric charge stored in each row of pixel capacitors are read periodically..... 9

Figure 1.5 pixel cross section of a direct conversion detector including storage capacitor, TFT and charge amplifier. 11

Figure 1.6 Physical cross section of an individual pixel of a direct conversion x-ray detector (not to scale). 12

Figure 1.7 Physical cross section of a single pixel of an indirect conversion x-ray detector (not to scale). 14

Figure 1.8 Photomicrographs of a direct conversion detector with a pixel electrode made of indium tin oxide (ITO) [42]. 18

Figure 1.9 Schematic of a) 3T and b) 4T active pixel sensors. The select transistor transfer the signal to the data line. 20

Figure 1.10 Generation of electrons and holes due to impact ionization process..... 26

Figure 2.1 Theoretical and emitted x-ray photon fluence as a function of energy. The electron from the filament has a maximum energy of 100-keV. The emitted photon fluence is less than the theoretical value at low energy due to self-absorption. The low energy photons are absorbed by the target itself. The peaks are due to characteristic x-ray emission [66]. The photon energy distribution can be further modified by using external filters..... 35

Figure 2.2 The mass attenuation coefficient of a) a-Se and b) CsI including the contribution of Rayleigh scattering, Compton scattering and photoelectric effect. The data have been extracted from Ref. [67]. 37

Figure 2.3 EHP creation energy, W_{\pm} of a-Se as a function of electric field at different x-ray energies. The symbols are the experimental results that extracted from Ref. [70] [71] [72] [73].39

Figure 2.4 Energy band diagram of a scintillator (or phosphor) showing excitation and scintillation..... 40

Figure 2.5 Schematic of an x-ray detector with pixel electrodes. The top electrode is the radiation receiving electrode and it is positively biased and the pixel electrodes are negatively biased. Therefore photo-generated hole travels from x_1 and x_2 (in the direction of the electric field) and induces charge on the electrodes.....	44
Figure 2.6 Illustration of charge carrier injection from metal electrode to semiconductor. E_C and E_{Fm} are the conduction band energy of the semiconductor and Fermi level in metal electrode..	47
Figure 2.7 Modulation transfer function of an x-ray detector at different spatial frequencies. The detector resolves the input image ~100% of the input image when its spatial frequency is 1 lp/mm. At a spatial frequency of 2 lp/mm, the detector resolves less than 100% and at 4 lp/mm, the input information is totally lost at the output.	49
Figure 2.8 a) The top view of a bare TFT (without photoconductor/scintillator) showing pixel aperture width and pixel pitch, b) MTF due to aperture function [84].	51
Figure 3.1 Cross sectional diagram showing an indirect FPI with CsI scintillator and a-Se HARP layer.....	61
Figure 3.2 Schematic diagram for calculating the LSF due to K-fluorescence reabsorption.	63
Figure 3.3 Flow diagram showing the propagation of signal and NPS through the stages (shaded stages are not considered when the imaging properties of CsI is calculated) of cascaded linear system model for indirect avalanche x-ray detector.	65
Figure 3.4 The DQE of CsI layer as a function of spatial frequency for different thicknesses of CsI samples, (a) $L_1=150 \mu\text{m}$, (b) $L_1=300 \mu\text{m}$, and (c) $L_1=600 \mu\text{m}$. The symbols, solid lines and dashed lines represent experimental results [104], T_{OP} with and without Lubberts effect, respectively.	73
Figure 3.5 Presampling MTF of the CsI layers for different thicknesses.	74
Figure 3.6 Presampling MTF (solid line), MTF without optical blurring with Lubberts effect (dash-dotted line) and MTF without K-fluorescence reabsorption scattering (dashed).	75
Figure 3.7 DQE(f) at different electric fields. The solid and dashed lines overlap at $F=103 \text{ V}/\mu\text{m}$	77
Figure 3.8 Calculated DQE(f) at different avalanche gains. The solid ($g_m=45$) and dashed ($g_m=25$) lines overlap.	78
Figure 3.9 DQE(0) as a function of applied electric field for different fluoroscopic exposures. The detector thickness is $15 \mu\text{m}$	79

Figure 4.1 Cross sectional diagram showing an a-Se based direct-conversion multiplayer avalanche x-ray detector. The detailed diagram can be found in Ref. [124].	84
Figure 4.2 Diagram showing the flow of signal and NPS in the cascaded linear system model proposed for direct-conversion multiplayer avalanche x-ray detector. Here ζ is the probability of K -shell interaction, ω is the probability of K -fluorescence production and f_k is the average reabsorption probability of K -fluorescent x-ray photons within the photoconductor volume.	87
Figure 4.3 Weighting potential of a direct-conversion multilayer avalanche x-ray detector. The charge induction is the greatest in the region near the pixel electrode.	97
Figure 4.4 Average weighting potential in the absorption layer for different mesh aperture.	98
Figure 4.5 Comparison between Wronski et al.'s [124] model and the proposed model for different avalanche gains. The x-ray exposure is 1 μ R.	100
Figure 4.6 Effect of hole lifetime on $DQE(f)$ when $N_e = 1500$ e/pixel. The dotted line represents the $DQE(f)$ without carrier trapping.	101
Figure 4.7 Effect of non-zero weighting potential in the absorption layer on the $DQE(f)$ at $X = 1$ μ R and the value of g_M is set to 1.	102
Figure 4.8 $DQE(f)$ at different electric fields hence different avalanche gains.	103
Figure 4.9 Calculated $DQE(f)$ at different avalanche gains. The solid ($g_m = 35$) and dashed ($g_m = 20$) lines overlap.	104
Figure 4.10 $DQE(0)$ as a function of applied electric field for different fluoroscopic exposures.	105
Figure 5.1 Cross sectional diagram showing an a-Se based direct-conversion multilayer avalanche x-ray detector with trapping layer and the time dependent electric field profile. The dashed line shows the initial electric field (F_0) and the solid line shows the electric field profile as the time elapses. Drawing is not to scale.	111
Figure 5.2 Diagram showing the flow of signal and noise power spectrum in the cascaded linear system model. Here ζ is the probability of K -shell interaction, ω is the probability of K -fluorescence production and f_k is the average reabsorption probability of K -fluorescent x-ray photons within the photoconductor volume.	118
Figure 5.3 Electric field distribution at different times. The electric field is uniform across the detector at $t = 0$ s.	122
Figure 5.4 Average electric field in the gain region after applying bias voltage for different thicknesses of trapping layer.	123

Figure 5.5 Average electric fields in the gain region as functions of time after applying bias voltage of 4.7 kV for different values of N_t^f . The trapping layer thickness is 5 μm	124
Figure 5.6 Effect of applied bias voltage on the dark current density as a function of time.	125
Figure 5.7 Comparison between $\text{DQE}(f)$ of an a-Se based direct conversion detector used in tomosynthesis and that of the proposed structure calculated using the cascaded linear system model. The solid symbols are the measured $\text{DQE}(f)$ at different x-ray exposures. The solid and dashed lines are $\text{DQE}(f)$ calculated using the developed model at 1.02 and 0.41 mR, respectively. These lines overlap when avalanche multiplication is considered in the proposed structure. The measured values are obtained from Ref. [132].	127
Figure 5.8 $\text{DQE}(0)$ vs applied voltage for different trap densities in trapping layer. The x-ray exposure is 0.41 mR.	128
Figure 5.9 The effect of avalanche gain on presampling MTF. The solid and dotted lines represent the presampling MTF with and without avalanche gain, respectively.	129
Figure 6.1 $\text{DQE}(f)$ of different detectors with avalanche gain for fluoroscopic applications.	136
Figure 6.2 $\text{DQE}(0)$ of different detectors for fluoroscopic applications as a function of x-ray exposure with and without avalanche gain.	137
Figure 6.3 MTF of different structures for fluoroscopic application.	138
Figure 6.4 $\text{DQE}(f)$ of different detectors with avalanche gain for tomosynthesis.	139
Figure 6.5 $\text{DQE}(0)$ of different detectors for tomosynthesis as a function of x-ray exposure with and without avalanche gain.	140
Figure 6.6 MTF of different structures for tomosynthesis.	141

LIST OF TABLES

Table 1.1 Different parameters for FPI used in radiography, mammography and fluoroscopy [38]	16
Table 2.1 Physical properties of potential photoconductors [38].....	39
Table 2.2 Physical properties of different phosphors [38].....	41
Table 4.1 Parameters used in the simulations	99
Table 5.1 Parameters used in the simulations	121
Table 6.1 Different parameters used for comparing the imaging performance of different avalanche detectors.	133
Table 6.2 Parameters used in the simulations	134

LIST OF ABBREVIATIONS

2D	-	Two-dimensional
3D	-	Three-dimensional
AMA	-	Active matrix array
AMFPI	-	Active matrix flat panel imager
APD	-	Avalanche photodiodes
APS	-	Active pixel sensor
CMOS	-	Complementary metal oxide semiconductor
CR	-	Computed radiography
CT	-	Computed tomography
DOS	-	Density of states
DQE	-	Detective quantum efficiency
DR	-	Direct radiography
DRL	-	Distributed resistance layer
DXA	-	Dual-energy x-ray absorptiometry
EHP	-	Electron-hole pair
ESF	-	Edge spread function
FDA	-	Food and Drug Administration
FDM	-	Finite Difference Method
FFDM	-	Full-field digital mammography
FPD	-	Flat-panel detector

FPI	-	Flat panel imager
Fps	-	Frames per second
HARP	-	High-gain avalanche rushing amorphous photoconductor
HL	-	High light
HR	-	High resolution
IGZO	-	Indium gallium zinc oxide
<i>i</i> -layer	-	Intrinsic layer
IP	-	Imaging plate
ITO	-	Indium tin oxide
LD	-	Lucky drift
LSF	-	Line spread function
MRI	-	Magnetic resonance imaging
MTF	-	Modulation transfer function
NNPS	-	Normalized noise power spectrum
NPS	-	Noise power spectrum
PPS	-	Passive pixel sensor
PVD	-	Physical vapor deposition
RIL	-	Resistive interface layer
RT	-	Reset transistor
S/N	-	Signal to noise
SF	-	Source follower
SNR	-	Signal to noise ratio
TFT	-	Thin film transistor

TT	-	Transfer transistor
US	-	Ultrasound
XRII	-	X-ray image intensifier

LIST OF SYMBOLS

γ	-	Quantum yield (fraction of the dissociated EHPs to all the total EHPs created)
$\sigma_{g_i}^2$	-	Variance of i^{th} stage in cascaded linear-system model
a	-	Pixel aperture width
A^*	-	Richardson constant
A_{mesh}	-	mesh aperture
A_{pixel}	-	Pixel area
c	-	Speed of light
d	-	Pixel pitch
E	-	Photon energy
E_C	-	Energy of conduction band
E_F	-	Fermi level energy
E_g	-	Bandgap
E_k	-	Average energy of K -fluorescent x-ray
E_{phonon}	-	Phonon energy
E_V	-	Energy of valance band
F	-	Electric field
f_k	-	Reabsorption probability of K -fluorescent x-ray
f_N	-	Nyquist frequency
F_w	-	Weighting field of the charge collecting electrode
g_i	-	Gain of i^{th} stage in cascaded linear-system model

h	-	Plank's constant
h_{CsI}	-	Reciprocal of mean absorption length of CsI
I_i	-	Induced current
I_l	-	Modified Bessel function
J_0	-	Zero-order Bessel function
J_d	-	Dark current density
$J_{inj,e}$	-	Electron injection current
k_B	-	Boltzmann constant
L	-	Thickness of medium
m^*	-	Effective mass
M_{atom}	-	Atomic mass of material
MTF_a	-	MTF due to pixel aperture
N	-	Density of states
N_0	-	Ionization line density
N_c	-	Effective density of states in conduction band
N_d	-	Noise due to dark current
N_{sp}	-	Number of spatial divisions in the absorption layer
N_v	-	Effective density of states in valance band
P	-	Probability density
Q	-	Collected charge
q	-	Unit charge
Q_i	-	Induced charge
r_0	-	Initial separation between bound EHP

R_{max}	-	Range of the primary photoelectron
S_{Ne}	-	Electronic noise power
T	-	Temperature
T_i	-	MTF of i^{th} stage in cascaded linear-system model
T_{int}	-	Charge integration period
T_K	-	MTF due to K -fluorescent x-ray
v	-	Velocity
ν_p	-	Photon frequency
ν_r	-	Thermal velocity
V_w	-	Weighting potential
W_{\pm}	-	Ionization energy
X	-	X-ray exposure
x	-	Distance in medium
Z	-	Atomic number
α	-	Attenuation coefficient
α'	-	Linear trapping attenuation coefficients of carriers travelling towards top electrode
α_{en}	-	Absorption coefficient
β'	-	Linear trapping attenuation coefficients of carriers travelling towards mesh electrode
β_{op}	-	The optical coupling efficiency between CsI and a-Se
β_{pf}	-	Poole-Frenkel coefficient
ϵ_s	-	Permittivity of the medium

η	-	Quantum efficiency
κ	-	Reciprocal of relaxation length of photon
λ	-	Wavelength
μ	-	Carrier mobility
ξ	-	Probability of <i>K</i> -shell interaction
ρ	-	Density of material
ρ_i	-	Reflectivity of CsI layer
τ	-	Carrier lifetime
τ_r	-	Release time of the trapped charge carriers
ϕ	-	Photon fluence
ω	-	Probability of <i>K</i> -fluorescence production
φ	-	Effective barrier height
\hbar	-	Modified plank constant

CHAPTER 1

Introduction

Since the discovery of x-ray by Professor Wilhelm Roentgen in 1895, medical imaging has grown from a state of infancy to a high level of maturity. Till date it remains as one of the most common and useful means for medical diagnosis and therapy. The core concept of medical x-ray imaging is to capture the spatially modulated x-ray radiation that contains information relating to specific aspect of body structure or function. The captured image quality must be sufficient enough so that the interpreted information is meaningful. The x-ray image quality depends on various aspects of the imaging system, namely, x-ray anode and filtration, tube current, radiation dose, x-ray scattering and x-ray detectors [1][2]. This thesis focuses on various aspects of the x-ray detectors.

Depending on the diagnostic method used, the x-ray radiation can either be detected with analog (x-ray film) systems or with digital systems. These acquisition methods have distinct properties. The analog x-ray detectors consist of three main components, namely, a) x-ray film, b) intensifying screen and c) light-proof housing or cassette [3]. The intensifying screen converts the modulated x-ray intensity to visible light photons and the light photons imprint a latent image on a photographic emulsion (silver halide) of x-ray films. The cassette protects the film from ambient light and with the help of pressure pads, keeps the film and intensifying screen in close and uniform contact [4]. A photochemical processing reveals the image on an x-ray film [3].

On the other hand, there are two major types of digital radiography (i.e., computed radiography, CR and direct radiography, DR). In CR systems, modulated x-ray energy is absorbed and stored in a phosphor imaging plate (IP). Later, the IP is read with a scanning laser beam [5]. Whereas in direct radiography, the modulated x-ray energy is converted (e.g., direct conversion or indirect conversion) into electric charges and stored into capacitors which are instantly read with the help of thin film transistor (TFT) or complementary metal oxide semiconductor (CMOS) sensor array [6].

A vigorous development in digital radiography has made possible up to 80% reduction of x-ray dose, when compared with analog systems [7]. The obvious advantages of digital radiography are fast processing of x-ray images, elimination of darkroom and usage of processing chemicals, higher patient throughput, and reduction of errors associated with improper image developing in analog systems. The digital detectors ensure wider dynamic range (range within which the detector shows linear response) that leads to reduction of failed x-ray exposure [8].

Among CR and DR digital systems, DR is inherently digital and has the ability to read out x-ray panel very fast (30 frames per second) [9]. Therefore, DR has the potential to be used as a real-time x-ray imager. It has already been used in applications as tomosynthesis where fast image rate is a requirement [10][11]. The limitation of DR systems is that its performance is not adequate for low dose applications.

In real time imaging (i.e., fluoroscopy), a continuous x-ray beam is passed through human body to capture the motion of specific body parts that are being examined. The quality of fluoroscopic images depends on radiation dose. A higher x-ray dose ensures better image quality. However, x-ray radiation is injurious to human health. It causes radiation-induced cancers, cataracts, and other consequences [12]. It is therefore important to minimize the usage of x-ray radiation while maintaining adequate image quality. The image quality of an x-ray detector is described by its detective quantum efficiency (DQE). The DQE describe the ability of the x-ray detector to transfer signal to noise ratio (SNR) from its input to its output [13][14]. The common goal is to ensure higher DQE at all relevant frequencies for all radiological imaging methods. A detail description of DQE is given in chapter 2.

1.1 Radiological imaging methods

Radiological imaging is a branch of medicine that uses imaging technologies to diagnose and treat numerous medical conditions. It includes many diagnostic tasks, imaging techniques and several modalities, namely, radiography, fluoroscopy, computed tomography (CT), ultrasound (US), nuclear medicine, and magnetic resonance imaging (MRI). Among these modalities, radiography, CT and fluoroscopy use ionizing radiation to construct images of body parts. Radiography (including mammography) and fluoroscopy are the most popular medical imaging modalities due to their low cost of operation, high resolution and rapid processing suitable for the emergency situations [15].

Since the first radiographic image captured by Wilhelm Roentgen on a photographic plate, plain radiography has always been the first-line test of choice in radiologic diagnosis. Many diseases or conditions (e.g., various types of arthritis and pneumonia, benign bone tumors, fractures, blockage of bowel, collapsed lung and congenital skeletal anomalies) are identified in human body by classic diagnosis obtained by non-invasive plain radiographs [16]. Plain radiography is the oldest x-ray imaging modality. Due to its accessibility and low cost, plain radiography is still the first choice in radiologic diagnosis [17].

In radiography, the energy of the x-ray photons varies depending on the radiographic application. Such as mammography and dual-energy x-ray absorptiometry (DXA) are the low energy radiography modalities. In mammography, low x-ray energy is used because the breast contains only soft tissues [18]. On the other hand, in chest radiography, higher x-ray energy is used because the x-ray beam has to penetrate highly dense bones. Mammogram detects characteristic masses or microcalcifications in the breast to identify breast cancer in early stage. Another branch of mammography is breast tomosynthesis, also known as semi three-dimensional (3D) mammography. Tomosynthesis is a promising and relatively new advancement in mammography. In breast tomosynthesis, a sequence of images is captured while the x-ray tube is positioned at different angles with respect to the breast [11]. Finally, three-dimensional (3D) images of the breasts are synthesized with the help of computer reconstructions. These 3D images can detect the overlapped fibroglandular tissues in the breast and thus ensure better detection of cancer. In recent times, U.S. Food and Drug Administration (FDA) has suggested to use both conventional full-field digital mammography (FFDM) and tomosynthesis together. The combined procedure (i.e., FFDM and tomosynthesis) is recommended because microcalcification clusters are better detected

in FFDM and accurate comparison with prior studies can be done using FFDM. However, a new technique has been proposed to reduce the total x-ray dose by approximately 40%–50% and the required time to perform the combined procedure [19]. This procedure is known as 2D synthetic mammography (SM). In SM, 2D images are reconstructed from the images captured for tomosynthesis. Figure 1.1 shows that the image quality of 2D SM is comparable to that of FFDM.

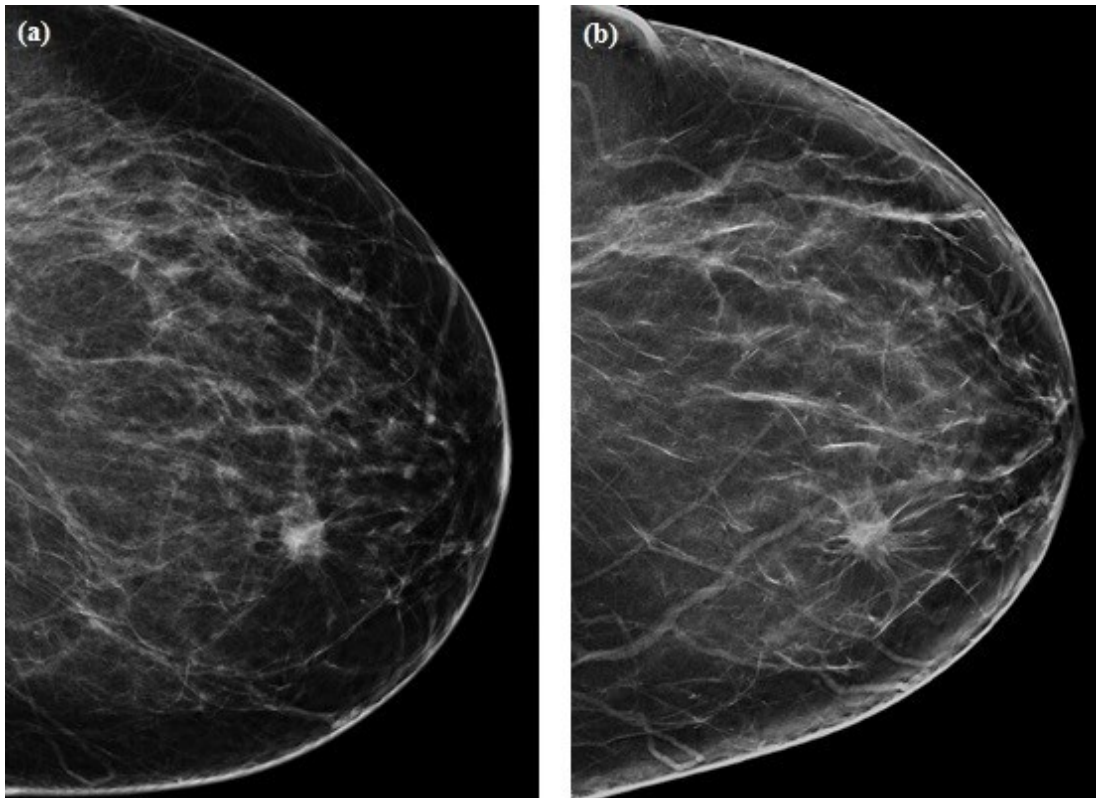


Figure 1.1 (a) Standard digital mammography and (b) 2D synthetic mammography images show a speculated mass in breast [20].

Fluoroscopy shows the real-time moving images of body parts. Therefore, a continuous x-ray beam passes through human body until the fluoroscopy procedure is finished. Fluoroscopy allows to monitor surgical procedures and examine the passage of a contrast agent (“dye”) through the body. Fluoroscopy is also used to guide small instruments such as catheters through blood vessels. The

most promising feature of fluoroscopy is that it is less invasive than surgical procedures and thus reduces the risk of infection and the recovery time [21].

One of the main components of these medical imaging systems is the image sensor or the detector. The flat panel x-ray detectors based on a large area self-scanned active matrix array (AMA), also known as active matrix flat panel imagers (AMFPI), has already replaced the film based analog systems for radiographic applications (including mammography) in many facilities [22]. In recent years, AMFPI is introduced to fluoroscopic applications. However, AMFPI is not yet fully commercialized for fluoroscopy due to its inadequate performance at fluoroscopic exposure level [23]. The following sections include the description of the detectors that are widely used for radiography and fluoroscopy.

1.2 Active matrix flat panel imagers

Flat panel imagers are used in many applications, such as, medical, security and industrial imaging. The concept of AMFPI is illustrated in Figure 1.2. The object (e.g., body part) which is being imaged is placed in between the x-ray source and the AMFPI. The x-ray beam passes through the object and impinges onto the large array of pixels that are integrated part of the active matrix array (AMA). An AMA is a 2D array of pixels. It contains millions of identical pixels. Each pixel receives various amounts of x-ray intensity and converts them into electric charges proportionally.

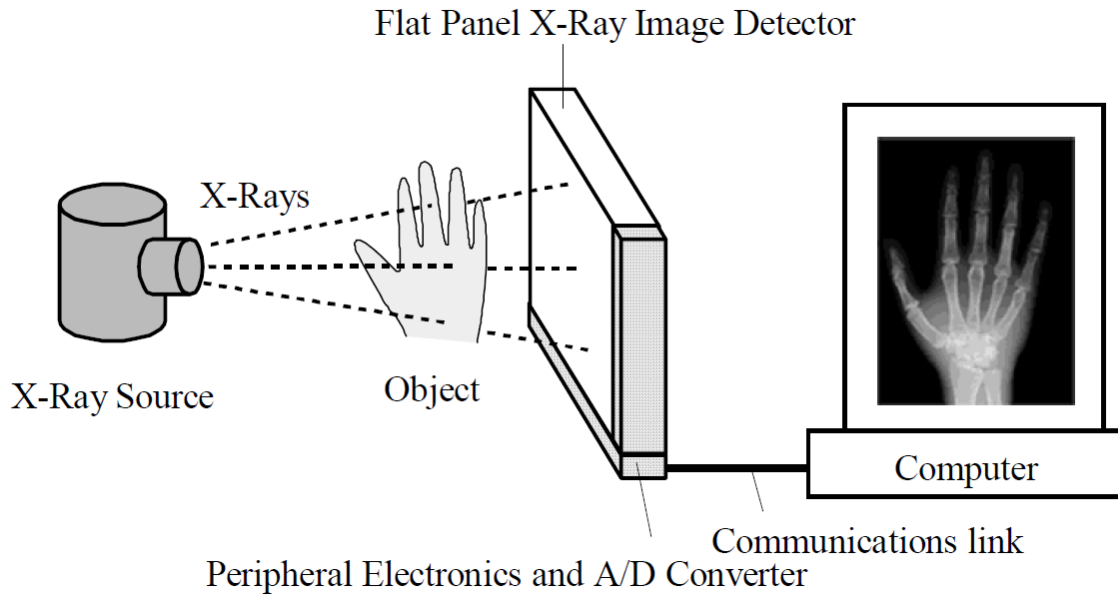


Figure 1.2 X-ray imaging process with a flat panel x-ray image detector [24]

There are essentially two types of AMFPs based on the technique used to convert x-ray energy into electric charges, namely, direct and indirect conversion. The majority of commercial AMFPs are indirect conversion detectors [25]. In an indirect conversion detector, the x-ray photons impinged upon a scintillator and the scintillator converts the x-rays into light photons. Then the light photons interact with the photodiode and generate electric charges [26]. On the other hand, in a direct conversion detector, the x-ray photons interact with the photoconductor and directly create electric charges [24]. Figure 1.3 explains the concept of direct and indirect conversion x-ray detectors. The charge distribution across the panel is readout by scanning the pixels line by line. The readout charges are treated as signals. The signals are then transmitted to a computer system for storage and display.

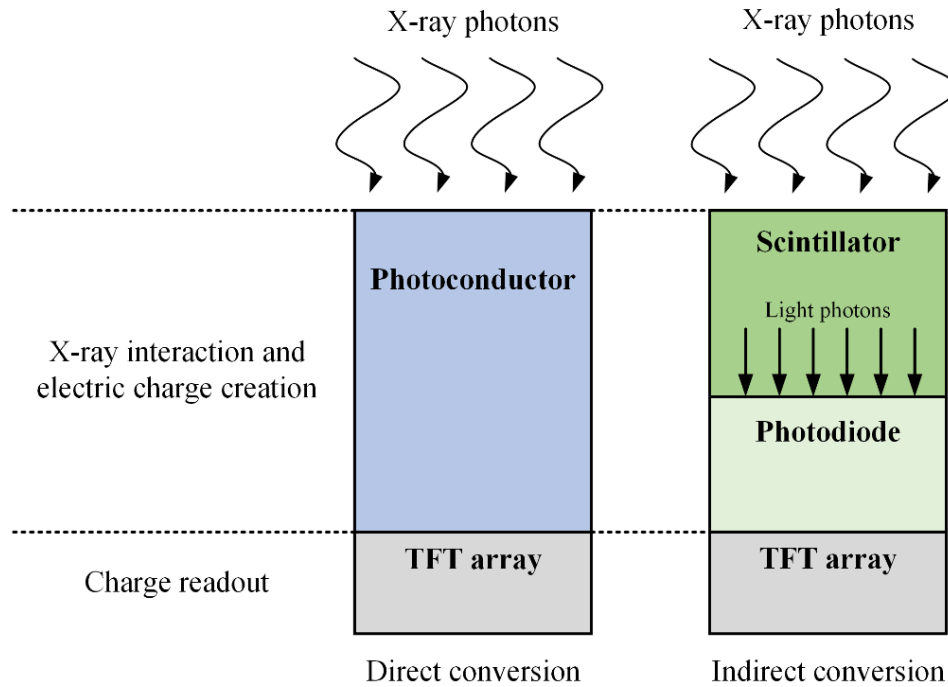


Figure 1.3 Direct and indirect conversion x-ray detectors with readout TFT array.

Each pixel consists of a storage capacitor for holding the charges collected by the pixel electrode. The capacitance of the capacitor is significantly greater than that of the photoconductor. Therefore, most of the applied high voltage is dropped across the photoconductor. The TFT functions as a switch. It is used to control the charge flow from the capacitor. The drain terminal of the TFT is usually connected to the storage capacitor and the source terminal is connected to the collective data transmission line. The data-line is connected to charge amplifier. An external circuit controls the operation of the TFTs. It remains in the “OFF” state while the pixel integrates charges and a voltage pulse at the gate terminal turns the TFT “ON” when the pixel is ready to be read. The panel is read row by row, that means all the TFTs in one row is turned “ON” at the same time and the stored charges in the capacitors of that specific row are transferred to the external charge amplifiers.

Figure 1.4 shows a simplified schematic of an active matrix array. The gate terminals of the TFTs in each row are connected with a common gate line and on the other hand, the source terminals of the TFTs in each column are connected with a common data line. For example, when the gate line i is turned ON, all the pixels situated on line i discharge their capacitors through the data lines from $j=1$ to N (assuming N is the total number of data line). Once all the data lines are read, the next gate line (e.g., $i + 1$) is turn ON. Each data line is connected with a charge integrating amplifier, which amplifies the charges by a pre-set gain value. The parallel signals are then converted into serial data with the help of a multiplexer. The analog data can be digitalized before or after multiplexing. The data are converted into digital image in a computer.

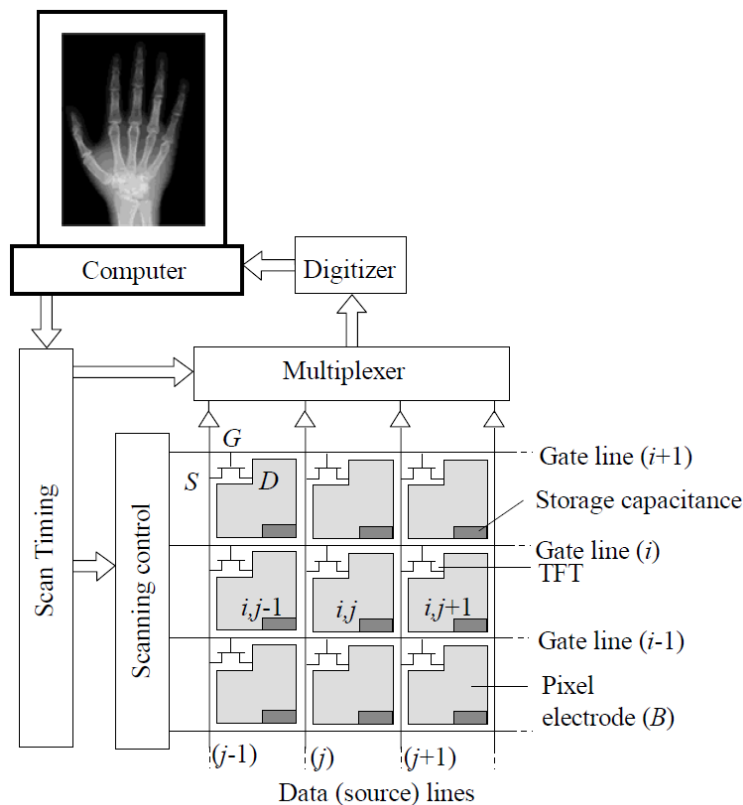


Figure 1.4 Simplified schematic of active matrix array with few pixels [24]. The electric charge stored in each row of pixel capacitors are read periodically.

1.2.1 Direct conversion detector

The three main components of a pixel in AMFPI are photoconductor, storage capacitor and, TFT. Figure 1.5 shows the pixel cross section of a direct conversion detector including the components of AMA. A uniform layer of x-ray photoconductor with high atomic number (e.g., stabilized amorphous selenium, a-Se), is deposited onto the AMA that is based on a-Si:H. Due to the excellent transport properties of both holes and electrons, low dark current density and high spatial resolution, stabilized a-Se has become the most popular photoconductor for direct conversion AMFPIs [27]. Furthermore, the high absorption coefficient of a-Se over the x-ray energy range of interest ensures high quantum efficiency. The absorbed x-ray energy ionizes the atoms in the photoconductor and generates electron-hole pairs (EHPs). An applied high voltage at the radiation receiving electrode (top electrode) drives the x-ray generated charges towards bottom surface of the photoconductor, where they are collected by the pixel electrode. The applied voltage can be positive or negative.

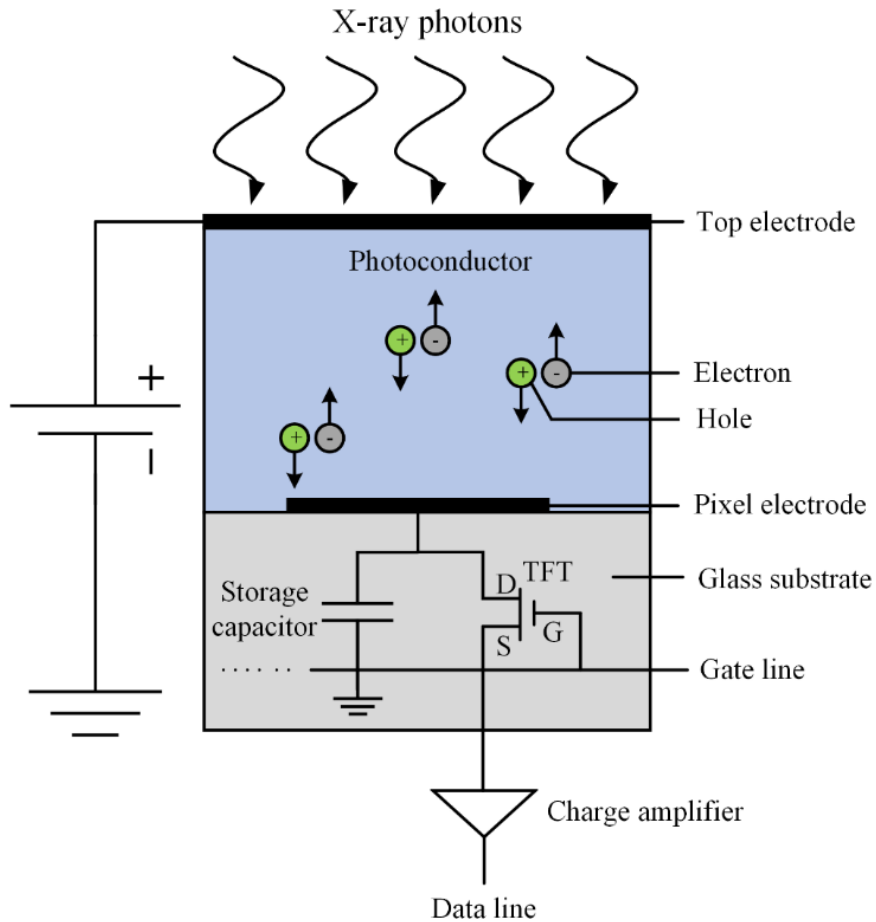


Figure 1.5 pixel cross section of a direct conversion detector including storage capacitor, TFT and charge amplifier.

The selection of the polarity of the applied voltage depends on the choice of charge carrier (i.e., electrons or holes) to be collected. When the top electrode is positively biased, the direction of the electric field is directed towards the pixel electrodes. Therefore, the x-ray generated electrons and holes travel toward the top and pixel electrodes, respectively. Usually, the charge carrier with higher mobility is preferable to be collected at the pixel electrode.

Figure 1.6 shows the cross section of a single pixel where the top electrode is the x-ray receiving electrode. The top electrode is usually deposited using any convenient physical vapor deposition (PVD) technique [28]. The bottom or pixel electrode on the glass substrate is a plate of the storage capacitor and also the drain terminal of the TFT.

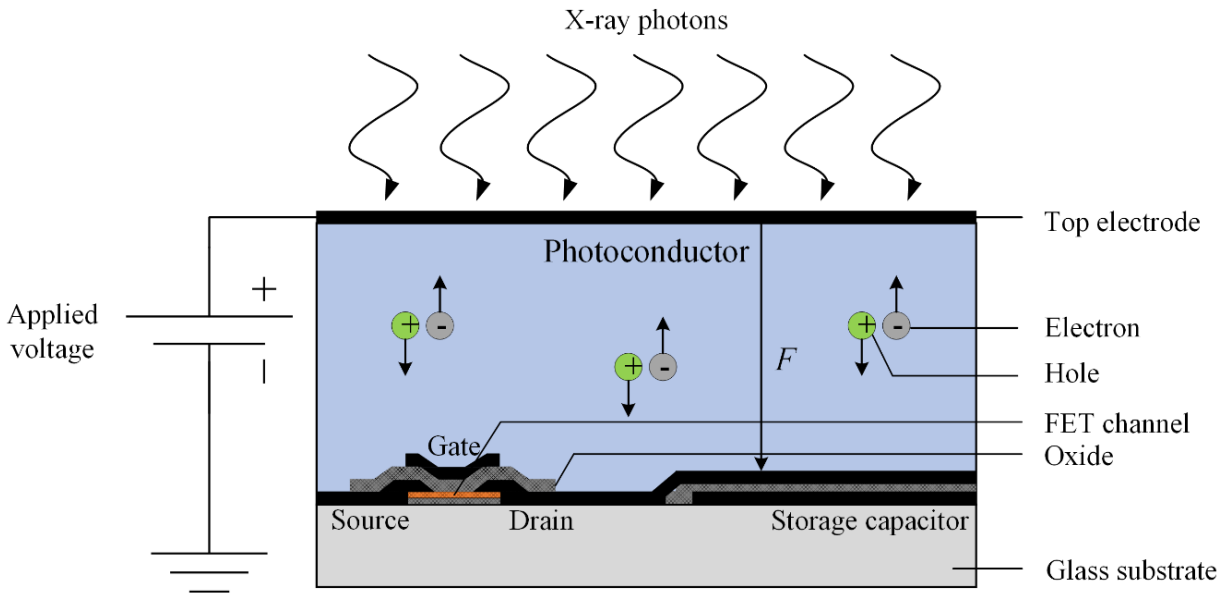


Figure 1.6 Physical cross section of an individual pixel of a direct conversion x-ray detector (not to scale).

1.2.2 Indirect conversion detector

The majority of AMFPIs available in the market, are based on indirect conversion because the price of indirect conversion detectors are cheaper compared to that of direct conversion detectors [25]. In indirect conversion detectors, the x-ray photons are absorbed in phosphor screens (e.g., gadolinium oxysulfide, Gd_2O_2S) or structured cesium iodide (CsI) scintillator and generate optical

photons. The performance of an indirect x-ray detector depends critically on the selection and design of the scintillator. The scintillators should minimize the spread of light photons. The spread of light photons reduces the spatial resolution of the detector. The atomic number of a scintillator also plays a vital role. High atomic number facilitates x-ray absorption. The columnar structure (fiber-optic like) CsI scintillators doped with Thallium (Tl) guides the light towards the detector and thus reduces the scattering of the light photons [29]. Moreover, the high atomic number of cesium and iodide is suitable for x-ray absorption. These properties made CsI the most widely used scintillators in indirect x-ray imaging systems [30].

A photodiode coupled with the scintillator converts the optical photons into electric charges (i.e., EHPs). It is usually a PIN photodiode based on hydrogenated amorphous silicon (a-Si:H). In a PIN junction the intrinsic layer (*i*-layer) is sandwiched between thin *n*- and *p*-layers. The thickness of the *i*-layer is $\sim 1.5 \mu\text{m}$ and the *n*- and *p*-layers are in nanometer scale [31]. Indium tin oxide (ITO) is used as the optical photon receiving electrode due to the fact that it is transparent to the optical photons. The photogenerated charges in the photodiode are electronically processed, similarly as in direct conversion detectors. Figure 1.7 shows the cross section of a pixel in an indirect conversion x-ray detector.

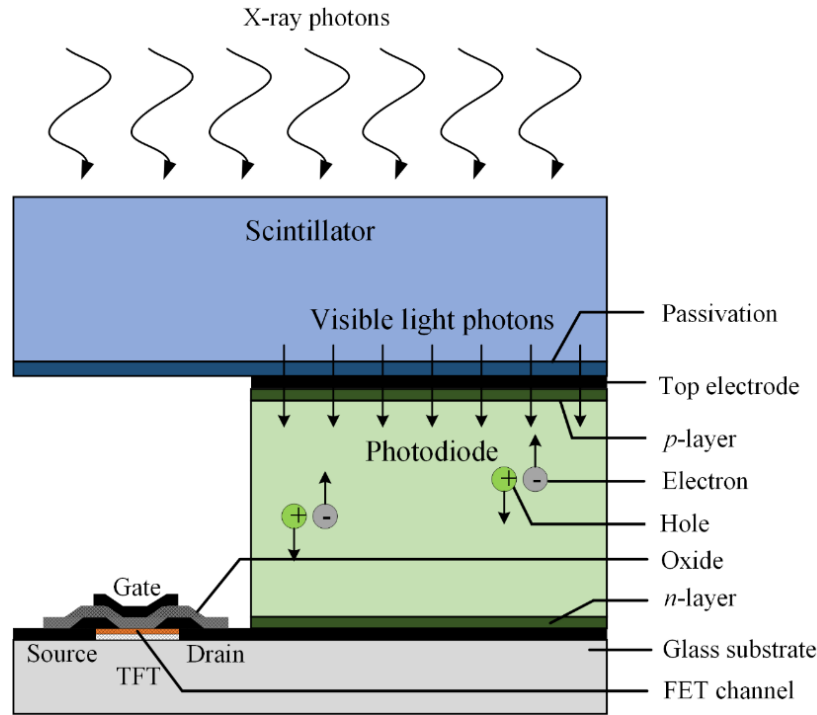


Figure 1.7 Physical cross section of a single pixel of an indirect conversion x-ray detector (not to scale).

1.3 AMFPI for fluoroscopy

A traditional fluoroscope consists of an x-ray tube and a fluorescent screen, such as, zinc cadmium sulfide. This old method of fluoroscopy requires the radiologists to increase the sensitivity of their eyes to subdued lights. The procedure that the radiologists follow to increase the sensitivity of their eyes is known as dark adaptation [32]. However, poor coupling between radiologist's eyes and fluorescent screen results loss of optical photons (known as secondary quantum sink). Besides, this technique does not permit to store the fluoroscopic video. In middle of 20th century, introduction of x-ray image intensifier (XRII) has removed the complexities arising from dark

adaptation and the secondary quantum sink [33][34]. An XRII converts the x-ray photons into optical photons at higher intensity compared to a simple fluoroscope. XRII systems pose some basic limitations such as, pincushion distortion due to curved input phosphor surface [35], blooming artefact due to limited dynamic range of the coupled video camera [36] and S-distortion due to external magnetic field [37]. Furthermore, the XRII system are heavy and bulky which make it difficult to move around patients' body. These limitations compelled the researchers to search for alternatives of the existing XRIIs system.

Over the past two decades, active research has resulted a rapid development in AMFPI. In many medical facilities, traditional analog radiography systems have already been replaced by digital AMFPIs. This vigorous advancement and availability of AMFPI, have made it a potential candidate for fluoroscopy. Unlike XRII systems, AMFPIs are compact and larger in size, free from image distortion, and are not affected by external magnetic fields. Besides, the AMFPIs have less conversion steps compared to the XRIIs, which ensures AMFPIs having higher DQE and also higher resolution when the pixel size is sufficiently small. However, a major drawback of AMFPIs is its inherent electronic noise. The electronic noise arises from the readout circuitry. It causes the performance of the AMFPIs to degrade at low x-ray exposure required for fluoroscopic applications. The different requirements of x-ray imaging systems for various x-ray imaging modalities are mentioned in the following section.

1.4 Requirements of radiographic and fluoroscopic imaging systems

Ever since the beginning, radiologists have been developing and improving the techniques to acquire and interpret the x-ray images. Since the very first x-ray image captured, the x-ray detectors have greatly evolved and are still evolving. However, the main purpose of x-ray imaging systems remains more or less the same. Radiographic images are inspected to identify the abnormal tissues and fluoroscopy is used in interventional radiography to perform minimally invasive procedures. These techniques impose some requirements on different x-ray imaging modalities. The requirements include field of view, dynamic range, pixel size, and accepted noise level etc. Table 1.1 shows some of the requirements that should be taken into consideration while designing flat panel imagers (FPI) for different medical imaging modalities, such as, radiography, mammography and fluoroscopy.

Table 1.1 Different parameters for FPI used in radiography, mammography and fluoroscopy [38]

Clinical task	Chest radiology	Mammography	Fluoroscopy
Detector size	35 cm × 43 cm	18 cm × 24 cm	25 cm × 25 cm
Pixel size	200 μm × 200 μm	50 μm × 50 μm	250 μm × 250 μm
Number of pixels	1750 × 2150	3600 × 4800	1000 × 1000
Readout time	~1 sec	~1 sec	~1/30 sec
X-ray spectrum	120 kVp	30 kVp	70 kVp
Mean exposure	300 μR	12 mR	1 μR
Exposure range	30 - 3000 μR	0.6 - 240 mR	0.1 - 10 μR

1.5 Electronic noise

The peripheral electronics of the AMA are responsible for providing appropriate voltages to the pixel TFTs, amplifying and digitalizing the pixel output. It also synchronizes the workflow, such as, storing the charges and reading out the pixels in a timely manner and finally transmitting the images to a workstation where they are processed for visualization. However, the peripheral electronics and the AMA act as sources of noise that reduce the imaging performance and dynamic range of the AMFPIs.

The thermal noise (also known as Johnson noise) is a source of noise that contributes to the total electronic noise. The thermal energy facilitates the Brownian motion of the charge carriers and thus randomly changes the conductance of electronic components. The thermal noise is known to be a white noise as its response remains constant to a wide range of frequencies. It is very sensitive to the operating temperature. Among all other components, the storage capacitor is most vulnerable to the thermal noise. The thermal noise in capacitors is known as kTC noise [39]. The effect of this noise can be minimized by reducing the temperature and/or the capacitance. However, reducing the operating temperature affects the performance of the TFTs and efficiency of the AMFPI. On the other hand, reducing the storage capacitance is not feasible because it reduces the dynamic range and also the breakdown voltage.

A charge-integrating amplifier is fed with the output signal of a selected pixel. A standard configuration of charge-integrating amplifier consists of a feedback capacitor and a reset switch. The switch is turned “ON” to flush the feedback capacitor. The gain of the amplifier is determined

by the capacitance of the feedback capacitor. However, the amplifier also contributes to the total electronic noise. The noise performance of the amplifier mainly depends on its intrinsic noise and the noise due to input load capacitance (e.g., data line capacitance) [40][41]. The data line capacitance depends on its length and the number of connected pixels. A data line of a typical AMFPI has a capacitance of 50 to 100 pF which contributes a noise of 500 to 2000 e.

The gate voltage controls the charge flow across the TFTs. As shown in Figure 1.8, the gate lines pass over or under the data lines and thus a coupling capacitance exists between these two lines.

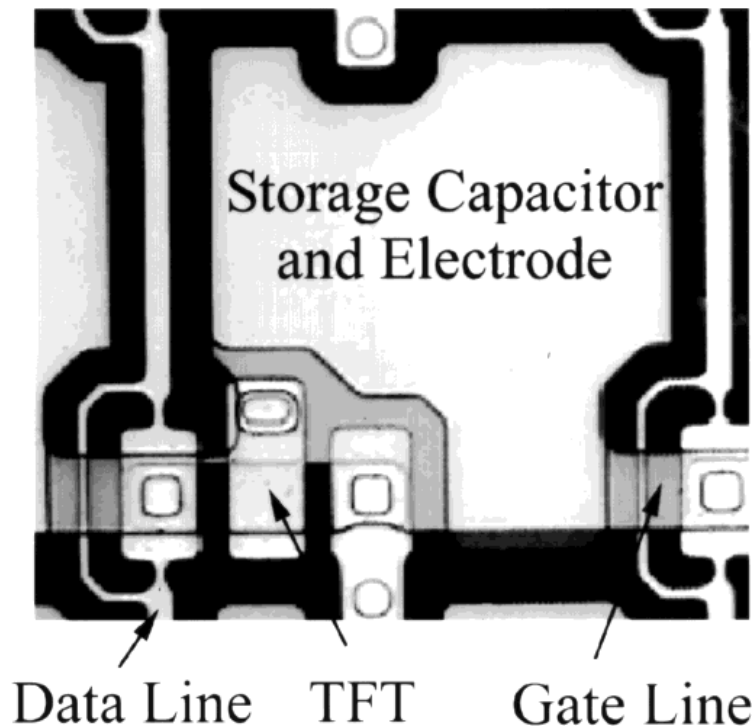


Figure 1.8 Photomicrographs of a direct conversion detector with a pixel electrode made of indium tin oxide (ITO) [42].

Therefore, some charges are injected into the data lines due to modulation of the voltage on the gate lines in order to turn the TFTs “ON” or “OFF”. The injection occurs at every gate and data line intersections. The voltage source used to bias the photoconductor or photodiode also interferes with the noise performance of the device. Without proper shielding or efficient design layout, the noise of the power supply can capacitively couple into the AMA.

1.6 Possible solutions to overcome electronic noise

The effects of electronic noise become severe at low exposures. It is because, at very low exposures, the performance of an AMFPI does not remain quantum noise limited. The detector performance is referred to be quantum noise limited if the total output noise is dominated by the stochastic variation of the impinged x-ray photon distribution. The performance of AMFPI should be close to quantum noise limited for fluoroscopic applications. However, at lower exposure, the number of charge carrier created by x-ray photons is comparable to the electronic noise. Therefore, either the electronic noise has to be minimized or the signal strength has been increased. The electronic noise can be reduced by using active pixel sensors (APS) to readout the panel. On the other hand, signal strength can be increased by using high gain photoconductors. The signal strength can also be increased by initiating impact ionization of charge carriers in the photoconductor.

1.6.1 Active pixel sensor based x-ray detector

In recent years, the low-noise CMOS APS has become a strong competitor of a-Si:H TFT based passive pixel sensor (PPS) in x-ray imaging applications. It is because the active pixel-based readout circuit contains a low noise analog amplifier in each pixel and therefore reduces the floor noise [43]. Active pixels are compatible with both direct and indirect conversion x-ray detectors. This section provides the basic introduction to CMOS APS in x-ray detectors.

The most popular architectures of CMOS APS are 3T and 4T. The letter “T” stands for transistor. The 3T and 4T APS contain 3 and 4 transistors per pixel, respectively. Figure 1.9 shows the schematics of 3T and 4T APS.

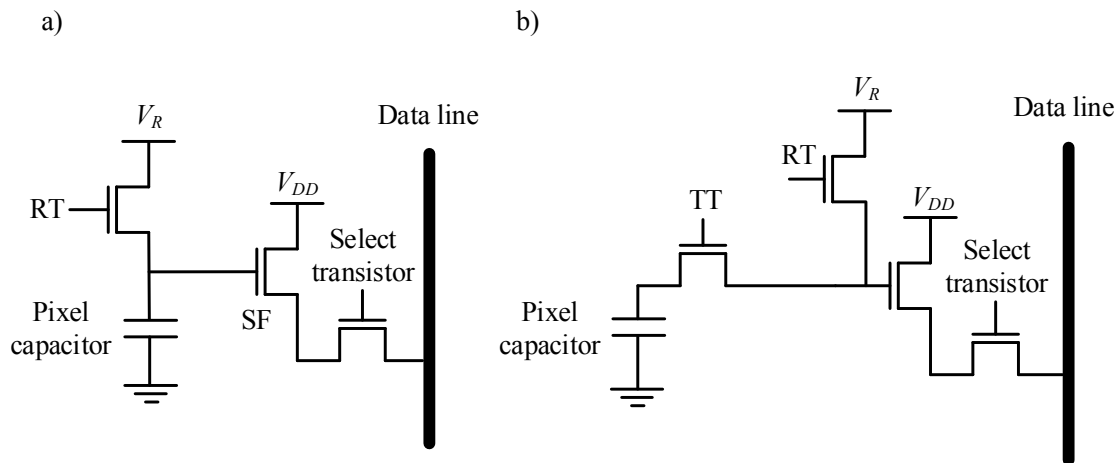


Figure 1.9 Schematic of a) 3T and b) 4T active pixel sensors. The select transistor transfer the signal to the data line.

As shown in Figure 1.9 (a), the 3T APS consists of reset, source follower and row select transistors. The operation of a CMOS APS based x-ray detector is divided into three stages, namely, a) reset,

b) integration and, c) readout. During the reset stage, the storage element is reset to predefined voltage by turning “ON” the reset transistor (RT). The reset transistor is turned “OFF” and the charges that are created by the x-ray photons are stored during the integration period. The stored charges reduce the preset voltage across the storage element. This voltage depends on the total integrated charge per pixel. Finally, the panel is readout row by row by switching “ON” the row select transistors. The current flowing through the source follower (SF) and data line depends on the gate voltage of the source follower. In 4T APS [Figure 1.9 (b)], one transistor is added to the existing 3T structure. The extra transistor is called to be transfer transistor (TT). It introduces a floating diffusion node which is connected to the reset and source follower transistors. The stored charges are transferred to the floating diffusion node and then readout similarly as in 3T CMOS APS. The transfer transistor isolates the charge storage element from the reset and row select transistors. As a result, the reset and read processes are separated from the charge integration process. This enables the double sampling feature which is used to correct the offset. It is to be noted that the readout process is non-destructive (i.e., charges are not removed while reading the pixel) in CMOS APS based x-ray detectors.

The pixel amplifiers are only activated when a particular row is scanned. This allows energy optimization, hence heat reduction. The parallel readout increases the frames per second (fps) rate. Also, the panel readout time can be modulated by changing the bias current. A frame rate of 20 – 30 fps has been reported [44][45]. The source follower transistor separates the sensing node from the data line capacitance and thus improves the signal to noise (S/N) performance. Since CMOS APS readouts are non-destructive, multiple readouts of pixels is possible. Therefore, signal averaging technique can be used to reduce the electronic noise.

Although CMOS APS reduces the electronic noise to e/pixel , the fill factor reduces since the APS contains more transistors [46][47]. Furthermore, the active pixels are vulnerable to radiation damage because one or more transistors operates as amplifiers. Multiple transistors at each pixel also increase the complexity of device fabrication. As a result, the cost of x-ray imagers based on APS significantly increases.

1.6.2 High gain photoconductors

The photoconductor plays an important role on the performance of the direct conversion AMFPI. There are some basic requirements that the materials or compounds must fulfil in order to be considered as photoconductors. A photoconductor should have high quantum efficiency so that it can absorb most of the incident x-ray photons. High quantum efficiency reduces the required x-ray exposure. The intrinsic sensitivity of the photoconductors determines the number of collectable EHPs created by per unit of x-ray radiation. Therefore, the photoconductors with high sensitivity ensure good image quality at low x-ray dose. The lifetime (τ) and mobility (μ) of the charge carriers determine the charge collection efficiency. A photoconductor should have high lifetime-mobility product ($\tau\mu$) to reduce carrier trapping and increase the charge carrier collection. Another important aspect of a photoconductor is its large area deposition capability. A photoconductor should exhibit uniform characteristic throughout the active region. At last but not least, the dark current density (current flowing across photoconductor due to applied voltage) should be as small as possible. It

is because the dark current is a source of noise and also reduces the dynamic range of the detector [48].

The energy required to create an EHP in widely used photoconductor (i.e., a-Se) is very high (i.e., ~ 45 eV at the electric field of $10 \text{ V}/\mu\text{m}$) [27]. As a result, at low x-ray exposures, AMFPI based a-Se becomes vulnerable to electronic noise. On the other hand, high gain photoconductors, such as, Mercuric Iodide (HgI_2), Lead Iodide (PbI_2), Cadmium Zinc Telluride (CdZnTe) and Lead Oxide (PbO) require less energy to create EHP and thus provide the necessary gain for quantum noise dependent performance [6][48][27].

The aforementioned high gain photoconductors are polycrystalline materials. The grain boundaries in these polycrystalline materials has great influence on the photoconductor uniformity. The x-ray image quality largely depends on the uniformity of the photoconductors [49]. Non-uniform photoconductors cause pixels to have different sensitivity in response to the same input x-ray beam. Non-uniform behavior is observed when the grains are larger than the pixels. Therefore, it is in the best interest to reduce the grain size to increase the uniformity. However, when the grain size is reduced, the collection efficiency is adversely affected. It is because, reducing the grain size forces the charge carriers to travel through the grain boundaries and hence the defect states. It causes the charge carriers to be trapped and/or recombined. This in turn reduces the schubweg (i.e., distance travelled by charge carriers between two consecutive deep trapping events) of charge carriers, which in turn reduces the collection efficiency of the photoconductor.

High dark current is also one of the main drawbacks of these high gain photoconductors. The high dark current reduces the dynamic range of the detector by filling up the storage capacitors and leaves small room for x-ray signals. Therefore, it becomes difficult to operate at higher and/or longer x-ray exposures when the dark current is high. Besides, the dark current is a source of noise (square root of the dark current). The maximum allowed dark current in AMFPI is 1 - 10 pA/mm² [50]. In the literature, the dark current in HgI₂ is reported as high as ~180 pA/mm² when the temperature is 35° C and the electric field is ~0.95 V/μm [51]. It increases superlinearly with the applied voltage [52]. Unlike HgI₂, the dark current in PbI₂ increases sublinearly with the applied bias voltage. It is in the range of 10 - 50 pA/mm² when the electric field is 0.5 V/μm and increases to a higher value of 100 – 450 pA/mm² when the field is increased to 1 V/μm [51][53]. PdO exhibits extremely high dark current which increases with applied field. It is found that the dark current is ~250 pA/mm² at 3.5 V/μm [54][55]. Although CdZnTe (CZT) has a better sensitivity, the dark current is very high compared to that in a-Se. The dark current is ~70 pA/mm² (at applied field of 0.25 V/μm) and increases linearly with the applied voltage [56]. Higher Zn concentration reduces the dark current. However, the hole mobility and carrier lifetime deteriorate when the concentration of Zn is increased. It is due to the fact that Zn introduces extra defects in the CZT layer.

Another shortcoming of these high gain photoconductors is high lag signal (residual signal from previous exposure). The lag signal makes it difficult to use these photoconductors in fluoroscopic applications where it is required to maintain a frame rate of ~30 fps. It is observed that PbI₂ requires a long time to remove the residual signal. In fluoroscopic mode, the lag signals in PbI₂ are reported to be ~75% and 15% after 66 ms and 3 s from the first readout, respectively [51]. The

size of the grains in CZT is large and non-uniform which has profound effect on the lag signal. Tokuda et al. [56] has shown in their recent work that Cl doping reduces lag signal from 40% to 15% of a 300 μm thick CZT photoconductor. However, the lag signal remains very high in comparison with the existing technologies. It is also found that the PbO layer become unstable when it comes in contact with surrounding ambient air. The oxygen voids act as traps for x-ray generated charge. Therefore, the detectors based on PbO become prone to lag and ghost (change in x-ray sensitivity). The lag signal is 9% and 4% after 1s when the electric fields are 0.5 and 3.5 $\text{V}/\mu\text{m}$, respectively, which makes it inapplicable for fluoroscopic applications [48].

Although these photoconductors have fulfilled many of the requirements, performance and quality parameters such as, stability, uniformity, dark current, and signal lag require more investigative studies before using them as photoconductors.

1.6.3 Avalanche gain

The avalanche multiplication of charge carriers is caused by impact ionization. The impact ionization is a process occurring in a semiconductor when a charge carrier gains enough energy in form of kinetic energy to liberate one or more bound electrons while it travels. The charge carriers obtain the required kinetic energy to initiate impact ionization from the applied electric field. Figure 1.10 shows the process of generating multiple charge carriers by impact ionization.

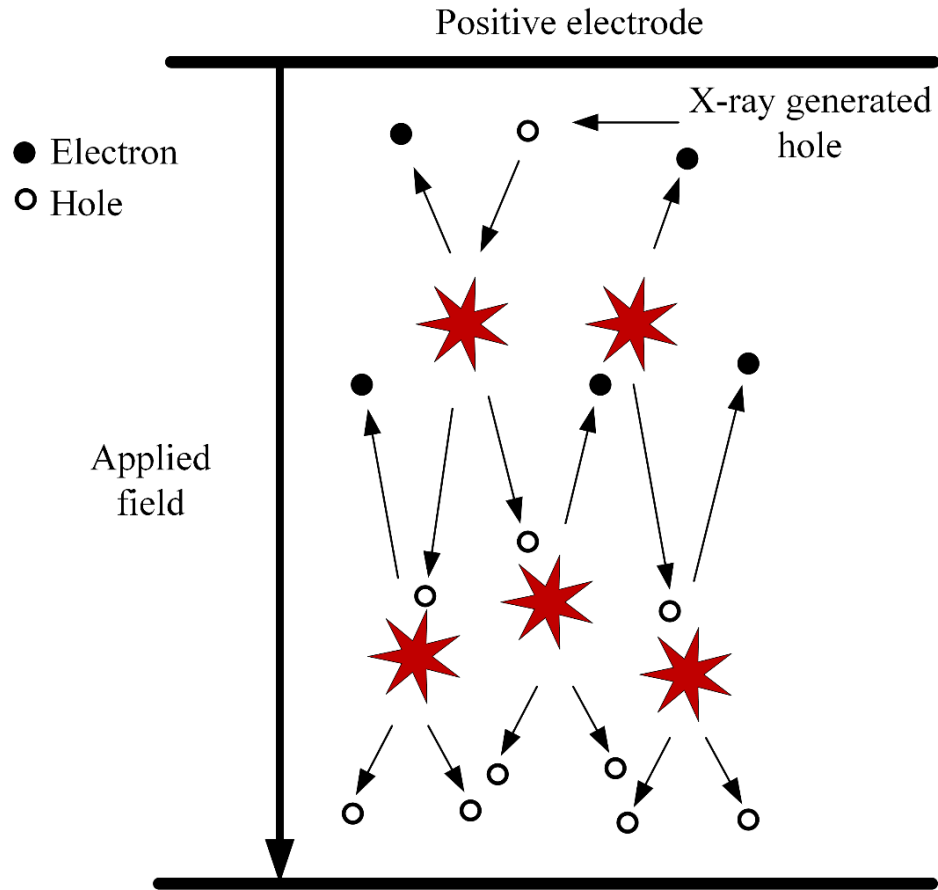


Figure 1.10 Generation of electrons and holes due to impact ionization process.

As mentioned earlier, a-Se is a well-established material for x-ray detection and exhibits controllable impact ionization. It has been observed that the holes in a-Se achieve sufficient energy to initiate avalanche multiplication when the electric field is above $70 \text{ V}/\mu\text{m}$ [48]. Recently, Reznik et al. have reported an avalanche gain of 1000 in a-Se [57]. Using the avalanche multiplication of holes in a-Se, high-gain avalanche rushing amorphous photoconductor (HARP) optical image sensors for a practical ultrahigh sensitive television camera has been developed [58]. There is an active research ongoing for utilization of HARP film on top of AMA for low dose medical x-ray imaging. The avalanche multiplication of holes boosts up the signal strength

and improves the detector performance in terms of signal to noise ratio (SNR) by overcoming the effect of electronic noise at low x-ray doses.

The dark current in HARP-AMFPI can become very high due to the extremely high applied electric field and the impact ionization of thermally activated and/or injected charge carriers. The blocking layers adjacent to the electrodes can reduce the charge injection. The prospective a-Se based HARP-AMFPI are 1) Cerium dioxide (CeO_2) with a bandgap of 3.3 eV as hole blocking layer, resistive interface layer (RIL) as electron blocking layer [58], and 2) indium gallium zinc oxide (IGZO) as hole blocking layer [59]. In both cases, the top and pixel electrodes are indium tin oxide (ITO) and gold (Au), respectively. Another disadvantage of HARP-AMFPI is that at electric field higher than 100 and 110 $\text{V}/\mu\text{m}$ in 30 and 10 μm thick photoconductors, respectively, the electrons start participating in impact ionization process. The electron impact ionization results in self-sustaining avalanche breakdown. A tremendous amount of charge carrier generated during breakdown, screen out the applied voltage across the photoconductor. Therefore, the electric field should be always less than the breakdown field to limit the avalanche gain. Another drawback of hole avalanche is the gain fluctuation noise due to exponential x-ray absorption over thick photoconductor layer. A solution to this problem is to separate the avalanche gain region from the x-ray absorption layer.

1.7 Research objective

One of the purposes of the research work is to understand the underlying physics behind the observed imaging performance of both direct and indirect conversion detectors at low x-ray doses. Also, to investigate the feasibility of avalanche gain as a solution to the problems arising from high electronic noise. In order to do so, physics-based models have been developed to explain and understand the behaviors of these detectors. The models incorporate avalanche multiplication to enhance the performance on the detectors at low doses. The research objective also includes designing and modeling the electrical and imaging performance of a novel detector structure for low dose x-ray imaging.

1.7.1 Imaging performance of amorphous selenium based indirect conversion avalanche X-ray detector

Enhancement of system gain of indirect conversion x-ray detectors is required to achieve quantum noise dependent performance and higher DQE at low x-ray exposures. One of the strategies to increase the gain is to replace the conventional photodiode with avalanche photodiodes (APD). In recent times, crystalline silicon based small area APDs have been developed, however large area deposition still remains a great challenge [60]. High dark due to thermal generation in low bandgap of silicon increases the noise in APD based detectors [61]. Moreover, the gain of APDs exhibit significant dependency on temperature. Therefore, the operating voltage has to be varied depending on the temperature in order to control the overall gain [62]. On the other hand,

amorphous selenium can be deposited over a large area and also avalanche gain can be achieved at reasonable electric fields ($\sim 70 \text{ V}/\mu\text{m}$) [48]. The dark current caused by applied voltage can be reduced by using blocking layers [48]. Therefore, in order to increase the system gain, a-Se with avalanche gain can be used in place of conventional photodiode in indirect conversion x-ray detectors. However, the optical efficiency of a-Se is not as high as that of silicon-based photodiode. This loss is compensated by the avalanche gain offered by the photoconductor [63]. However, a thorough imaging performance of such indirect detectors are yet to be determined.

In such detectors, the x-ray image resolution in terms of MTF and NPS are strong function of the absorption depth of the incident x-ray photons. It is because the spreading of light photons depends on the distance that they travelled. Therefore, the exponential x-ray absorption makes the indirect conversion x-ray image sensors vulnerable to the Lubberts effect (non-uniform response to x-ray photons), which in turn makes the sensor more sensitive to the electronic noise. Due to Lubberts effect, the MTF at higher frequencies deteriorate significantly.

In the literature, the linear-system models developed for the indirect conversion detectors do not consider the Lubberts effect. The blurring caused by the optical photon spreading is usually considered in the models by using empirical equations. Therefore, the effects of different parameters on Lubberts effect cannot be realized with the existing models for indirect conversion x-ray detectors. Moreover, these models fail to fit the experimental results at higher spatial frequencies.

A cascaded linear-system model is proposed by incorporating image blurring due to Lubberts effect and K -fluorescence reabsorption in indirect conversion avalanche x-ray detectors. The detector is based on CsI scintillator and a-Se photodiode. The model ensures good fit to the experimental results at higher frequencies. It computes the required electric field to overcome the effect of electronic noise and depth dependent x-ray absorption (Lubberts effect) in amorphous selenium indirect conversion avalanche detectors.

1.7.2 Charge trapping in direct conversion avalanche detector

Due to defect states within the bandgap of a-Se (absorption layer) in direct conversion detectors, x-ray generated charge carriers may get trapped. As a result, the sensitivity (collected charge per unit area per unit exposure of radiation) reduces. At the same time, the trapped carriers induce charges on the neighboring pixel and thus decrease the resolution of the detector.

In order to increase the DQE at low x-ray exposures, a-Se based direct conversion avalanche detector with grid electrode has been proposed in the literature. However, the existing cascaded linear-system model for the detector structure, does not consider carrier trapping in the absorption layer. Thus, the predicted DQE is overestimated.

A cascaded linear system model is developed to determine the detective quantum efficiency (DQE) considering trapping of charge carriers in the absorption layer of an amorphous selenium multilayer direct conversion avalanche detector. This model considers the effects of charge carrier

trapping and reabsorption of *K*-fluorescent x-rays on the frequency-dependent $DQE(f)$. A 2D simulation is performed to calculate the actual weighting potential in the absorption layer in presence of grid electrode, which is used to calculate the amount of collected charge.

1.7.3 Novel Amorphous Selenium Avalanche Detector

The indirect conversion detectors are vulnerable to the Lubberts effect. Whereas, a-Se based direct conversion detector is by far superior in terms of MTF. Although the direct conversion detector with grid electrode, offers the required avalanche gain to overcome the adverse effect of electronic noise, it has a complicated structure which makes it difficult to fabricate and also it is required to apply two voltages in order to initiate avalanche multiplication.

A novel amorphous selenium (a-Se) avalanche detector structure for low dose direct-conversion flat-panel x-ray detector is proposed. The proposed structure contains blocking layers to reduce carrier injection from metal electrodes and hole trapping layer to separate x-ray absorption layer from avalanche gain region. The trapping layer enhances the electric field in the gain region to initiate avalanche multiplication of charge carriers which improves the signal strength. As a result, the proposed structure is simpler and requires only one voltage source. This chapter also investigates the feasibility of the structure for avalanche gain with negligible avalanche noise by using the Semiconductor Module of COMSOL Multiphysics together with a cascaded linear system.

A brief outline of the thesis work is presented in the following section.

1.8 Thesis outline

This thesis consists of seven chapters, starting with this introductory chapter. In the second chapter, review of the background theories, useful terminologies and physics-based explanation of observed phenomena in the detectors are presented. Chapter 3 describes a linear-system model which includes Lubberts effect in indirect conversion avalanche detector. Another model which includes charge carrier trapping in the absorption layer of the direct conversion avalanche detector with grid electrode is presented in the fourth chapter. In chapter 5, a novel amorphous selenium (a-Se) avalanche detector structure for low dose direct-conversion flat-panel x-ray detector is proposed. The comparison between different detector structures is given in chapter 6. Finally, the conclusion drawn from the theoretical calculation using the developed models is presented in chapter 7.

CHAPTER 2

Background Theory

The radiological imaging techniques rely on the differential absorption of x-ray in different body parts. The x-ray absorption depends on the radiological density of the materials that are being imaged and also the energy of the x-ray beam. Another essential part of x-ray imaging is to capture the modulated x-ray beam and convert it into meaningful information. This chapter will focus on the theories and definitions of important terms related to x-ray production and absorption, charge carrier generation and collection and the basic characteristics of x-ray imaging detectors.

2.1 X-ray spectra from x-ray tube

The basic two components of x-ray tubes are a cathode and an anode which are separated by a certain distance and are enclosed in a vacuum chamber. The anode, also known as target, is positively biased and the cathode, which is the source of bombarding electron, is negatively biased. The cathode contains tungsten filaments which emits electrons when it is heated. The filament is heated up by flowing current through it. The electrons emitted from the filament gain kinetic energy from the electric field existing between anode and cathode due to the applied voltage [64]. The emitted electrons lose their energy in form of x-ray radiation as they travel through the anode.

The range of the wavelength of x-ray radiation used in medical imaging varies from 0.01 to 0.1 nm. The energy (E) of x-ray photon is proportional to its frequency (ν_p) and given by [65]

$$E = h\nu_p \quad (2.1)$$

where, h is the Plank's constant and ν_p can be expressed by c/λ . Here, λ is the wavelength and c is the speed of light. Thus, the energy of x-ray used in diagnostic imaging spans from 12.4 to 124 keV.

The electrons with high kinetic energy strike on the anode material (usually tungsten) and interact with the coulombic field existing in the anode atoms. During the interactions, the electrons decelerate and produce bremsstrahlung radiation. The intensity of bremsstrahlung radiation depends on the charge and mass of the electrons and the charge of the nuclei of the target material. On the other hand, characteristic radiation emits when the incident electron interacts with the electrons of the target material. The interaction takes place when the incident electron possesses more energy than the binding energy of the electron in the target material.

For example, if an electron emitted from the cathode liberates a bound electron from the K -shell of the anode, a vacancy is created in that particular energy shell. An electron from the outer shell emits a specific amount of energy in form of characteristic x-ray and fills the vacancy in the K -shell. The name of the characteristic x-ray depends on the electron receiving shell. In this example, the K -shell is receiving an electron from the outer shell, therefore the characteristic x-ray produced due to this transition is called K -fluorescent. The energy of the K -fluorescence x-ray depends on the shell from where the electron has made the transition. If an electron from L -shell fills the vacancy in K -shell, it emits a characteristic x-ray with energy of $(70 - 11)$ or 59 keV. The same

process takes place to fill up the newly created vacancy in *L*-shell. Therefore, liberation of an electron triggers a cascade of electron transitions. This process of filling vacancies continues until the outermost shells are filled with free electrons. The liberated electrons can subsequently interact with other atoms in the same manner and liberate more electrons and create more characteristic x-rays. This process comes to an end when the electron loses all its kinetic energy. Figure 2.1 shows the x-ray spectra when the kinetic energy of the impinged electron is 100 keV.

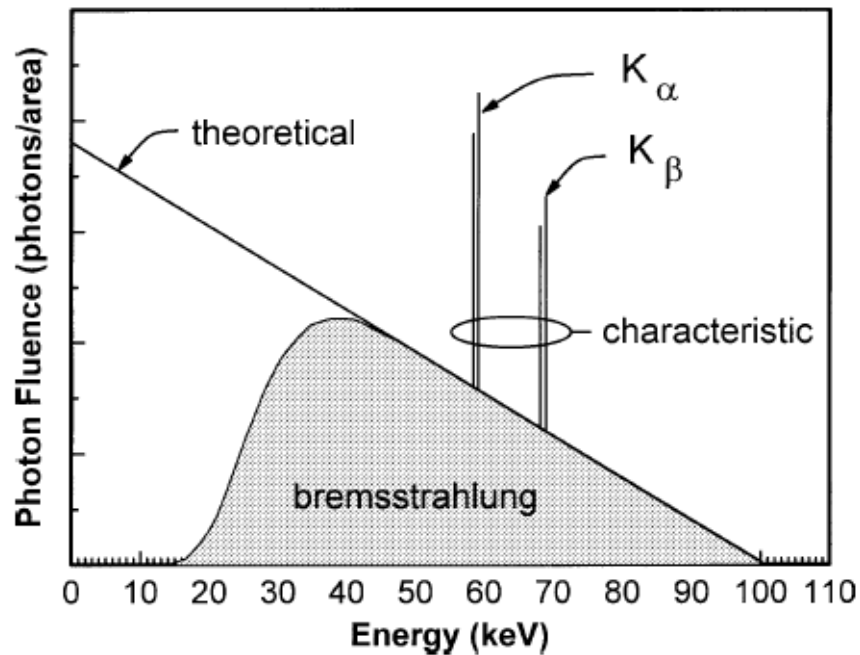


Figure 2.1 Theoretical and emitted x-ray photon fluence as a function of energy. The electron from the filament has a maximum energy of 100-keV. The emitted photon fluence is less than the theoretical value at low energy due to self-absorption. The low energy photons are absorbed by the target itself. The peaks are due to characteristic x-ray emission [66]. The photon energy distribution can be further modified by using external filters.

2.2 X-ray interaction in a-Se and CsI

As mentioned earlier, a-Se and CsI are the most established photoconductor and scintillator, respectively. Therefore, in this research work, a-Se is chosen as the photoconductor for the direct conversion detectors and CsI is chosen as the scintillator for the indirect conversion detectors. This section describes the contribution of different x-ray interaction processes (mentioned in the previous sections) to the total x-ray energy attenuation in a-Se and CsI.

The primary interaction of impinged x-rays is mainly divided into two categories, such as, x-ray photon scattering and ionizing atoms in the medium. The x-ray scattering includes, Rayleigh and Compton scattering and creation of characteristic x-rays. On the other hand, both photoelectric effect and Compton scattering ionize atoms by transferring energy to the electrons. The liberated electrons dissipate energy to the medium and may create more EHPs. The electrons may also lose energy in form of bremsstrahlung radiation.

As a result, a fraction of the total energy of an x-ray photon is absorbed (not scattered) in the medium. The fraction can be described by the energy absorption coefficient α_{en} . For example, when the energy of the incident x-ray is E , the absorbed energy (E_{ab}) in the medium is $(\alpha_{en}/\alpha)E$. Figure 2.2 (a) and (b) show the mass attenuation coefficients of a-Se and CsI. The mass attenuation coefficient of a material is defined by dividing its attenuation coefficient by its density. Thus, the unit of mass attenuation becomes cm^2/g . The figures also show the contribution of photoelectric effect, Rayleigh and Compton scattering to the attenuation. The abrupt jumps in the absorption coefficient are attributed to the x-ray interaction with K -shell electrons.

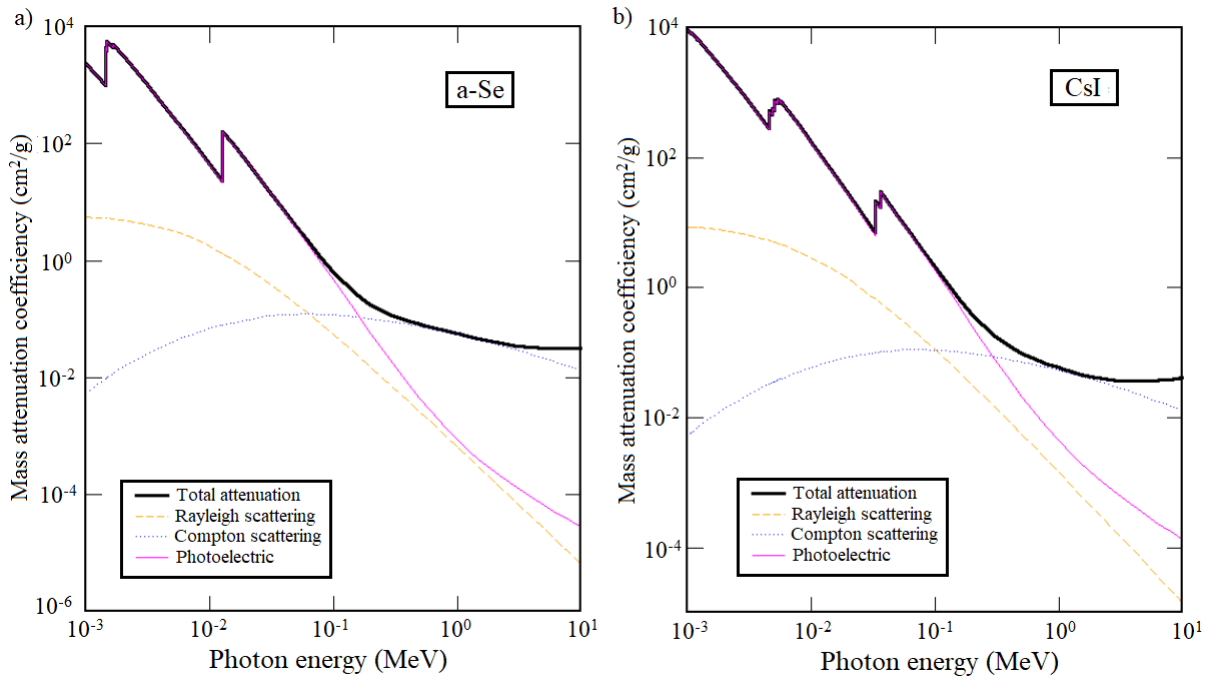


Figure 2.2 The mass attenuation coefficient of a) a-Se and b) CsI including the contribution of Rayleigh scattering, Compton scattering and photoelectric effect. The data have been extracted from Ref. [67].

2.3 Electron and hole pair creation energy (W_{\pm})

2.3.1 W_{\pm} in photoconductors

A photon with energy equal or more than the bandgap (E_g) can excite an electron from the valance band to the conduction band. The excited electron created by highly energetic x-ray photon can ionize more atoms while travelling towards the electrode. In addition, the required energy (W_{\pm}) to

create an EHP is not simply the bandgap energy of the photoconductor. According to Klein's rule, W_{\pm} is a function of the bandgap of photoconductors and can be given by [68],

$$W_{\pm} \approx 2.8E_g + E_{phonon} \quad (2.2)$$

where, E_{phonon} is the dissipated phonon energy. The value of E_{phonon} in Equation 2.2 is less than 0.5 eV.

The value of W_{\pm} is well defined in crystalline semiconductor and also independent from the applied electric field. However, in some photoconductors (e.g., a-Se), the value of W_{\pm} depends on the field and the also x-ray photon energy [48]. Unlike most of semiconductors which follow Klein's rule, a-Se has exceptionally high value of W_{\pm} . It is assumed that the high value of W_{\pm} of a-Se is due to the recombination of initial EHPs. Recently, Hijazi *et al.* [69] have developed a model to evaluate the charge extraction yield depended W_{\pm} .

Kabir *et al.* have developed an empirical expression to compute the x-ray photon energy and electric field dependent W_{\pm} of a-Se. At room temperature, the empirical expression is

$$W_{\pm} = \left(6 + 300/F^{0.9}\right) \left(0.38 + 4.8/E^{0.5}\right) \text{eV} \quad (2.3)$$

where, the electric field, F is in V/ μm and the x-ray photon energy, E is in keV. The experimental fit of the empirical expression is shown in figure 2.3.

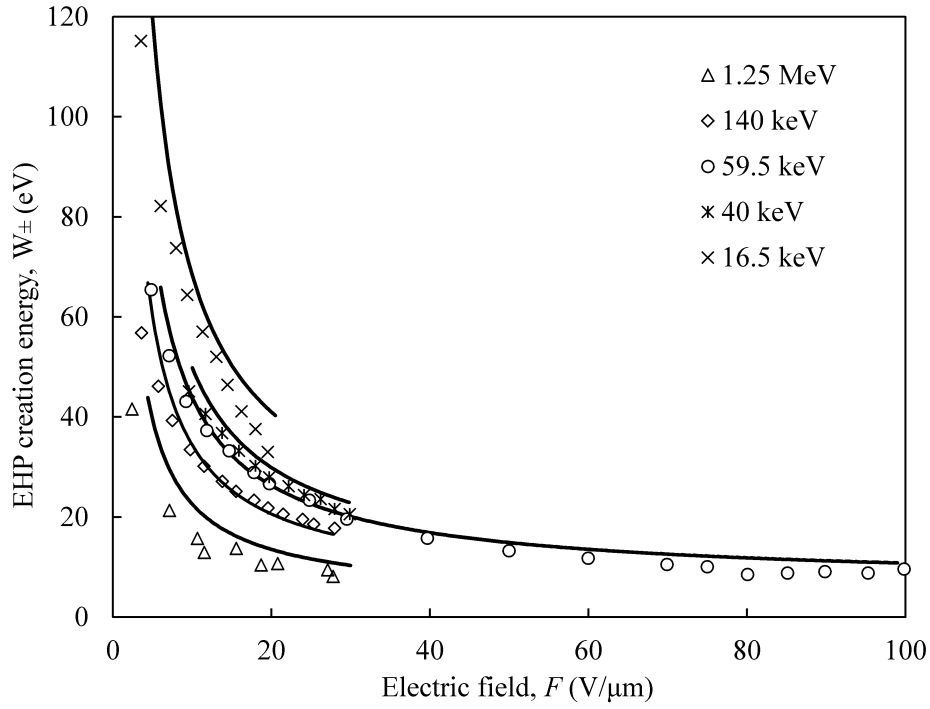


Figure 2.3 EHP creation energy, W_{\pm} of a-Se as a function of electric field at different x-ray energies. The symbols are the experimental results that are extracted from Ref. [70] [71] [72] [73]. Table 2.1 shows the basic physical properties of different photoconductors.

Table 2.1 Physical properties of potential photoconductors [38].

Material	Atomic number	Density (g/cm ³)	Electric field (V/μm)	Bandgap (eV)	EHP creation energy, W_{\pm} (eV)
a-Se	34	4.27	10	2.2	42
PbI ₂	82/53	6.2	2	2.3	5
PbO	82	9.8	4	1.9	9-20
TlBr	81/35	7.56	1	2.7	6.5

2.3.2 W_{\pm} in scintillators or phosphors

In indirect conversion detectors, the scintillators absorb the x-rays and emits visible light photons. Figure 2.4 shows the process of production of light photons in a scintillator. The x-ray photons excite the electrons in the scintillator from the valance band to the conduction band. These excited electrons move freely for a short distance and come back to the valance band through a local state. The local states are created by adding some impurities, known as activators. In order to return to the valance band, the electrons emit radiant energy in form of visible light photons. However, some electrons directly return to the valance band without emitting any light. The value of W_{\pm} identifies the total number of emitted light photons by an x-ray.

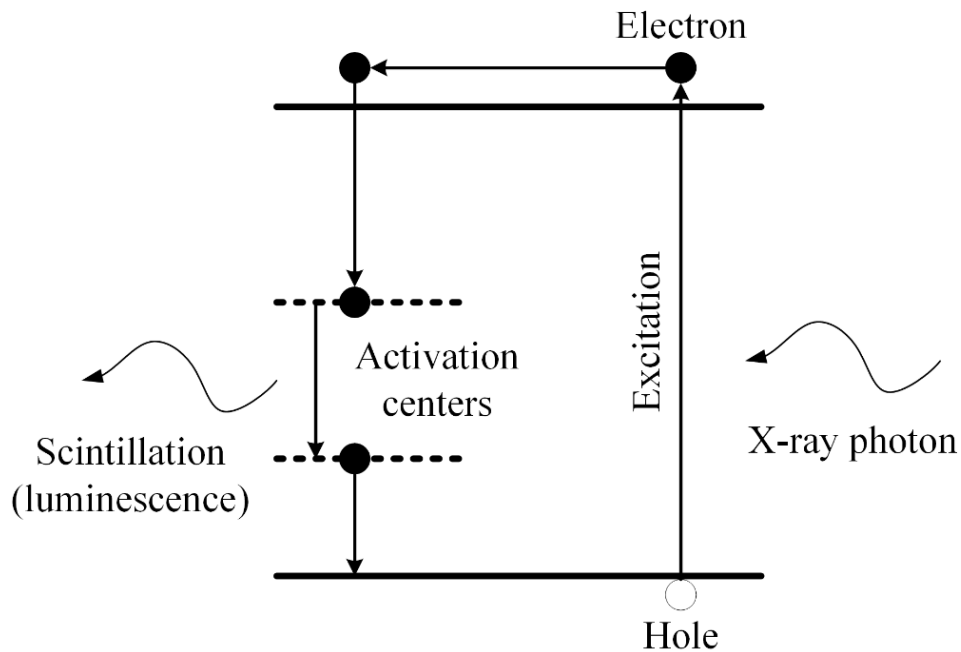


Figure 2.4 Energy band diagram of a scintillator (or phosphor) showing excitation and scintillation.

Some phosphors (e.g., CaWO_4) can emit light without activators. These phosphors are called to be luminescence. The activators play an important role in the phosphors. The peak wavelength and intensity of the emitted light depends on the type of added activator or impurities. For example, the peak wavelength in $\text{Gd}_2\text{O}_2\text{S}$ shifts from 545 nm (green light) to 626 nm (red light) when $\text{Tb}_2\text{O}_2\text{S}$ and $\text{Eu}_2\text{O}_2\text{S}$ are used as activators, respectively. The same phosphor ($\text{Gd}_2\text{O}_2\text{S}$) emits light with wavelength peak at 506 nm when praseodymium is used as activator [74]. Apart from selecting peak wavelength, the activators have influence over the value of W_{\pm} of a phosphor. The most commonly used phosphor, CsI is doped with small concentration of thallium iodide (CsI:Tl) to improve its scintillating properties. Table 2.2 shows the atomic number, density and the value of W_{\pm} of different phosphors.

Table 2.2 Physical properties of different phosphors [38].

Material	Atomic number	Density (g/cm^3)	Optical photon creation energy, W_{\pm} (eV)
CaWO ₄	74	6.06	33
Gd ₂ O ₂ S:Tb	64	7.34	17
CsI:Na	55/53	4.51	25
CsI:Tl	55/53	4.51	18

2.4 Impact ionization

Unlike many amorphous materials, a-Se shows impact ionization of holes at reasonable high electric fields ($\sim 70 \text{ V}/\mu\text{m}$). Impact ionization in a-Se has been investigated using modified lucky drift (LD) model [57] [75] [76]. An empirical expression is also used to estimate the ionization coefficient of holes within a limited range of electric field (up to $\sim 110 \text{ V}/\mu\text{m}$) where avalanche

multiplication is observed [48]. The expression is

$$\beta = \beta_1 e^{-\beta_2/F}, \quad (2.4)$$

where F is the electric field across the photoconductor, β_1 and β_2 are the fitting parameter. The best fitting values of β_1 and β_2 are $1.1 \times 10^4 \mu\text{m}^{-1}$ and $1.09 \times 10^3 \text{ V}/\mu\text{m}$, respectively [48].

2.5 Shockley-Ramo Theorem

Once an EHP is created due to x-ray interaction in a photoconductor, the electron and hole start travelling towards the electrodes under the influence of the applied electric field. The direction of the charge carriers depends on the direction of the electric field. The holes travel in the direction of the electric field and the electrons travel in the opposite direction. In doped semiconductors or ionic materials, there are plenty of free charges to surround a moving charge. The surrounding charges effectively screen out the electric field lines of the moving charge. Therefore, the field lines are not terminated at the electrode and at the same time, the local charge neutrality is maintained. As a result, the charge cannot contribute to the output current while it is travelling inside the semiconductor. It contributes to the current only when it is collected by the electrode. However, in large bandgap photoconductors, the amount of free charges is not enough to surround the moving charge and the local charge neutrality is not maintained. The electrodes sense current while the charges created due to x-ray interaction move along their paths. The current induced by the charges to the electrodes is called as induction current. The Shockley-Ramo theorem allows to calculate the induction current due to the motion of a charge carrier in a photoconductor [77].

According to the theory, the induced charge (Q_i) and current (I_i) due to the motion of charge q are [78]

$$Q_i = -qV_w(x) \quad (2.5)$$

$$I_i = qvF_w(x) \quad (2.6)$$

where, $v (= \mu F)$ and x are the velocity and the position of the charge, μ is the charge carrier mobility and F is the applied field. F_w and V_w are the weighting field and the potential of the charge collecting electrode. F_w and V_w are the existing field and potential across the device, respectively, when the potential of the electrode of interest is raised to unity, the potential of rest of the electrodes are set to zero and all charges are removed.

For example, the induced charge due to the movement of a point charge from x_1 and x_2 (as shown in Figure 2.5)

$$Q_{i(x_1 \rightarrow x_2)} = -(Q_{ix_2} - Q_{ix_1}) = q[V_w(x_2) - V_w(x_1)] \quad (2.7)$$

The weighting potential and field of large-area pixel are given by $V_w(x) = x/L$ and $F_w(x) = 1/L$, respectively, where L is the thickness of the photoconductor. Thus, in a large-area pixel, the induction current due to a charge carrier originating inside the photoconductor is qv/L . According to Equation 2.7, the total charge induced by a positive point charge in a large area pixel when it travels from x_1 to x_2 is

$$Q_{i(x_1 \rightarrow x_2)} = -(Q_{ix_2} - Q_{ix_1}) = q \frac{(x_2 - x_1)}{L} \quad (2.8)$$

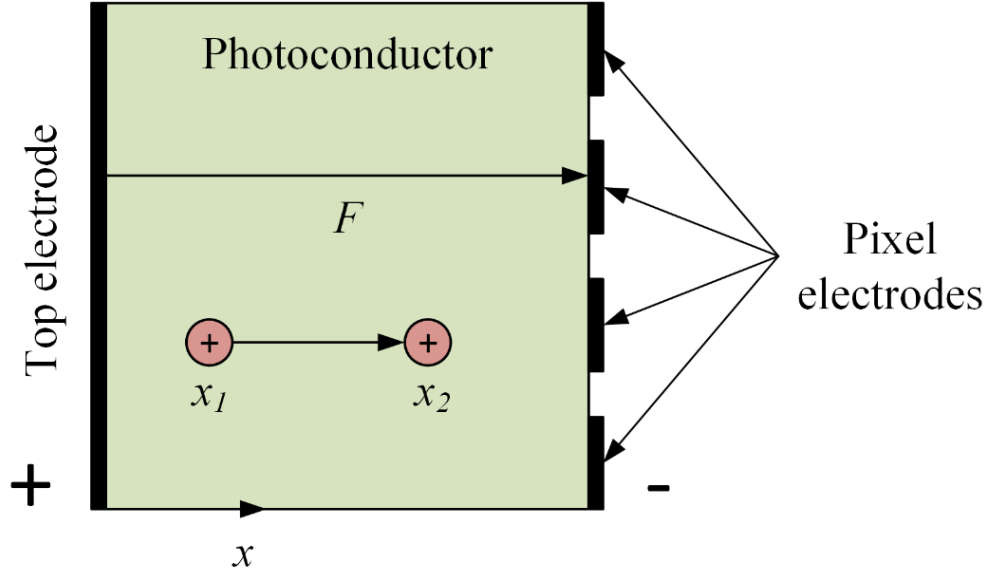


Figure 2.5 Schematic of an x-ray detector with pixel electrodes. The top electrode is the radiation receiving electrode and it is positively biased and the pixel electrodes are negatively biased. Therefore photo-generated hole travels from x_1 and x_2 (in the direction of the electric field) and induces charge on the electrodes.

Therefore, when an electron or hole travel a certain distance before getting trapped, it induces a portion of the total charge. Considering carrier trapping, the average electron and hole currents become $i_e = (qv_e/L) \exp(-t/\tau_e)$ and $i_h = (qv_h/L) \exp(-t/\tau_h)$, respectively, where τ is the carrier lifetime and the subscripts e and h stand for electron and hole, respectively. Since, both electron and hole contribute to the current, the average collected charge at an electrode is

$$\begin{aligned}
 Q(x) &= \int_0^{t_e} i_e(t) dt + \int_0^{t_h} i_h(t) dt \\
 &= \frac{q\mu_e\tau_e F}{L} \left[1 - e^{-x/\mu_e\tau_e F} \right] + \frac{q\mu_h\tau_h F}{L} \left[1 - e^{-(L-x)/\mu_h\tau_h F} \right]
 \end{aligned} \tag{2.9}$$

where $t_e = x/\mu_e F$ and $t_h = x/\mu_h F$ are the time required for electron and hole to reach to the positive and negative electrodes, respectively and F is the applied electric field. This equation is known *Hecht equation* which evaluates the average charge collection.

2.6 Dark current

In direct and indirect conversion detectors, the charge collection layers are the photoconductor and photodiode, respectively. A voltage is applied to create an electric field inside the charge collection layer to collect the generated charges. Due to the applied voltage, a small current flow across the device. This current which flows without x-ray irradiation or shining light is known as dark current. The dark current is a source of noise and it reduces the dynamic range of the x-ray detectors. Therefore, it is in the best interest to reduce the dark current in the detectors.

The noise due to dark current is the result of random injection and/or generation of charge carriers in the charge collection layer. The noise in the dark current is estimated by the Poisson fluctuation. Therefore, if the dark current density is J_d , pixel area is A_{pixel} and charge integration period is T_{int} , the noise due to dark current is [79]

$$N_d = \sqrt{\frac{J_d A_{pixel} T_{int}}{q}} \quad (2.10)$$

The value of N_d should be less than other sources of electronic noise, such as kTC noise (i.e., thermal charge fluctuation in TFT) [38], $1/f$ (i.e., conductivity fluctuation due to the contacts in

the amplifiers) [80]. Considering the electronic noise to be 1000 e/pixel, integration period to be 1 sec, and pixel area to be 85 μm , the dark current should be less than 1.8 pA/mm².

During integration period, the x-ray generated charges are stored in the pixel capacitor. However, if the dark current is high, then the pixel capacitor would be left with less space for the x-ray generated charges. As a result, the dynamic range of the detector is adversely affected.

The main source of dark current in x-ray detectors is charge carrier injection from the metal contacts [81]. The carrier injection takes place at the contacts which are blocking in nature. The blocking contact is also known as Schottky contact. Carrier injection from the contacts is governed by Schottky emission [82]. The injected carriers move in the photoconductor by drift and diffusion mechanisms. Due to the applied high potential, the drift component of the injected carriers is stronger than the diffusion component. Therefore the electron injection current density is given by [50][82]

$$J_{inj,e}(t) = qN_c v_{de}(t) \left[\frac{v_r}{v_r + v_e} \right] \exp \left\{ -\frac{\varphi_e - \Delta\varphi_e(F)}{k_B T} \right\} \quad (2.11)$$

and hole injection current density is

$$J_{inj,h}(t) = qN_v v_h(t) \left[\frac{v_r}{v_r + v_h} \right] \exp \left\{ -\frac{\varphi_h - \Delta\varphi_h(F)}{k_B T} \right\} \quad (2.12)$$

where N_c and N_v are the effective density of states in the conduction and valance bands, respectively, $v (= \mu F)$ is the instantaneous drift velocity, $v_r (= A^* T^2 / q N_c)$ is the thermal velocity, A^* is the Richardson constant, φ is the effective barrier height from metal to photoconductor.

Assuming $A^*=120 \text{ A/cm}^2/\text{K}^2$, $T=300 \text{ K}$ and $N_C = 10^{19} \text{ cm}^{-3}$, the thermal velocity in a-Se becomes $\sim 6.5 \times 10^6 \text{ cm/s}$ whereas at electric field of $10 \text{ V}/\mu\text{m}$, the drift velocity of the faster carrier (i.e., holes, $\mu_h = 0.12 \text{ cm}^2/\text{V-s}$) in a-Se is $1.2 \times 10^4 \text{ cm/s}$. At operating electric field, the magnitude of the thermal velocity is two order more than the drift velocity. Therefore, the injection current is dominated by drift velocity of the injected carriers. In Equation 2.11 and 2.12, the term $\Delta\phi(F)$ represents the field dependent barrier lowering. The effective barrier may be lowered by the rearrangement in the interfacial layer, image force barrier lowering, and/or thermally assisted tunneling. Figure 2.6 shows a schematic representation of barrier lowering at metal/photoconductor junction. The following expression is used to evaluate the barrier lowering [82].

$$\Delta\phi(F) = \sqrt{\frac{q^3 F}{4\pi\epsilon_s}} + q\alpha_i F^2 \quad (2.13)$$

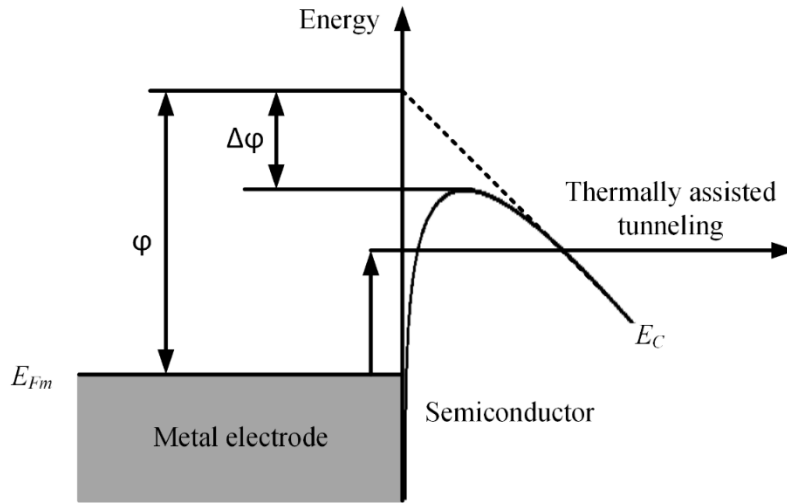


Figure 2.6 Illustration of charge carrier injection from metal electrode to semiconductor. E_C and E_{Fm} are the conduction band energy of the semiconductor and Fermi level in metal electrode.

The first term of Equation 2.13 incorporates the image force barrier lowering and the second term includes the effect of thermally assisted tunneling. The expression for α_t is determined by considering the tunneling probability through a triangle potential barrier and Boltzmann occupation probability and is given by [82],

$$\alpha_t = \frac{q\hbar}{24m^*(k_B T)^2} \quad (2.14)$$

where \hbar ($=1.054 \times 10^{-34}$ J-s) is the modified plank constant and m^* is the effective mass of the photoconductor. The tunneling probability increases when the carriers gain thermal energy. It is because the thermally activated carriers face a thinner barrier (shown in Figure 2.6) and thus the probability of tunneling increases.

2.7 Modulation transfer function

The modulation transfer function (MTF) is the spatial response of an active matrix flat panel imager. In other words, the MTF estimates the efficiency of a detector to resolve information with different spatial frequencies. In medical imaging, the objects with different sizes and opacity are imaged with different gray values. The MTF shows how well an x-ray detector can convert the contrast values of objects with different sizes into contrast intensity levels in the final x-ray image.

Figure 2.7 shows an example of MTF of an imaging system at three different spatial frequencies. The image consists of a periodic array of black and white stripes and the thicknesses of both kinds of stripes are equal. In Figure 2.7 A, the input image has a pair of stripes in 1 mm, whereas in

Figure 2.7 B and C, there are 2 and 4 pairs of stripes, respectively, in 1 mm. Therefore, the resultant spatial frequencies are 1, 2 and 4 line pairs per mm (lp/mm) in Figure A, B and C, respectively. The detector in the example resolves 100% of the input signal when the spatial frequency is 1 lp/mm. The same detector resolves less than 100% when the spatial frequency is 2 lp/mm and fails to resolve the input information when frequency is 4 lp/mm.

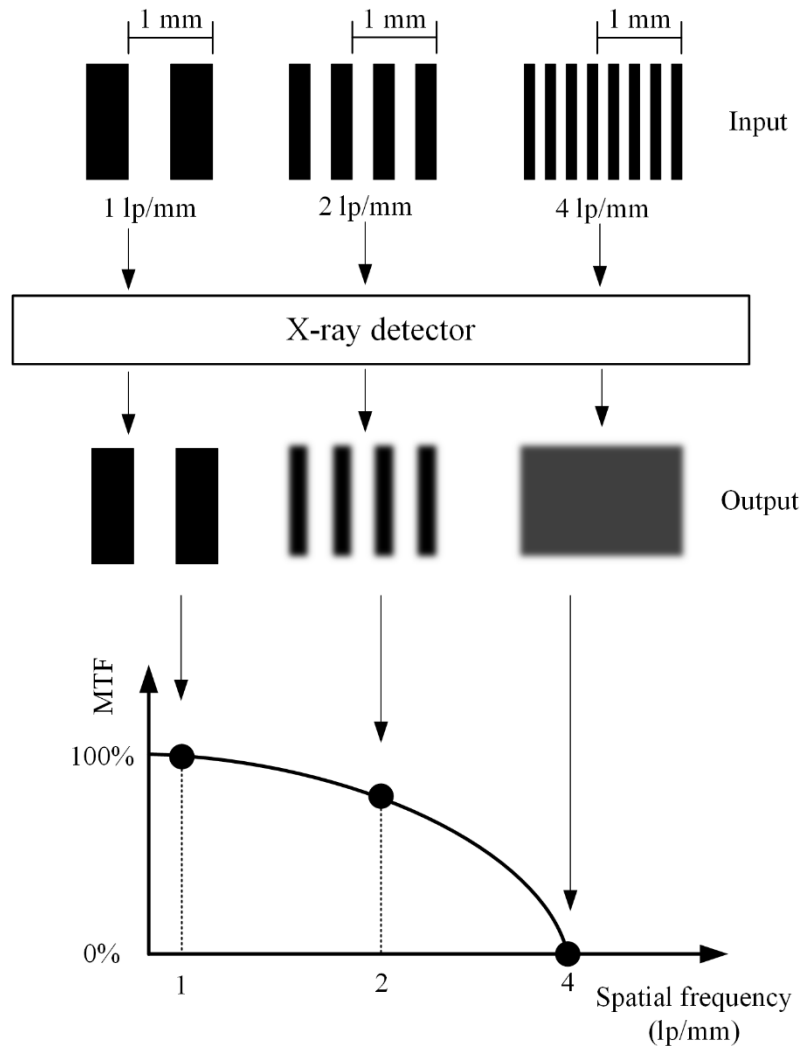


Figure 2.7 Modulation transfer function of an x-ray detector at different spatial frequencies. The detector resolves the input image ~100% of the input image when its spatial frequency is 1 lp/mm.

At a spatial frequency of 2 lp/mm, the detector resolves less than 100% and at 4 lp/mm, the input information is totally lost at the output.

There are two methods to measure the MTF of a detector, namely, slit and edge methods. The slit method is used to measure the line spread function (LSF) and the edge method is used to measure the edge spread function (ESF) [83]. The ESF is the integral of LSF. The LSF is response of a detector to a narrow slit. The modulus of the Fourier transform of the LSF is the MTF of the system. The MTF is normalized to unity at zero frequency. On the other hand, an edge device is used to measure the ESF. The calculated ESF is differentiated to obtain the LSF and then the Fourier transform of the LSF gives the MTF of the system. The edge method is cost effective compared to the slit method because a test device with a narrow slit is more expensive than a straight edge device. Moreover, the edge method is not vulnerable to physical defects, radiation scattering and misalignment.

The MTF of a digital x-ray detector is comprised of two components, namely, presampling and digital components. The presampling MTF includes the geometric blurring, photoconductor or scintillator blurring and aperture blurring. The geometric blurring is caused by the focal spot of the x-ray source. It is eliminated by placing test device close to the detector surface (to remove magnification). The aperture blurring is due to averaging the signal over the aperture a pixel. The aperture of a pixel is assumed to be the area of the charge collecting electrode (pixel electrode). Figure 2.8 shows pixels with square apertures. The pixel pitch is the distance between the centres of two adjacent pixels. The MTF due to pixel aperture, MTF_a is given by

$$\text{MTF}_a(f) = |\text{sinc}(af)| = \left| \frac{\sin(\pi af)}{\pi af} \right| \quad (2.15)$$

Figure 2.8 also shows the spatial frequency dependent $\text{MTF}_a(f)$. The first zero occurs at $f = 1/a$.

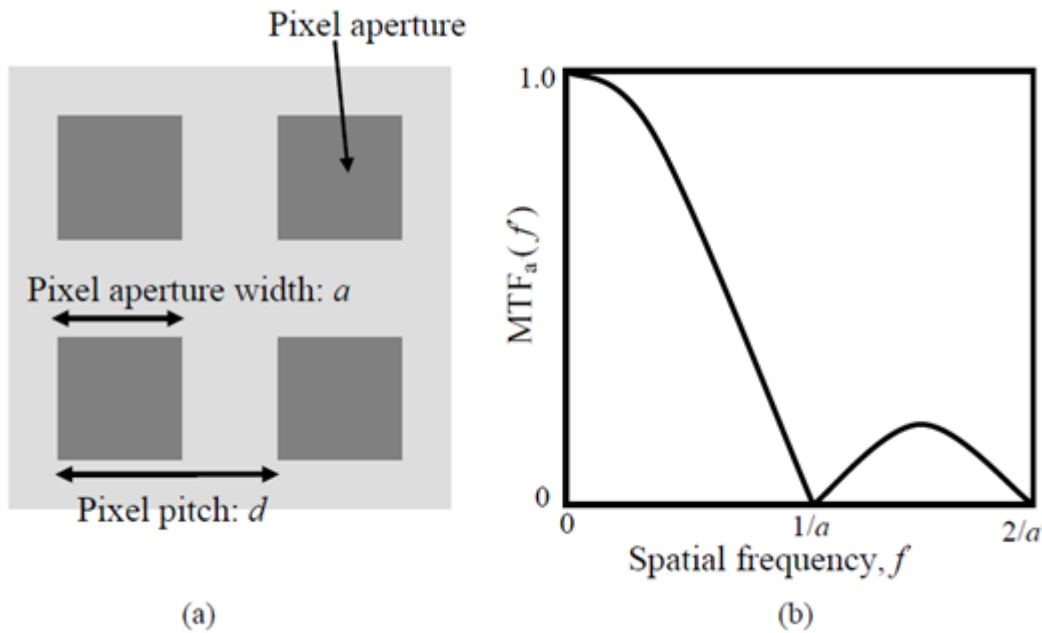


Figure 2.8 a) The top view of a bare TFT (without photoconductor/scintillator) showing pixel aperture width and pixel pitch, b) MTF due to aperture function [84].

The overall MTF of x-ray detectors also includes the blurring due to sampling. It is evaluated from the convolution between the presampling MTF and the Fourier transform of the sampling function. The convolution shows the response of the detector to a delta function. Any signal component at frequency higher than half of the sampling frequency, called Nyquist frequency (f_N), causes aliasing. The overall MTF becomes higher at frequencies lower than f_N due to overlapping of the replicated spectra. Therefore, the MTF performance of two different digital detectors are compared

using presampling MTFs. However, in analog x-ray detectors, the overall MTF is not affected by undersampling (i.e., aliasing).

2.8 Noise power spectrum

By definition, NPS is given by the Fourier transform of the covariance of a random signal. In other words, NPS represents the spectral decomposition of noise power as a function of frequency in an x-ray image. In digital detectors, the NPS is calculated by performing the discrete space Fourier transform of the autocovariance of the random output signal intensity [85]. The autocovariance of a random variable evaluates the covariance of the variable with itself at a different location. The output signal intensity of an x-ray detector is assumed to be wide-sense-stationary (i.e., mean and covariance are space invariant). Therefore, the NPS is called Wiener spectrum.

The impinged x-ray photons are assumed to be uncorrelated. As a result, the NPS of the incoming x-ray distribution is constant and equal to the mean incident x-ray fluence. However, the output signal intensity has both correlated and uncorrelated components. Therefore, the NPS of the output signal may show frequency dependency. The effect of aliasing mentioned in the previous section, is also applicable to the interpretation of NPS. The NPS of a digital x-ray detector is comprised of primary quantum noise, excess Poisson noise, secondary quantum noise, structure noise, aliasing and electronic noise originating from the readout circuitry [86].

The primary quantum noise arises from the fluctuation in the number of absorbed x-ray photons in the photoconductor or scintillator. The number of x-ray photons impinged on the detector

surface and the number of absorbed photons is random in nature and follow Poisson distribution. Therefore, even if a specific body part attenuates incoming x-ray constantly, the average number of x-ray photons appearing over a detector surface would vary from location to location.

Excess Poisson noise arises in the detector due to the fluctuation in the number of secondary quanta (EHP in direct conversion detectors and light photon in indirect conversion detectors) created by per primary quanta (i.e., x-ray photon). Therefore, this noise given by the ratio between excess noise and primary quantum noise.

The secondary quantum noise occurs when the secondary quanta are converted. It is a Poisson noise and the level of this noise depends on the conversion efficiency of the scintillator, escaping probability of light photons and coupling efficiency between scintillator and photodiode and the quantum efficiency of the photodiode for the emitted light spectrum from the scintillator.

The structure noise is a fixed pattern noise. It can arise due to gain variation in the conversion layers. The source of this noise includes phosphor screen granularity, non-uniformity in the coupling between scintillator and photodiode thickness variation of the photoconductors etc.

Both signal and noise of digital detectors, are affected by aliasing. When aliasing occurs, the frequency components more than the Nyquist frequency are folded around this value and added to their counterpart frequencies below the Nyquist frequency. Therefore, it is not possible to distinguish the added components from the frequencies below the Nyquist frequency. The additive

electronic noise is independent from the x-ray exposure. It is mainly caused by dark current density, noise from the readout circuitry (i.e., kTC noise) and gain variation in the charge amplifiers.

2.9 Detective quantum efficiency

The detective quantum efficiency (DQE) evaluates the signal (related to the MTF) and noise performance of x-ray imaging detectors as a function of spatial frequency. The image quality of the x-ray detectors is quantitatively measured by output signal to noise ratio (SNR). A higher signal contrast compared to the noise, ensures a better image quality. The SNR of x-ray detectors improves when the x-ray exposure and quantum efficiency are increased, and sources of random noise is minimized. The input signal has the highest SNR and given by [87]

$$\text{SNR}_{\text{in}} = \frac{\phi_i}{\sqrt{\phi_i}} = \sqrt{\phi_i} \quad (2.16)$$

when the mean input x-ray quanta is ϕ_i . The $\text{DQE}(f)$ shows the efficiency of x-ray detectors to transfer the input SNR at different spatial frequencies to the detector output [86]. The $\text{DQE}(f)$ is defined by the following equation [87],

$$\text{DQE}(f) = \frac{\text{SNR}_{\text{out}}^2(f)}{\text{SNR}_{\text{in}}^2(f)} \quad (2.17)$$

where SNR_{in} and SNR_{out} are the SNR of the input and output signals, respectively. An ideal detector would have a unity DQE at all relevant spatial frequencies. However, when only quantum noise is considered and all other sources of noise and blurring are disregarded, the output signal

and noise of an x-ray detector become $\eta\phi_i$ and $\sqrt{\eta\phi_i}$, respectively. Thus, SNR_{out} becomes $\sqrt{\eta\phi_i}$ and the DQE becomes η [18]. When there are other sources of noise exist in the detector, the DQE reduces below η as if a smaller number of x-ray quanta is used to construct the output image.

For simplicity, DQE at zero spatial frequency, $\text{DQE}(0)$ is often calculated to characterize different x-ray detectors. $\text{DQE}(0)$ represents the efficiency of detectors to transfer SNR from input to output without considering any blurring mechanism. The $\text{DQE}(f)$ can be given in terms of $\text{DQE}(0)$ by the following equation [87],

$$\text{DQE}(f) = \frac{\text{DQE}(0)\text{MTF}^2(f)}{\text{NNPS}(f)} \quad (2.18)$$

where NNPS is the NPS of x-ray detectors normalized to unity as f approaches to zero.

CHAPTER 3

Impact of Lubberts effect on amorphous selenium indirect conversion avalanche detector for medical x-ray imaging

The contribution of this chapter has recently been published [88]. Most of the materials are taken from the published manuscript.*

A cascaded linear-system model is proposed for CsI based indirect conversion a-Se avalanche x-ray detectors. The depth dependent MTF and NPS are modelled by incorporating the Lubberts effect. The MTF for *K*-fluorescence reabsorption is calculated by determining the LSF and subsequent one-dimensional Fourier transform. The optimal design parameters and operational condition for CsI scintillator-based avalanche x-ray detectors are described in this work. The required avalanche gain in a-Se layer to overcome the electronic noise is calculated. The model offers more physical insight for the explanation of the experimental results, and therefore, helps to optimize the design for improving the performance of the CsI based avalanche x-ray detectors. The theoretical model is compared with the experimental results and shows a better fit than the previously published models.

*S. M. Arnab, & M. Z. Kabir, "Impact of Lubberts Effect on Amorphous Selenium Indirect Conversion Avalanche Detector for Medical X-Ray Imaging," *IEEE Transactions on Radiation and Plasma Medical Sciences*, vol. 1, pp. 221, 2017

3.1 Introduction

The flat-panel imagers (FPI) are, at present, the most widely used digital x-ray detectors for mammography and general radiography and are under scrutiny for use in fluoroscopy and portal imaging [30], [89]. The FPIs are generally either phosphor based (indirect conversion), in which x-ray energy is converted into light photons in phosphor layer (mostly cesium iodide, CsI) and these light photons are then detected by a photodiode, or photoconductor based (direct conversion), in which x-ray photons directly generate electron and hole pairs, EHPs, in the photoconductor layer (generally amorphous selenium, a-Se) [6][29][90].

The detective quantum efficiency (DQE) is the most comprehensive measure of the detector performance, which represents the signal to noise (SNR) transfer efficiency for different frequencies of information in an image. The optimal image quality can only be achieved by ensuring the DQE is maximized over all spatial frequencies of importance [38]. The DQE may be degraded by many factors, such as low conversion gain, scattering of optical quanta and charge carriers, and additive electronic noise of the active matrix arrays (AMA) [91].

The DQE is degraded severely at low exposure applications (e.g., average dose in fluoroscopy is 1 μ R per frame) by the electronic noise [92]. As a result, the FPI does not remain quantum noise limited. Therefore, the reduction of electronic noise has been a key issue in last two decades in order to maximize the DQE

The AMA is made of either amorphous silicon (a-Si) thin film transistors (TFTs) or silicon CMOS.

There are two types of AMA; (i) passive pixel sensor (PPS) that consists of single transistor per pixel and (ii) active pixel sensor (APS) consisting three transistors per pixel. The electronic noise in a-Si APS is ~ 700 e per pixel of $200 \mu\text{m}$ pixel size, which is 2-4 times lower than the existing a-Si PPS FPIs [93]. The CMOS APS shows almost an order of magnitude lower electronic noise (per pixel) than a-Si technology in very small pixel sensors (pixel size of $\sim 25 \mu\text{m}$) [94]. However, larger CMOS APS sensor shows higher electronic noise (e.g., ~ 300 e for pixel size of $96 \mu\text{m}$ [95]). For real-time large area applications, binning mode of operation is usually used for faster readout [96]. For example, 2×2 binning mode of $96 \mu\text{m}$ CMOS APS is almost equivalent to the pixel size of $\sim 200 \mu\text{m}$ having an equivalent electronic noise of 1200 e (4×300 e) per pixel. Therefore, a variation of electronic noise from 700 to 1500 e per pixel of size $200 \mu\text{m}$ for large area real-time applications is reasonable at present standard.

An extensive research is underway to design viable indirect FPIs for real-time imaging and low dose applications. A uniform layer of a-Se with high electric field, called high gain avalanche rushing photoconductor (HARP), amplifies signal before readout to surpass the effects of electronic noise and improves the DQE [63]. Previous studies show that indirect conversion approach is more suitable compared to direct conversion for avalanche x-ray detectors [97].

The resolution (in terms of modulation transfer function, MTF) and noise power spectrum (NPS) of the detector strongly depend on the absorption depth of the incident x-ray photons [98]. The exponentially distributed absorption profile results a significant deterioration of MTF at higher spatial frequencies, which is known as Lubberts effect [99][100][101].

In previous linear-system models, Lubberts effect is not considered and the blurring caused by the optical photons has been taken into consideration by using empirical equation or directly feeding the mismatch between theoretical and experimental results [102], [103], [104]. W. Zhao et al. [104] modeled MTF due to K -fluorescence reabsorption and separated it from the total presampling MTF in order to predict the optical blurring. However, the latter model fails to fit the experimental results at higher spatial frequencies. These models are based on empirical equations and do not provide complete explanation of the physics behind the inherent imaging characteristics of the scintillators. Badano et al. [99] described a method to estimate the Lubberts effect in columnar CsI using Monte Carlo simulation but they did not show its effect on DQE.

3.2 Structure of indirect conversion avalanche x-ray detector

A thin HARP layer is coupled with the x-ray scintillator (e.g., CsI) to detect optical photons [102]. There are two types of CsI available. One provides high resolution (HR) and the other provides high light output (HL) [104]. The HL CsI has a reflective layer at the x-ray entrance side, which reflects back the light photons that travel towards the x-ray entrance side. Although HR CsI provides a better resolution, the HL CsI provides ~40% more light and hence gives a higher DQE than the HR CsI. Therefore, HL CsI is mostly used in commercial x-ray detectors [104]. In this paper, we consider HL CsI.

The HARP structure consists of an intrinsic layer of a-Se sandwiched between a hole and an

electron blocking layers. The blocking layers are used to reduce carrier injection hence reducing the dark current [105]. The HARP substrate consists of a transparent indium tin oxide (ITO), which acts as the positive electrode. Then the negative electrode which is segmented into an array of individual square pixels of size $a \times a$ is situated on top of the electron blocking layer. The distributed resistance layer (DRL) is placed on top of electron blocking layer to minimize the electric field near the electrode edge [106]. The applied bias across the electrodes creates an electric field (F) in the a-Se layer. The structure of indirect conversion avalanche x-ray detector is shown in Figure 3.1.

3.3 Theory

The effect of x-ray spectrum on detectors can conveniently be determined by the average energy (E) of the spectrum [92]. The incident x-rays are absorbed exponentially across the CsI thickness and create optical photons. The x-ray photon fluence is ϕ_0 . The probability density for an x-ray photon to be absorbed at a distance x_1 from the top surface (radiation receiving surface) is given by [92],

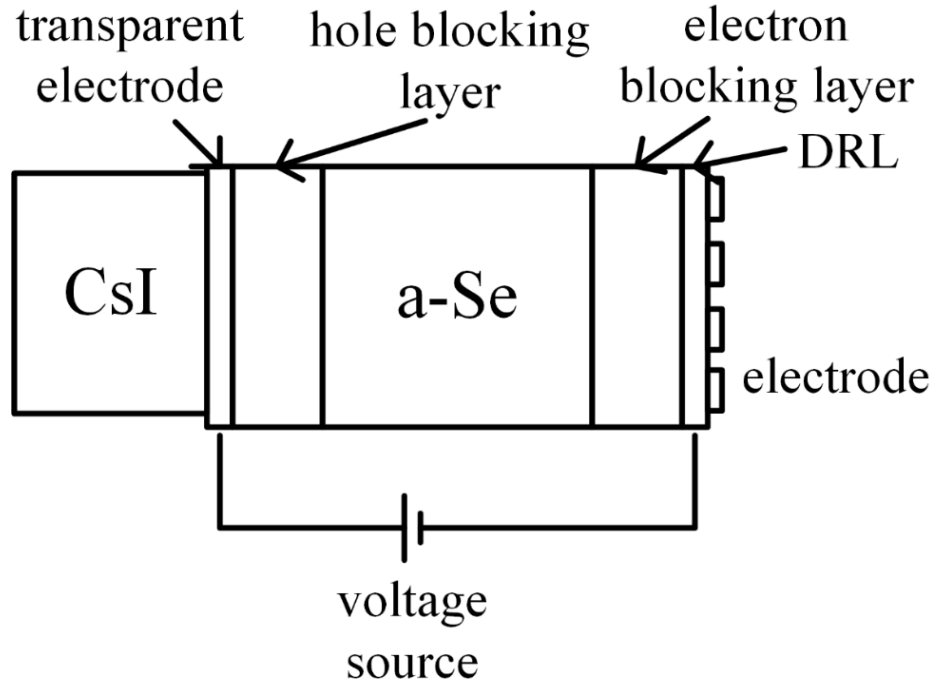


Figure 3.1 Cross sectional diagram showing an indirect FPI with CsI scintillator and a-Se HARP layer.

$$P_{x_1}(E, x_1) = \begin{cases} \frac{\alpha_{CsI} e^{-\alpha_{CsI} x_1}}{\eta}, & 0 \leq x_1 \leq L_1 \\ 0, & elsewhere \end{cases} \quad (3.1)$$

where $\eta = 1 - \exp(-\alpha_{CsI} L_1)$ is the quantum efficiency, α_{CsI} and L_1 are the linear attenuation coefficient and thickness of the CsI layer, respectively.

3.3.1 MTF due to K -fluorescence reabsorption

When the incident x-ray energy is above the K shell energy of CsI, one or more characteristics x-

rays known as K -fluorescent x-rays may be created [91]. Some of the K -fluorescent x-rays can be reabsorbed at random distances from the primary photon interaction site, which causes a lateral spreading of signal.

The LSF is calculated by considering normal incident of x-rays on the detector along the x_1 -axis at $x_1=0$ as shown in Figure 3.2. The one-dimensional Fourier transform of the LSF can be written as [91],

$$G_1(f) = \frac{\alpha_K}{2\eta} \int_0^{L_1} \int_0^{\infty} \frac{e^{-\alpha_K \sqrt{r^2 + \beta^2}}}{r^2 + \beta^2} \times \left[1 + e^{-\alpha_{CsI}\beta} - e^{-\alpha_{CsI}L} (1 + e^{-\alpha_{CsI}\beta}) \right] r J_0(2\pi fr) dr d\beta \quad (3.2)$$

where $r^2 = y_1^2 + z_2^2$, and $\beta = x_1 - x_2$. J_0 is the zero-order Bessel function. The MTF due to K -fluorescent x-ray is,

$$T_K(f) = G_1(f)/G_1(f=0) \quad (3.3)$$

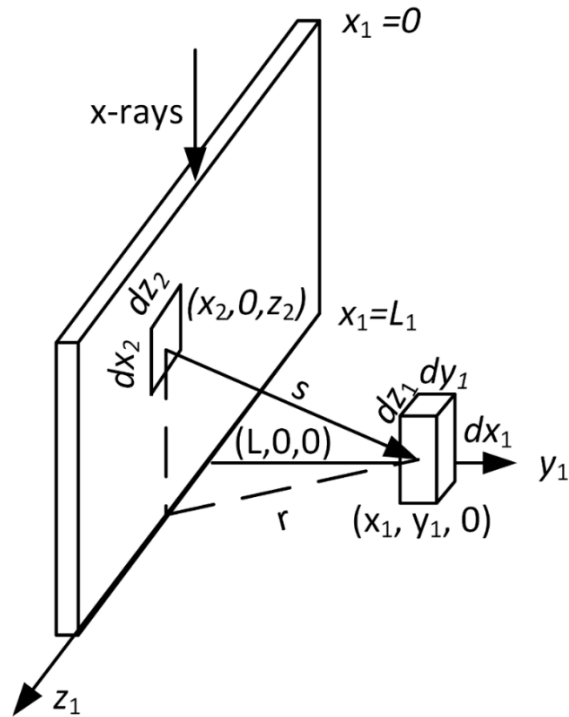


Figure 3.2 Schematic diagram for calculating the LSF due to K -fluorescence reabsorption.

3.3.2 MTF due to optical scattering with Lubberts effect

The incident x-rays are absorbed at different depths inside the CsI layer. Therefore, the light photons travel different distances before they are collected by the photodetector. The random variation in light transport process affects the signal and noise transfer through the CsI screen and, as a result, a significant light spreading (Lubberts effect) is observed. Badano et al. [99] found almost identical Lubberts fraction considering columnar (CsI:Tl) and granular (Gd₂O₂S:Tb) phosphor model using their Monte Carlo simulation and suggested that high scattering coefficient is required because of highly irregular columnar structures in CsI. Therefore, we have used the

original Swank's scattering model [101] for this Lubberts effect. The depth (x_1) and spatial frequency dependent screen gain, defined by Swank, is given by [101],

$$G_2(f, x_1) = \frac{\kappa\rho_1 \left\{ (t + \kappa\rho_0)e^{tx_1} + (t - \kappa\rho_0)e^{-tx_1} \right\}}{(t + \kappa\rho_0)(t + \kappa\rho_1)e^{tL_1} - (t - \kappa\rho_0)(t - \kappa\rho_1)e^{-tL_1}} \quad (3.4)$$

where κ is the reciprocal of the relaxation length of the photon (this parameter describes scattering and absorption occurring in the CsI layer), $t = \sqrt{h_{CsI}^2 + 4\pi^2 f^2}$ with h_{CsI} being the reciprocal of the mean absorption length of CsI and $\rho_i = (1-r_i)/(1+r_i)$ is the reflectivity of the CsI layer at the entrance ($i=0$) or the output ($i=1$) surfaces. The average gain as function of spatial frequency is calculated by,

$$G_2(f) = \int_0^{L_1} P_{x_1}(x_1) G_2(f, x_1) dx_1 = \frac{\alpha_{CsI} \kappa \rho_1 \left[\begin{aligned} &\left(1 - e^{-L_1(\alpha_{CsI} - t)}\right) \left(\frac{t + \kappa\rho_0}{\alpha_{CsI} - t}\right) \\ &+ \left(1 - e^{-L_1(\alpha_{CsI} + t)}\right) \left(\frac{t - \kappa\rho_0}{\alpha_{CsI} + t}\right) \end{aligned} \right]}{\eta \left[(t + \kappa\rho_0)(t + \kappa\rho_1)e^{tL_1} - (t - \kappa\rho_0)(t - \kappa\rho_1)e^{-tL_1} \right]} \quad (3.5)$$

The scintillator MTF due to Lubberts effect is, $T_{OP}(f) = G_2(f)/G_2(f=0)$.

3.3.3 Signal and noise propagation

A cascaded linear system can predict the MTF, NPS and, DQE as a function of many system parameters. A linear system breaks down a detector into a cascade of serial and parallel simple processes [107]. Figure 3.3 shows the flow diagram of the physical processes involved in the

imaging chain of an indirect conversion detector. The shaded processes are not considered while calculating the imaging performance of CsI scintillator. Here ζ is the probability of K -shell interaction, ω is the probability of K -fluorescence production and f_k is the average reabsorption probability of K -fluorescent x-ray photons within the scintillator volume. Each of the stages in the linear cascaded system is categorized as one of the following five processes; (i) stochastic gain, (ii) stochastic blurring, (iii) deterministic blurring, (iv) aliasing, and (v) addition.

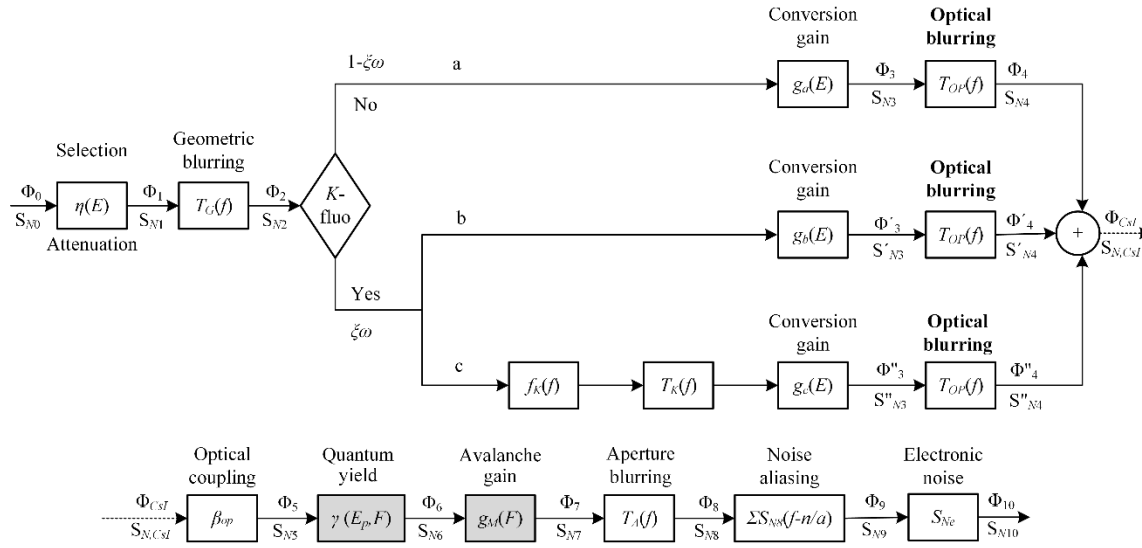


Figure 3.3 Flow diagram showing the propagation of signal and NPS through the stages (shaded stages are not considered when the imaging properties of CsI is calculated) of cascaded linear system model for indirect avalanche x-ray detector.

The output of i^{th} stochastic gain stage having the mean gain g_i and variance $\sigma_{g_i}^2$, is characterized by the following equations [108],

$$\phi_i(E, x) = g_i(E, x) \phi_{i-1}(E, x) \quad (3.6)$$

$$S_{Ni}(E, x, f) = g_i^2(E, x)S_{N(i-1)}(E, x, f) + \sigma_{g_i}^2(E, x)\phi_{i-1}(E, x) \quad (3.7)$$

where $\phi_{i-1}(E, x)$ and $S_{N(i-1)}(E, x)$ are the mean number of input quanta and the NPS of stage i , respectively. The selection, conversion gain, optical coupling, quantum yield and avalanche gain stages in Figure 3.3 are considered to be the stochastic gain stages.

The output of i^{th} stochastic blurring stage is characterized by the following equations [107],

$$\phi_i(E, x, f) = T_i(E, x, f)\phi_{i-1}(E, x, f) \quad (3.8)$$

$$S_{Ni}(E, x, f) = T_i^2(E, x, f)S_{N(i-1)}(E, x, f) + [1 - T_i^2(E, x, f)]\phi_{i-1}(E, x) \quad (3.9)$$

where $T_i(E, x, f)$ is the MTF of the i^{th} stage. Blurring due to K -fluorescence reabsorption and optical blurring with Lubberts effect are considered to be stochastic blurring. The optical blurring stage is added in the cascaded model and thus it is indicated in bold in Figure 3.3.

Deterministic blurring processes do not have random variability. The output of i^{th} deterministic blurring stage is given by the following equations [107],

$$\phi_i(E, x, f) = T_i(E, x, f)\phi_{i-1}(E, x, f) \quad (3.10)$$

$$S_{Ni}(E, x, f) = T_i^2(E, x, f)S_{N(i-1)}(E, x, f) \quad (3.11)$$

Averaging the signal over a pixel area causes a deterministic blurring. The blurring caused by the aperture with dimension a , is determined by the following equation,

$$T_A(f) = |\sin c(af)| = \left| \frac{\sin(\pi af)}{\pi af} \right| \quad (3.12)$$

3.3.4 X-ray photon attenuation (selection)

An x-ray photon either interacts with the scintillator or does not. Therefore, it is a Bernoulli process. According to binomial theorem, the variance of η is $\sigma_\eta^2(E) = \eta(1 - \eta)$ [92].

3.3.5 Conversion gain

The mean conversion gain of CsI is the mean number of optical photons generated after the absorption of x-rays. Once the x-ray photons are absorbed, signal and NPS propagation can be separated into three parallel chains [91];

- (i) K -fluorescent x-rays are not generated, and the total incident energy is converted into optical photons,
- (ii) K -fluorescent x-rays are generated, and remaining energy of the incident x-rays are converted into optical photons, and
- (iii) K -fluorescent x-rays are generated and reabsorbed at a certain distance from the primary x-ray interaction site. The conversion gain of the three parallel paths A, B and C are, respectively,

$$g_a(E) = \frac{E}{W_\pm}, \quad g_b(E) = \frac{(E - E_K)}{W_\pm}, \quad \text{and} \quad g_c(E) = \frac{E_K}{W_\pm} \quad (3.13)$$

where g is the conversion gain of the scintillator, E_k is the average energy of K -fluorescence photons and W_{\pm} is the optical photon creation energy of the scintillator. The fluctuations in conversion gain are caused by the statistical fluctuations of the number of optical photons released per x-ray photon. We assume that the mean number of optical photon released per x-ray photon obeys a Poisson process [91], that is, $\sigma_g^2(E) = g(E)$ in all three branches.

3.3.6 Quantum yield

The optical photons, emitted from the scintillator (CsI), are absorbed within the a-Se layer and create bound EHPs. The quantum yield (known as the fraction of the dissociated EHPs to all the EHPs created) in a-Se is calculated by using Onsager model [109] and given by the following equation [110],

$$\gamma(r_0, F, T) = \frac{e^{-a_1 - b_1}}{b_1} \sum_{l=1}^{\infty} l \left(\frac{b_1}{a_1} \right)^{l/2} I_l(2\sqrt{a_1 b_1}) \quad (3.14)$$

where $a_1 = q^2 / (4\pi\epsilon r_0 k_B T)$, $b_1 = qFr_0 / k_B T$, e is the elementary charge, r_0 is the initial separation between bound EHP, k_B is the Boltzmann's constant, T is the temperature, and I_l is the modified Bessel function.

3.3.7 Avalanche gain

The avalanche gain (g_M) increases along the path of the charge. The avalanche gain and its variation, when only one type of carrier contributes to impact ionization, are given by the following equations [111],

$$g_M = e^{\beta L_2} \quad (3.15)$$

$$\sigma_M^2 = g_M^2 - g_M \quad (3.16)$$

where L_2 is the thickness of the a-Se layer and β is the impact ionization coefficient of hole.

3.3.8 DQE calculation

The DQE is given by,

$$DQE(f) = \frac{SNR_{out}^2(f)}{SNR_{in}^2(f)} \quad (3.17)$$

where SNR_{in} and SNR_{out} are the signal to noise ratio at the input and output stages, respectively.

The expected total signal and NPS at the output of the fourth stage in path a is [92],

$$\phi_4(f) = \phi_o \eta T_G(f) (1 - \xi \omega) g_a T_{OP}(f) \quad (3.18)$$

$$S_{N4}(f) = \phi_o \eta (1 - \xi \omega) g_a [T_{OP}^2(f) g_a + 1] \quad (3.19)$$

where $T_G(f)$ is the MTF due geometric scattering.

In the same way, the expected total signal and NPS at the output of the fourth stage in path b are,

$$\phi'_4(f) = \phi_o \eta T_G(f) \xi \omega g_b T_{OP}(f) \quad (3.20)$$

$$S'_{N4}(f) = \phi_o \eta \xi \omega g_b [T_{OP}^2(f) g_b + 1] \quad (3.21)$$

Similarly, for path c

$$\phi''_4(f) = \phi_o \eta T_G(f) g_c f_K T_K(f) \xi \omega T_{OP}(f) \quad (3.22)$$

$$S''_{N4}(f) = \phi_o \eta \xi \omega f_K g_c [T_{OP}^2(f) g_c + 1] \quad (3.23)$$

The cross correlation between path b and c is given by [107],

$$S_{bc}(f) = \phi_o \eta \xi \omega g_b g_c f_K T_{OP}^2(f) T_K(f) \quad (3.24)$$

Therefore, the signal and NPS at the output of the scintillator are,

$$\phi_{Csl}(f) = \phi_4(f) + \phi'_4(f) + \phi''_4(f) \quad (3.25)$$

$$S_{N,Csl}(f) = S_{N4}(f) + S'_{N4}(f) + S''_{N4}(f) + 2S_{bc}(f) \quad (3.26)$$

After aperture blurring, the signal and NPS becomes,

$$\phi_8(f) = \beta \gamma g_M T_A(f) \phi_{Csl}(f) \quad (3.27)$$

$$S_{N8}(f) = T_A^2(f) g_M^2 \gamma^2 \beta^2 (S_{N,Csl}(f) - \phi_{Csl}) + T_A^2(f) \beta \gamma \phi_{Csl} (g_M^2 + \sigma_M^2) \quad (3.28)$$

Only NPS is affected by the signal and noise transfer through the aliasing stage. The resulting noise after aliasing stage is given by,

$$S_{N9}(f) = S_{N8}(f) + \sum_{n=-\infty}^{\infty} S_{N8}\left(f - \frac{n}{a}\right) \quad (3.29)$$

During image readout, the electronic noise power, S_{Ne} is added to the total noise power. The signal and noise at the output of the tenth stage (electronic noise) are,

$$\phi_{10}(f) = \phi_8(f) \quad (3.30)$$

$$S_{N10}(f) = S_{N9}(f) + S_{Ne} \quad (3.31)$$

The input NPS is the number of x-rays incident on the detector is equal to the mean photon fluence, this is, $S_{N0} = \phi_0$ [92]. As a result, the term SNR_m^2 in (17) becomes ϕ_0 . Therefore $DQE(f)$ can be written as,

$$DQE(f) = \frac{\phi_{10}^2(f)}{\phi_o S_{N10}(f)} \quad (3.32)$$

3.4 Results and discussion

The shaded stages in 3.3 are excluded while evaluating the optical properties of CsI. This section is divided into three segments, namely, validation of the model, investigation of the inherent imaging performance of CsI, and effects of avalanche gain on the performance of a-Se based indirect x-ray detectors.

The simulations are conducted by assuming that the x-rays are generated with a Tungsten tube operated at 70 kVp and filtered with 21 mm aluminum, where the average photon energy is 54 keV. Therefore, the value of E is kept fixed at 54 keV for all the simulations. The density of CsI is 3.38 g/cm^3 [104]. The mass attenuation coefficients of CsI at x-ray energy is taken from [67]. It is assumed that the x-ray beam is restricted to within 0° from the central ray [112], and thus $T_G(f)=1$. The reflectivity parameters, ρ_1 and ρ_0 are 1 and 0, respectively [101]. The following K -fluorescence related parameters in CsI are used in the simulations [113]: $E_k = 30.37 \text{ keV}$, $\zeta = 0.83$, $\omega = 0.88$. The value of f_k is calculated using the method of Dance and Day [114]. The optical coupling efficiency (β_{op}) between CsI and a-Se is assumed to be ~ 0.8 [102].

Figures 3.4 (a), (b) and (c) show the $DQE(f)$ of 150, 300 and 600 μm thick CsI layers, respectively. The symbols represent experimental data which are extracted from [104]. The dashed lines are the theoretical fit to the experimental findings using the MTF due to the optical blurring (T_{OP}) measured by Zhao *et al.* [104]. They have calculated T_{OP} by dividing the experimental MTF by the MTF due to K -fluorescence reabsorption (T_K). The solid lines are the theoretical fit to the experimental results using the proposed cascaded linear-system model. The pixel size is 48 μm . The fitted values of κ and h_{CsI} are 40 and 5 mm^{-1} , respectively [101]. In the experimental results, the electronic noise is subtracted from the NPS measurements at different exposures and this makes the $DQE(f)$ exposure independent. For this reason, the electronic noise is assumed to be zero in the simulations. The nominal thicknesses of the CsI layer are 150, 300 and 600 μm . However, we have used the estimated thicknesses (calculated from mass loading) while performing the simulations. The estimated thicknesses are 169, 246 and 491 μm for corresponding nominal thicknesses of 150, 300 and 600 μm , respectively [104]. The intrinsic value of W_{\pm} for CsI

is ~ 17 eV. However, we used $W_{\pm} = 28$ eV in the simulations because only $\sim 60\%$ of the light emitted from CsI is transmitted towards the detector [104].

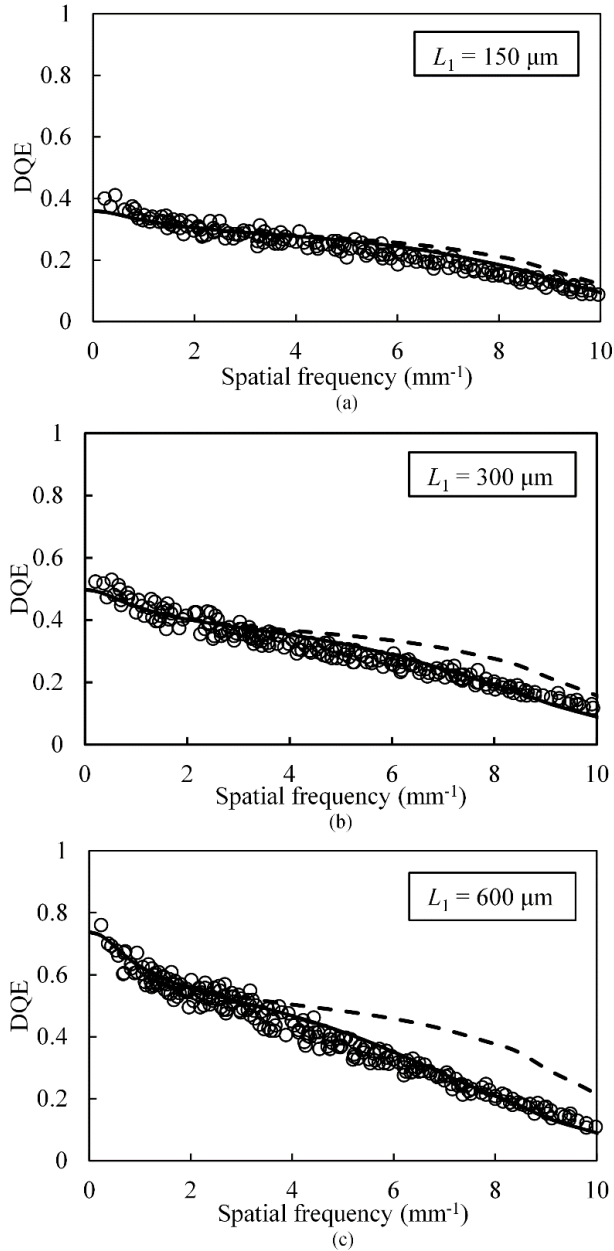


Figure 3.4 The DQE of CsI layer as a function of spatial frequency for different thicknesses of CsI samples, (a) $L_1=150 \mu\text{m}$, (b) $L_1=300 \mu\text{m}$, and (c) $L_1=600 \mu\text{m}$. The symbols, solid lines and dashed lines represent experimental results [104], T_{OP} with and without Lubberts effect, respectively.

The DQE(0), i.e., DQE($f=0$) increases from ~ 0.41 to ~ 0.77 (88% increment) when the thickness of CsI is increased from 150 to 600 μm . Whereas, at a higher frequency ($f = 6 \text{ mm}^{-1}$), DQE increases from ~ 0.22 to ~ 0.33 (50% increment). The increment in DQE is comparatively small at higher frequencies in thick scintillators. Because, at higher frequencies, the x-ray absorption in thicker CsI layer is overpowered by the frequency dependent stochastic and/or deterministic blurring processes. The thicker scintillator is more susceptible to blurring processes.

The presampling MTF of CsI samples of different thicknesses are shown in Figure 3.5. The MTF decreases with increasing the thickness of CsI because the optical photons have to travel a longer distance in thicker CsI layer.

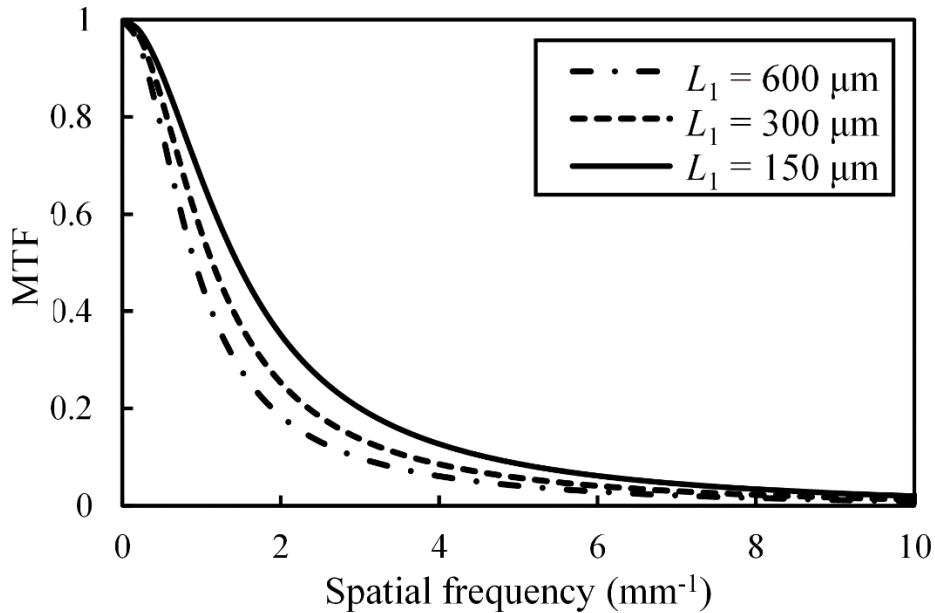


Figure 3.5 Presampling MTF of the CsI layers for different thicknesses.

In order to find the actual reason behind the drop in presampling MTF at higher frequencies in

thick CsI layer, we calculate the contribution of different blurring processes to the total presampling MTF as shown in Figure 3.6. The solid, dashed and dash-dotted lines represent the total presampling MTF, presampling MTF without K -fluorescence, and presampling MTF without optical blurring and Lubberts effects, respectively.

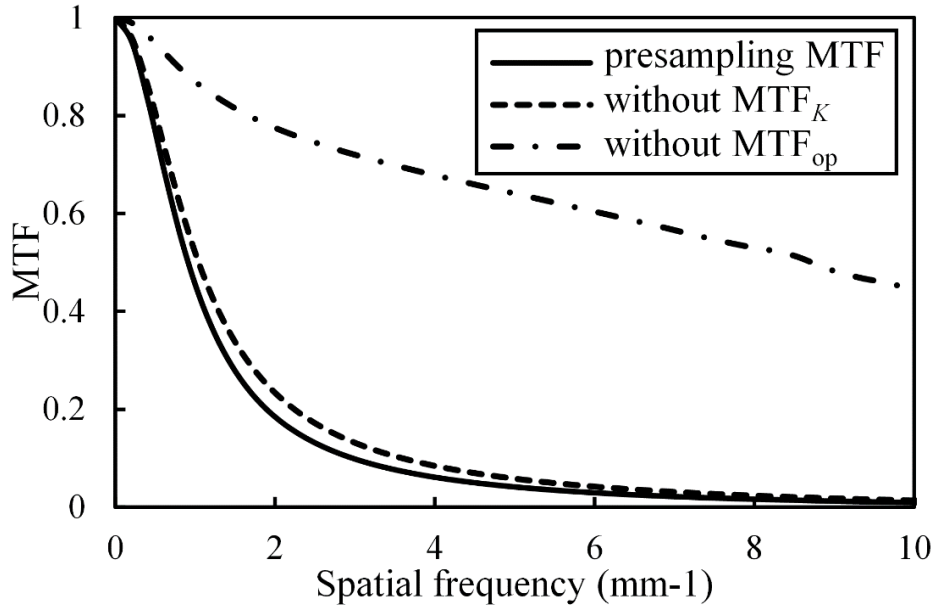


Figure 3.6 Presampling MTF (solid line), MTF without optical blurring with Lubberts effect (dash-dotted line) and MTF without K -fluorescence reabsorption scattering (dashed).

The results suggest that the MTF of CsI is more susceptible to the optical scattering with Lubberts effect than the K -fluorescence reabsorption blurring. In fact, the MTF at the Nyquist frequency (f_N) of 2.5 mm^{-1} improves from ~ 0.1 to ~ 0.75 when optical scattering is not considered. Whereas MTF increases from ~ 0.1 to ~ 0.17 when K -fluorescent reabsorption is not considered. Moreover, at f_N , the DQE decreases by $\sim 50\%$ due to the Lubberts effect alone (Figure 3.4 (c)).

The x-ray absorption can be improved by increasing the thickness of the CsI. High x-ray absorption

improves the signal strength. However at higher frequencies, after a certain thickness, the $DQE(f_N)$ saturates.

Figure 3.7 shows $DQE(f)$ at different electric fields. The solid and dashed lines represent DQE with and without Lubberts effect, respectively. The exposure is kept fixed at $1 \mu\text{R}$ and the pixel size is assumed to be $200 \times 200 \mu\text{m}$, which are the typical values for fluoroscopic applications [90]. The value of W_{\pm} for CsI is assumed to be $\sim 17 \text{ eV}$. The thickness of CsI is $600 \mu\text{m}$ and the electronic noise is 1000 e/pixel . The DQE at f_N (2.5 mm^{-1}) drops from 0.037 to 0.01 at a field of $60 \text{ V}/\mu\text{m}$ due to the Lubberts effect. The Lubberts fraction decreases with increasing the field thereafter. It is evident from the figure that an electric field of $103 \text{ V}/\mu\text{m}$ (corresponds to an avalanche gain of ~ 44 when L_2 is $15 \mu\text{m}$) is required to overcome the Lubberts effect.

Avalanche multiplication offers the gain which is required to overcome the adverse effects of electronic noise and thus makes the detector quantum noise limited. Figure 3.8 shows the $DQE(f)$ for a detector with CsI thickness of $600 \mu\text{m}$ at different avalanche gains. The pixel pitch is $200 \mu\text{m}$. The lower end of the dose range in fluoroscopy ($0.1 \mu\text{R}$ of x-ray exposure per frame) is considered. The wavelength of the optical photons emitted from the CsI layer is $\sim 530 \text{ nm}$ [104]. These photons are absorbed within $0.1 \mu\text{m}$ at the entrance side of the a-Se layer. Therefore, the depth dependent avalanche gain fluctuation noise is negligible.

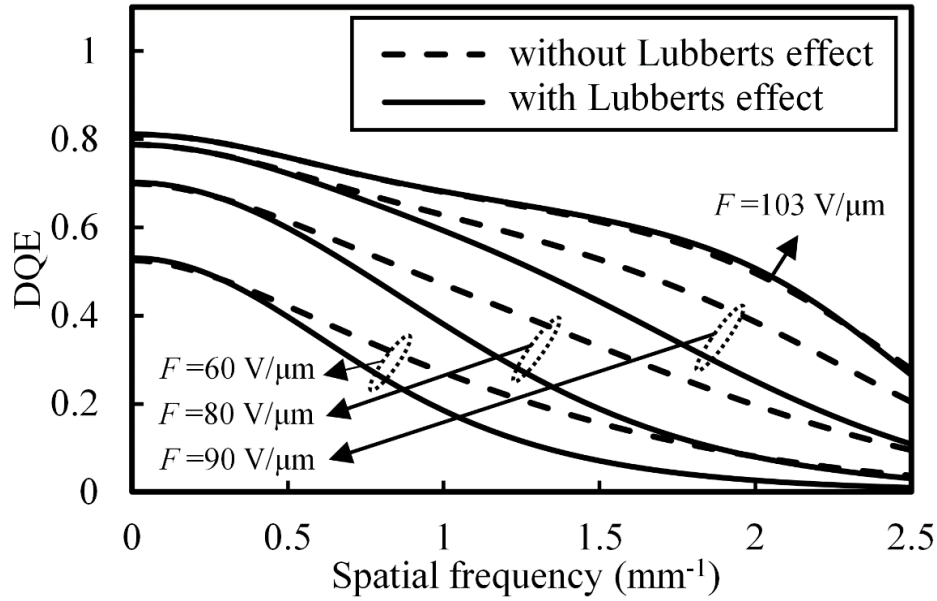


Figure 3.7 DQE(f) at different electric fields. The solid and dashed lines overlap at $F=103$ V/ μm .

It is observed that the improvement of DQE(f) without N_e beyond 70 V/ μm is not traceable. An avalanche gain of 45 (corresponds to the field of 110 and 103 V/ μm for L_2 of 8 and 15 μm , respectively) overcomes the adverse effect of the electronic noise of 1500 e/pixel whereas the required gain is 25 (electric field of 108 V/ μm for $L_2=8$ μm) to overcome the effect of the electronic noise of 700 e/pixel. The effect of N_e on DQE(0) is nullified at much smaller gain ($g_m = 5$ for $N_e = 700$ e/pixel). However, a high electric field across the a-Se layer is required to maintain a high quantum yield. A quantum yield of 0.2 and 0.36 are observed for the electric field of 70 and 110 V/ μm , respectively. From the results, we can conclude that avalanche gain improves the signal strength and overcomes the adverse effect of optical blurring with Lubberts effect and electronic noise.

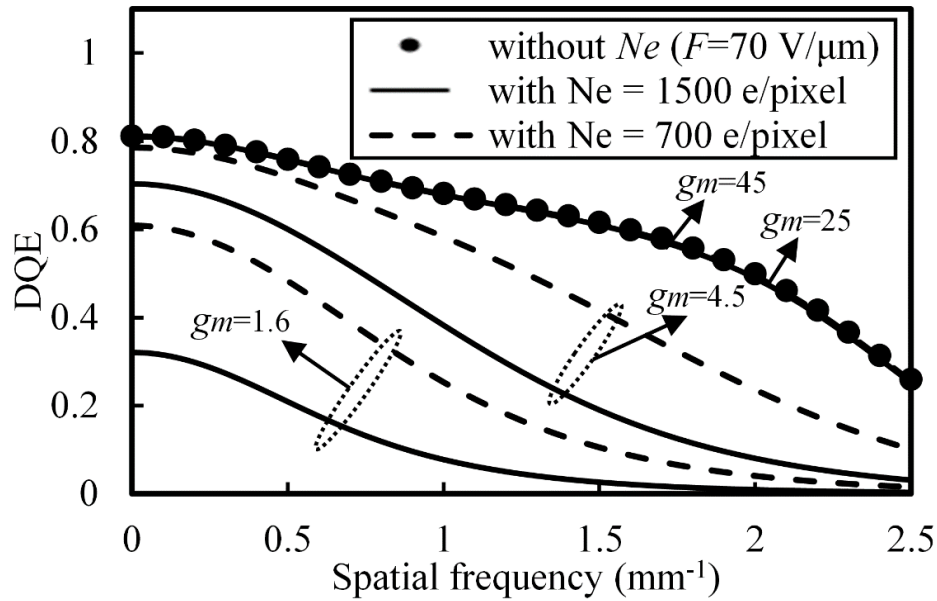


Figure 3.8 Calculated $DQE(f)$ at different avalanche gains. The solid ($g_m=45$) and dashed ($g_m=25$) lines overlap.

Figure 3.9 shows the effects of applied electric field (F) on $DQE(0)$ at different exposures. The $DQE(0)$ improves significantly with increasing exposure and it saturates at a field of ~ 103 V/ μm . The avalanche gain is more important at low exposure and/or higher electronic noise. It is evident from figures (3.8) & (3.9) that, although a higher field (below avalanche threshold) may make the detector quantum noise limited at zero spatial frequency, avalanche gain is required for all spatial frequencies of importance (up to f_N).

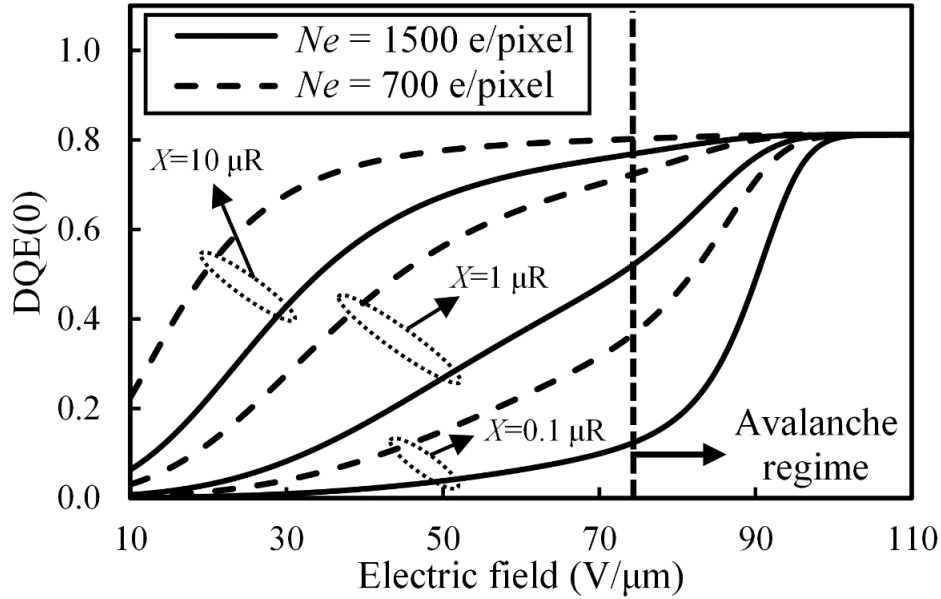


Figure 3.9 DQE(0) as a function of applied electric field for different fluoroscopic exposures. The detector thickness is 15 μm .

3.5 Summary

A cascaded linear-system model including optical blurring with Lubberts effect and K -fluorescence reabsorption is developed for a-Se based indirect conversion avalanche x-ray detector in this paper. At high frequencies, the Lubberts effect in optical blurring mainly reduces the DQE of the detector. The thick detectors are more susceptible to the adverse effects of K -fluorescence reabsorption and Lubberts effect. The DQE at f_N (2.5 mm^{-1}) drops from 0.037 to 0.01 at a field of $60 \text{ V}/\mu\text{m}$ (below avalanche) due to the Lubberts effect. The Lubberts fraction decreases with increasing the field thereafter. An avalanche gain of 45 and 25 are sufficient to overcome the Lubberts effect together with the effect of electronic noise of 1500 and 700 electrons per pixel, respectively, and the detector performance will be quantum noise limited. The analysis of this

paper offers more physical insight for the explanation of the experimental results, and therefore, helps to optimize the design for improving the performance of the CsI based a-Se avalanche x-ray detectors.

CHAPTER 4

Impact of charge carrier trapping on amorphous selenium direct conversion avalanche x-ray detectors

The contribution of this chapter has recently been published [115]. Most of the materials are taken from the published manuscript.*

A cascaded linear-system model is proposed for direct conversion multilayer avalanche x-ray detectors. The structure uses a mesh electrode to separate the absorption and gain regions to eliminate the absorption depth dependent avalanche gain variation. The proposed model considers charge collection efficiency using the Ramo-Shockley theorem and the weighting potential of the individual pixel. A 2D simulation is performed to calculate the actual weighting potential in the absorption layer. The loss of resolution due to the trapped charges in the absorption layer is also calculated. The model incorporates blurring due to *K*-fluorescent x-ray absorption. The optimal design parameters and operational condition for a-Se based direct-conversion multilayer avalanche x-ray detectors are described in this work. The required avalanche gain to overcome the electronic noise is calculated. The model offers more physical insight of the performance, and therefore, helps to optimize the design of a-Se based direct-conversion avalanche x-ray detectors.

* S. M. Arnab and M. Z. Kabir, "Impact of charge carrier trapping on amorphous selenium direct conversion avalanche x-ray detectors," *Journal of Applied Physics*, vol. 122, pp. 134502, 2017

4.1 Introduction

The flat-panel detector (FPD) with an active matrix array are the most widely used digital x-ray detectors for many radiographic applications and further research is underway to achieve adequate image quality for fluoroscopy and portal imaging [6], [116]. The image quality of a FPD largely depends on its x-ray sensitivity. The sensitivity, on the other hand, depends on the detector thickness, operating conditions and photoconductor properties [117]. Amorphous selenium (a-Se) is currently the best choice of photoconductor for direct-conversion detectors (i.e., the x-ray photons directly create electron-hole pair, EHP in the a-Se layer) due to its good charge transport properties and low dark current. The main drawback of the a-Se detector is low x-ray conversion gain [91]. This problem becomes more severe at low x-ray exposure (e.g., x-ray exposure used in fluoroscopy) because of electronic noise which arises from the active matrix arrays (AMA) [118].

Besides the electronic noise, charge carrier trapping in the absorption layer also has adverse effects on the performance of the direct-conversion x-ray detector. The incomplete charge collection due to carrier trapping degrades the signal strength [119]. They also induce charges on the neighboring pixels which increases the lateral spreading of the signal [120].

The most feasible way to address these problems is to increase the signal strength. The avalanche multiplication of charge carriers increases the internal gain of the photoconductor [118]. However, the statistical nature of x-ray absorption causes avalanche gain variation which increases the total noise of the system. A separation between the x-ray absorption and avalanche gain regions eliminates the avalanche gain variation [121].

Lee *et al.* [122] have recently proposed a direct-conversion avalanche x-ray detector structure which uses the concept of the MICROMEGAS structure [123]. The proposed structure contains distinct absorption and gain regions. A solid-state amorphous semiconductor material (i.e., a-Se) is used as the photoconductor. A ten-fold signal amplification has been obtained without introducing excessive noise (i.e., avalanche gain variation). Wronski *et al.* [124] have done further modification to this structure by increasing the mesh electrode aperture and aligning them (mesh apertures) with the pixel electrodes. The cascaded linear system model that has been developed by Wronski *et al.* to determine the detective quantum efficiency (DQE) of their proposed direct-conversion multiplayer avalanche x-ray detector does not include the charge collection efficiency, and modulation transfer function (MTF) due to carrier trapping. Therefore, their proposed model may not predict the expected detector behavior.

Many of the previous studies used the well-known Hecht relation to calculate the charge collection efficiency of a photoconductor [73][91]. However, the Hecht relation is applicable if the weighting potential across the photoconductor is linear, which is not the case in the direct-conversion multiplayer avalanche x-ray detector.

4.2 Structure of direct-conversion multilayer avalanche x-ray detector with grid electrode

Figure 4.1 shows the cross section of an a-Se based direct-conversion multilayer avalanche detector with grid electrode. It consists of a thick ($L_1 \sim 1000 \mu\text{m}$) absorption layer followed by a

comparatively thin ($L_2 \sim 50 \mu\text{m}$) avalanche gain region [124]. The absorption and gain regions are separated by a mesh electrode. The pixel pitch is $100 \mu\text{m}$ and the mesh aperture (A_{mesh}) is half of the pixel pitch [124]. The pixel electrodes are aligned with the mesh apertures. The x-rays are absorbed and converted into electron and hole pairs (EHPs) in the absorption layer under an electric field (F_1) of $\sim 10 \text{ V}/\mu\text{m}$ [91]. The detector is biased in such a way that the holes travel towards the mesh electrode. The mesh electrode sets up a high electric field, F_2 ($\sim 70\text{-}110 \text{ V}/\mu\text{m}$) within the gain region to initiate the avalanche multiplication of x-ray generated holes [88]. Therefore, the holes undergo avalanche multiplication in the gain region while travelling towards the pixel electrodes and are stored in the pixel capacitors. The capacitors are then readout periodically by TFT or CMOS array. Blocking nature of the electrodes prevents the electron injection in the gain region thus reduces the dark current [125].

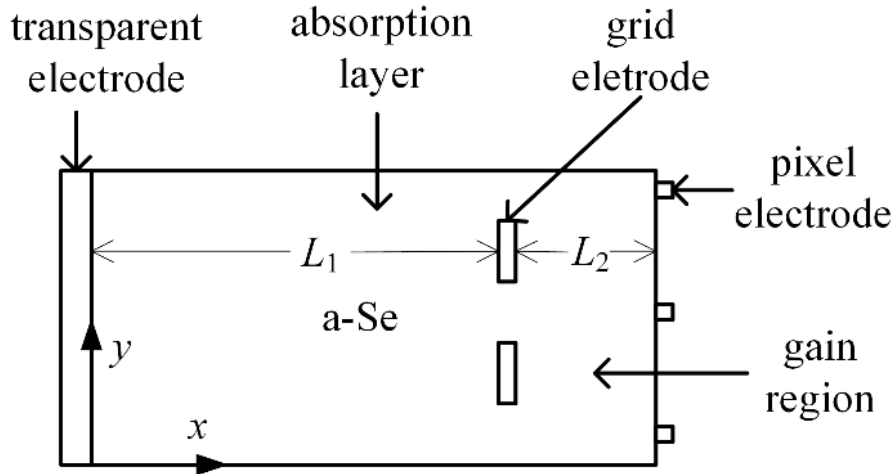


Figure 4.1 Cross sectional diagram showing an a-Se based direct-conversion multiplayer avalanche x-ray detector. The detailed diagram can be found in Ref. [124].

4.3 Theory

The average energy of the x-ray spectrum can be used to determine the effect of the total spectrum on the detector. Therefore, we consider mono-energetic x-ray with energy, E is impinging on the photoconductor. The probability density for an x-ray photon to be absorbed at a distance x_1 from the top surface (radiation receiving surface) is given by [88]

$$P_{x_1}(E, x_1) = \begin{cases} \frac{\alpha e^{-\alpha x_1}}{\eta}, & 0 \leq x_1 \leq L_1 \\ 0, & elsewhere \end{cases} \quad (4.1)$$

where $\eta = 1 - \exp(-\alpha L_1)$ is the quantum efficiency and α is the linear attenuation coefficient of the photoconductor.

4.3.1 Signal and noise propagation

Figure 4.2 represents the imaging processes involved in the direct-conversion multilayer avalanche x-ray detector. Each process in the linear cascaded system model may refer to one of the following processes [91] 1. stochastic gain; 2. stochastic blurring; 3. deterministic blurring; 4. aliasing; and 5. addition.

4.3.1.1 Stochastic gain

The signal and noise at the output of the i^{th} stochastic gain stage, which is characterized by the

mean gain, g_i and variance, $\sigma_{g_i}^2$ are given by the following equations [91]

$$\phi_i(E, x) = g_i(E, x)\phi_{i-1}(E, x) \quad (4.2)$$

$$S_{N_i}(E, x, f) = g_i^2(E, x)S_{N(i-1)}(E, x, f) + \sigma_{g_i}^2(E, x)\phi_{i-1}(E, x) \quad (4.3)$$

where $\phi_{i-1}(E, x)$ and $S_{N(i-1)}(E, x)$ are the mean number of input quanta and the NPS of the i^{th} stage, respectively. The selection, conversion gain, charge collection and avalanche gain stages in Figure 4.2 are considered to be the stochastic gain stages.

4.3.1.2 Stochastic blurring

The output of i^{th} stochastic blurring stage is given by the following equations [91]

$$\phi_i(E, x, f) = T_i(E, x, f)\phi_{i-1}(E, x, f) \quad (4.4)$$

$$S_{N_i}(E, x, f) = T_i^2(E, x, f)S_{N(i-1)}(E, x, f) + [1 - T_i^2(E, x, f)]\phi_{i-1}(E, x) \quad (4.5)$$

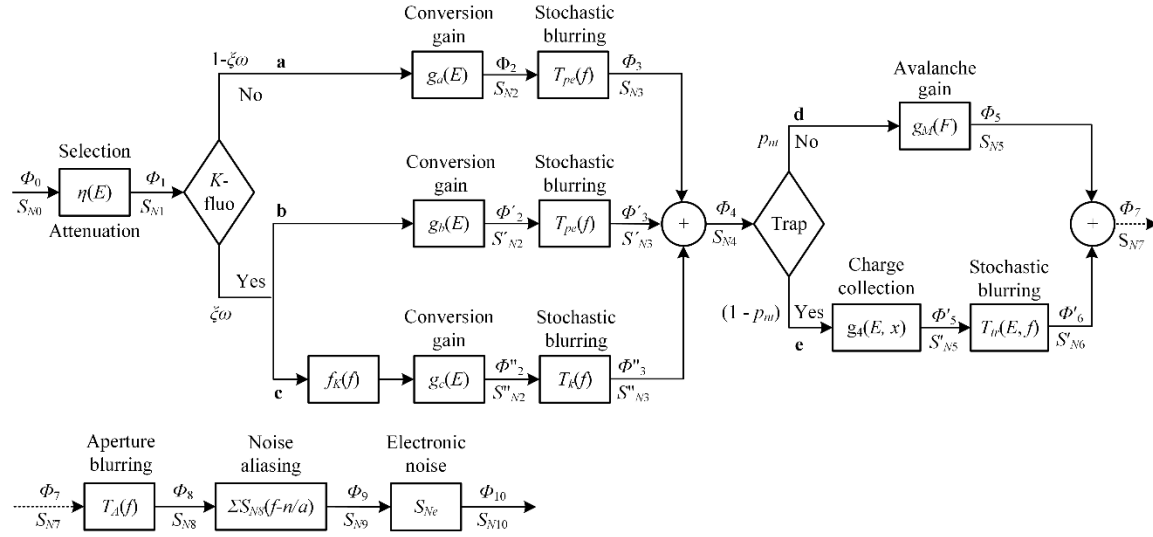


Figure 4.2 Diagram showing the flow of signal and NPS in the cascaded linear system model proposed for direct-conversion multiplayer avalanche x-ray detector. Here ζ is the probability of K -shell interaction, ω is the probability of K -fluorescence production and f_k is the average reabsorption probability of K -fluorescent x-ray photons within the photoconductor volume.

where $T_i(E, x; f)$ is the MTF of the i^{th} stochastic blurring stage. Blurring due to K -fluorescence reabsorption, range of the photoelectrons and charge carrier trapping are considered to be stochastic blurring.

4.3.1.3 Deterministic blurring

The transfer relationship through the i^{th} deterministic blurring stage is characterized by the following equations [91]

$$\phi_i(E, x; f) = T_i(E, x; f) \phi_{i-1}(E, x; f) \quad (4.6)$$

$$S_{Ni}(E, x; f) = T_i^2(E, x; f) S_{N(i-1)}(E, x; f) \quad (4.7)$$

The deterministic blurring is a result of averaging the signal over a pixel area. The following equation shows the blurring caused by the aperture with dimension $a \times a$,

$$T_A(f) = |\sin c(af)| = \left| \frac{\sin(\pi af)}{\pi af} \right| \quad (4.8)$$

4.3.1.4 Aliasing

The deterministic blurring is a result of averaging the signal over a pixel area. The digital detector is under-sampled because the pre-sampling signal has frequency components above the Nyquist frequency (f_N). The aliasing of NPS occurs due to under-sampling in digital detectors. The aliased NPS is given by [91]

$$S_{Ni}(f) = S_{N(i-1)}(f) + \sum_{n=-\infty}^{\infty} S_{N(i-1)}\left(f - \frac{n}{a}\right) \quad (4.9)$$

where i^{th} stage is assumed to be the noise aliasing stage.

4.3.1.5 Addition

The electronic noise generated from each pixel is independent of others. Therefore, the electronic noise power is added to the total noise power and the signal remains the same [91]

4.3.2 Mathematical models for stages

The mathematical models describing various stages are given below.

4.3.2.1 X-Ray photon attenuation (Selection)

An x-ray photon interaction with the photoconductor is a Bernoulli random process. According to binomial theorem, the variance of η can be given by, $\sigma_{\eta}^2(E) = \eta(1-\eta)$.

4.3.2.2 Conversion gain

The average number of EHP generation due to the absorption of an incident x-ray photon is referred to the mean conversion gain. Following a successful absorption of an x-ray photon, the signal and NPS are characterized using three parallel chains, namely a, b and c (see Figure 4.2). The details of the parallel paths are: Path a: Conversion of incident photon into EHPs with no K -fluorescence generation; path b: Conversion of incident photon into EHPs along with K -fluorescence generation but no reabsorption of characteristic x-rays; and path c: Conversion of incident photon into EHPs with K -fluorescence generation and reabsorption at a different location than the primary x-ray interaction site.

The conversion gain of the three parallel paths a , b and c are, respectively [91]

$$g_a(E) = \frac{E}{W_{\pm}}, g_b(E) = \frac{(E - E_K)}{W_{\pm}}, \text{ and } g_c(E) = \frac{E_K}{W_{\pm}}, \quad (4.10)$$

where g is the conversion gain, E_K is the average energy of K -fluorescence photons and W_{\pm} is the EHP creation energy of the photodetector.

The conversion gain is a random process. The variation in the conversation gain is $\sigma_g^2(E) = g(E)$

when it is assumed that the number of EHP generated by the x-ray photon follows the Poisson distribution [92]

4.3.2.3 Blurring due to range of primary photoelectron

The highly energized primary photoelectrons collide randomly with atoms and create a large number of secondary photoelectrons. The size of the electron cloud determines the blurring caused by this process and is closely related to the range of the primary photoelectron, R_{max} (i.e., how far the photoelectron can travel). The value of R_{max} , when the x-ray energy lies between 10-1000 keV, is calculated by the following empirical expression [126]

$$R_{max} = 2.761 \times 10^{-5} \times \frac{M_{atom} E_0^{5/3}}{\rho Z^{8/9}} \quad (4.11)$$

where ρ is the density (g/cm³), M_{atom} is the atomic mass (g/mol), Z is the atomic number, E_0 is the energy (keV) of the primary photoelectron and resultant R_{max} is in mm.

It is assumed that the charge carriers created by the photoelectrons have a spherically symmetric distribution with a Gaussian profile $\exp(-R^2/\sigma^2)$, where R is the radial distance and the parameter σ has a linear relationship with R_{max} . Que and Rowlands [112] have estimated σ to be $R_{max}/2$ for a-Se. The MTF due to the range of the primary photoelectron is calculated by taking the 2-D Fourier transform of the PSF obtained by projecting the charge distribution onto the lateral plane and is given by [112]

$$T_{pe}(E, f) = e^{-\pi^2 \sigma^2 f^2} \quad (4.12)$$

4.3.2.4 Blurring due to K -fluorescence reabsorption

It is probable that one or more characteristic x-rays known as K -fluorescent x-rays are emitted if the incident x-ray energy is above the K -shell energy of a-Se. The reabsorption of the emitted K -fluorescent x-rays at a different location than the primary photon interaction site causes a lateral signal spreading. The model developed by Kabir *et al.* [91] to calculate the MTF due to K -fluorescence reabsorption have been used in the cascaded linear system model.

4.3.2.5 Charge collection in the absorption layer

The Shockley-Ramo theorem provides a direct and simple method to compute the induced charge at different pixels [78]. According to the theorem, the induced charge on an electrode due to the motion of a charge carrier is the difference between the weighting potentials at the point of the charge carrier and its origin [127]. The weighting potential, V_w can be calculated by solving the Laplace equation $\nabla^2 V_w = 0$, using the boundary conditions; $V_w = 1$ on the pixel electrode and $V_w = 0$ on all the other electrodes [128]. The Laplace equation has been solved using Finite Difference Method (FDM). The average weighting potential across the pixel length is used to compute the charge collection in the absorption layer.

The trapping of charge carrier is a random process. Assuming that the x-ray is absorbed at x_1 , the probability density functions of the electrons travelling towards the top electrode being trapped at x'_1 and the holes travelling towards the mesh electrode being trapped at x''_1 are given by the following equations, respectively [119]

$$P_{top}(x_1'|x_1) = \alpha' e^{-\alpha'(x_1-x_1')} \quad (4.13)$$

$$P_{grid}(x_1''|x_1) = \beta' e^{-\beta'(x_1''-x_1)} \quad (4.14)$$

where α' and β' are the linear trapping attenuation coefficients of charge carriers travelling towards top and mesh electrode, respectively. We assume that the electrons are moving towards the top electrode and the holes are moving towards the mesh electrode. Therefore, the linear trapping attenuation coefficients are given by [119]

$$\alpha' = 1/\mu_e \tau_e F_1 \quad (4.15)$$

$$\beta' = 1/\mu_h \tau_h F_1 \quad (4.16)$$

where μ and τ are the carrier mobility and lifetime, respectively and F_1 is the electric field exists in the absorption layer. The subscripts e and h stand for electron and hole, respectively. The drifting electron and hole in the absorption layer (i.e., a-Se) produce current of similar polarity at any electrode. Therefore, the charge collection at the pixel electrodes is governed by both types of carrier. The collected charge at a pixel for an EHP generation at x_1 , due to the charge carriers that are travelling towards the mesh electrode is given by

$$Q_{grid}(x_1) = \sum_{m=x_1+1}^{N_{sp}-1} [V_w(x_1) - V_w(m)] \left[e^{-\beta'(m-x_1)} - e^{-\beta'((m+1)-x_1)} \right] + e^{-\beta'(L_1-x_1)} [V_w(N) - V_w(x_1)] \quad (4.17)$$

and due to the charge carriers, that are travelling towards the top electrode is given by

$$Q_{top}(x_1) = \sum_{m=1}^{x_1-1} [V_w(x_1) - V_w(m)] \left[e^{-\alpha'(x_1-(m+1))} - e^{-\alpha'(x_1-m)} \right] + e^{-\alpha'x_1} V_w(x_1) \quad (4.18)$$

where $\Delta x_1 = L_1/N_{sp}$ is the uniform step size and N_{sp} is the number of spatial divisions. Then the discrete point $x_1 = x_i \Delta x_1$, where x_i is an integer varies from 1 to N_{sp} . The weighting potential is considered to be constant within each step. The total collected charge at the pixel electrode due to an EHP generation at x_1 is

$$g_4(x_1) = Q_{grid}(x_1) + Q_{top}(x_1) \quad (4.19)$$

The variation of charge collection due to the random trapping is

$$\begin{aligned} \sigma_{g_4}^2(x_1) = & \sum_{m=x_1+1}^{N_{sp}-1} [V_w(x_1) - V_w(m)]^2 [e^{-\beta'(m-x_1)} - e^{-\beta'((m+1)-x_1)}] \\ & + e^{-\beta'(L_1-x_1)} [V_w(m) - V_w(x_1)]^2 + Q_{grid}^2(x_1) \\ & + \sum_{m=1}^{x_1-1} [V_w(x_1) - V_w(m)]^2 [e^{-\alpha'(x_1-(m+1))} - e^{-\alpha'(x_1-m)}] + e^{-\alpha'x_1} V_w^2(x_1) + Q_{top}^2(x_1) \end{aligned} \quad (4.20)$$

4.3.2.6 Probability of holes reaching gain region

The holes that are being trapped within the absorption layer do not participate in the avalanche multiplication process. However, the trapped charge carriers contribute to the induced charge density. The induced charge is not a subject to avalanche multiplication. Only the holes that arrive at the mesh electrode participate in avalanche multiplication. The probability of a hole reaching to the mesh electrode when the X-ray photon is absorbed at x_1 is calculated as follows

$$p_{nt}(x_1) = 1 - \int_{x_1}^{L_1} \beta' e^{-\beta'(L_1-x_1)} dx_1 = e^{-\beta'(L_1-x_1)} \quad (4.21)$$

For exponential x-ray absorption, the mean value of $p_{nt}(x_1)$ is

$$P_{nt} = \int_0^{L_1} \frac{\alpha e^{-\alpha x_1}}{\eta} e^{-\beta'(L_1-x_1)} dx_1 = \frac{\alpha}{\eta} \left[\frac{e^{-\alpha L_1} - e^{-\beta' L_1}}{\beta' - \alpha} \right] \quad (4.22)$$

4.3.2.7 Blurring due to charge trapping

The charge carrier trapping in a particular pixel reduces the charge collection at that pixel. Simultaneously trapped carriers induce charges on the neighboring pixel electrodes which causes image blurring. Kabir *et al.* [120] have proposed an analytical model to calculate the MTF, $T_{tr}(E, f)$ due to distributed carrier trapping in the bulk of a photoconductor. Their MTF model for charge carrier trapping is used in the cascaded linear system model.

4.3.2.8 Avalanche gain

The avalanche multiplication of charge carriers increases the signal gain. The following empirical equation is used to characterize the avalanche gain (g_M) under the assumption that the contribution of electron is negligible and only holes contribute to impact ionization [48][118][129][130]

$$g_M = e^{\beta L_2} \quad (4.23)$$

where L_2 is the thickness of the gain region (region between mesh electrode and pixel electrode),

The variance in avalanche gain is [118]

$$\sigma_M^2 = g_M^2 - g_M \quad (4.24)$$

4.3.3 Detective Quantum Efficiency (DQE)

In the calculation, it is assumed that the absorption layer is distinct from gain layer. The mesh electrode is sandwiched between these two layers. Applying Eq.(2)–Eq.(7) successively, the expected signal and NPS at the output of the second stage in path a are

$$\phi_3(f) = \eta(1 - \xi\omega)\phi_0 g_a T_{pe}(f) \quad (4.25)$$

$$S_{N3}(f) = \eta(1 - \xi\omega)\phi_0 g_a [T_{pe}^2(f) g_a + 1] \quad (4.26)$$

Similarly, the expected signal and NPS at the output of the second stage in path b are

$$\phi_3'(f) = \eta\xi\omega\phi_0 g_b T_{pe}(f) \quad (4.27)$$

$$S'_{N3}(f) = \eta\xi\omega\phi_0 g_b [T_{pe}^2(f) g_b + 1] \quad (4.28)$$

In the same way, the outputs of the third stage in path c are

$$\phi_3''(f) = \eta\xi\omega\phi_0 g_c T_k(f) f_k \quad (4.29)$$

$$S''_{N3}(f) = \eta\xi\omega f_k \phi_0 g_c [T_k^2(f) g_c + 1] \quad (4.30)$$

The total signal and NPS at the mesh electrode (before entering the gain region) are

$$\phi_4(f) = \phi_3(f) + \phi_3'(f) + \phi_3''(f) \quad (4.31)$$

$$S_{N3}(f) = S_{N3}(f) + S'_{N3}(f) + S''_{N3}(f) + 2S_{bc}(f) \quad (4.32)$$

where S_{bc} is the cross correlation between path b and c and given by the following equation [107]

$$S_{bc}(f) = \eta \xi \omega f_k \phi_0 g_b g_c T_{pe}(f) T_k(f) \quad (4.33)$$

After summing the signal and NPS from path d and e , the resultant $\phi_7(f)$ and $S_{N7}(f)$ are

$$\phi_7(f) = \phi_4(f) [g_M p_{nt} + T_{tr}(f) g_4 (1 - p_{nt})] \quad (4.34)$$

$$S_{N7}(f) = (1 - p_{nt}) [T_{tr}^2 \{g_4^2 S_{N4}(f) + \sigma_{g_4}^2 \phi_4 - g_4 \phi_4\} + g_4 \phi_4] \quad (4.35)$$

After aperture blurring, the signal and NPS becomes,

$$\phi_8(f) = T_A(f) \phi_7(f) \quad (4.36)$$

$$S_{N8}(f) = T_A^2(f) S_{N7}(f) \quad (4.37)$$

The resulting noise after aliasing stage is given by,

$$S_{N9}(f) = S_{N8}(f) + \sum_{n=-\infty}^{\infty} S_{N8}(f - \frac{n}{a}) \quad (4.38)$$

During image readout, the electronic noise power, S_{Ne} is added to the total noise power. The signal and noise at the output of the tenth stage (electronic noise) are,

$$\phi_{10}(f) = \phi_8(f) \quad (4.39)$$

$$S_{N10}(f) = S_{N9}(f) + S_{Ne} \quad (4.40)$$

The input NPS is the number of x-rays incident on the detector is equal to the mean photon fluence

(ϕ_0) , this is, $S_{n0} = \phi_0$. As a result, the frequency dependent $DQE(f)$, which is the ratio between the squares of the signal-to-noise ratios (SNR) at the input and output, can be written as,

$$DQE(f) = \frac{\phi_{i0}^2(f)}{\phi_o S_{N10}(f)} \quad (4.41)$$

4.4 Results and Discussion

The actual weighting potential does not remain zero in the absorption layer mainly due to finite mesh area [128]. Figure 4.3 shows a 2D representation of the actual weighting potential in the detector, where the pixel area, A is $100 \mu\text{m} \times 100 \mu\text{m}$. The A_{mesh} is $50 \mu\text{m}$ and the thicknesses of the absorption and gain regions are $1000 \mu\text{m}$ and $50 \mu\text{m}$, respectively. It is observed that the weighting potential becomes as high as 0.3 in the middle of the aperture.

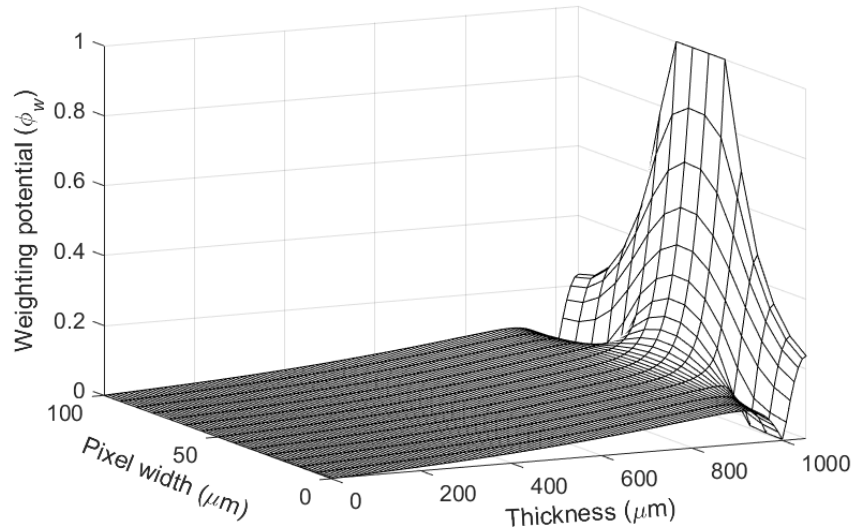


Figure 4.3 Weighting potential of a direct-conversion multilayer avalanche x-ray detector. The charge induction is the greatest in the region near the pixel electrode.

Figure 4.4 shows the effect of A_{mesh} on the average weighting potential in the absorption layer. The average weighting potential increases when the A_{mesh} is increased. In the vicinity of the mesh electrode, the average weighting potential increases from ~ 0.12 to ~ 0.21 if the aperture increases from $50 \mu\text{m}$ to $70 \mu\text{m}$. The average weighting potential is used to determine the charge collection at the pixel electrode due to the movement of charge carriers.

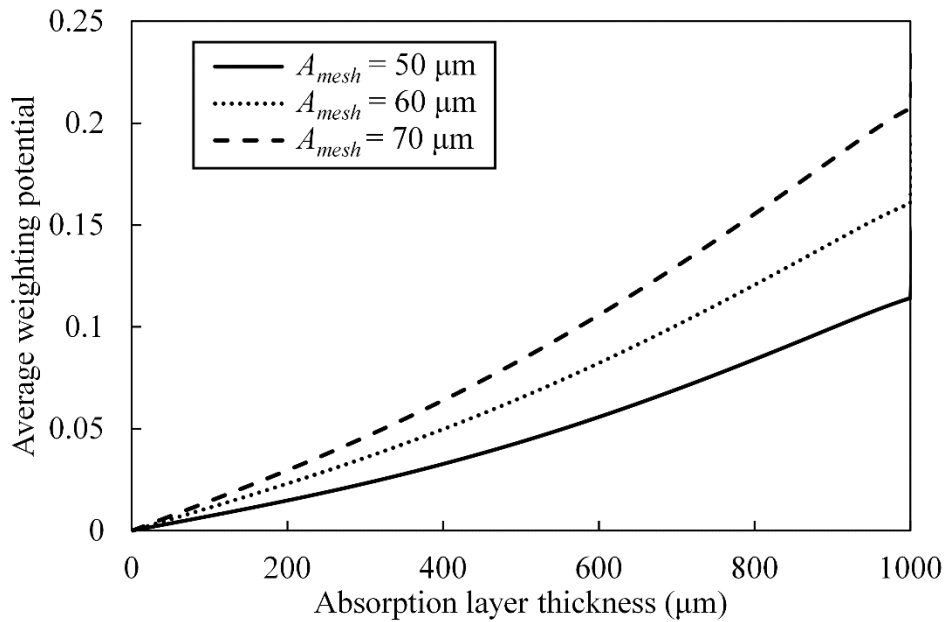


Figure 4.4 Average weighting potential in the absorption layer for different mesh aperture.

In Figure 4.5, the $DQE(f)$ calculated using Wronski et al.'s [124] model (without K -fluorescence reabsorption and carrier trapping, and zero weighting potential in the absorption layer) is compared with the $DQE(f)$ obtained by using the present model for different avalanche gains. The simulations are performed for fluoroscopic (70 kVp with 23.5 mm total Al filtration, where the average photon energy is $\sim 52 \text{ keV}$) applications [91]. Therefore, the value of E is kept fixed at 52 keV for the simulations. The values of the parameters used in the simulation are given in Table 4.1. In

fluoroscopic application, the x-ray exposure (X) varies from 0.1 to 10 μR . The conversion gain is calculated using Equation 4.10 and η is calculated using the linear attenuation coefficient of a-Se (which is taken from Ref. [67]). The value of f_k is calculated using the method of Dance and Day [114]. The value of F_1 is 10 $\text{V}/\mu\text{m}$. The thicknesses of the absorption and the gain regions is assumed to be 1000 and 50 μm , respectively [124]. The electronic noise is 1500 e/pixel [88][124]. Carrier trapping in the gain region is neglected because the number of carriers trapped in the gain region is negligible compare to that in absorption layer. It is because the thickness of the gain region is much less compared to the thickness of the absorption layer and also the electric field in the gain region is much higher than that in the absorption layer. Therefore, for simplicity, we have considered carrier trapping only in the absorption layer.

Table 4.1 Parameters used in the simulations

Parameters	Values
pixel pitch, Ref. [124]	100 μm
K -fluorescent X-ray energy (E_k), Ref. [91]	12.7 keV
probability of K -shell interaction (ξ), Ref. [91]	0.864
Probability of K -fluorescence production (ω), Ref. [91]	0.596
EHP creation energy (W_{\pm}), Ref. [72]	40 eV
electron mobility (μ_e), Ref. [91] and [73]	0.003 $\text{cm}^2/\text{V-s}$
electron lifetime (τ_e), Ref. [91] and [73]	200 μs
hole mobility (μ_h), Ref. [91] and [73]	0.12 $\text{cm}^2/\text{V-s}$
hole lifetime (τ_h), Ref. [73]	30 μs

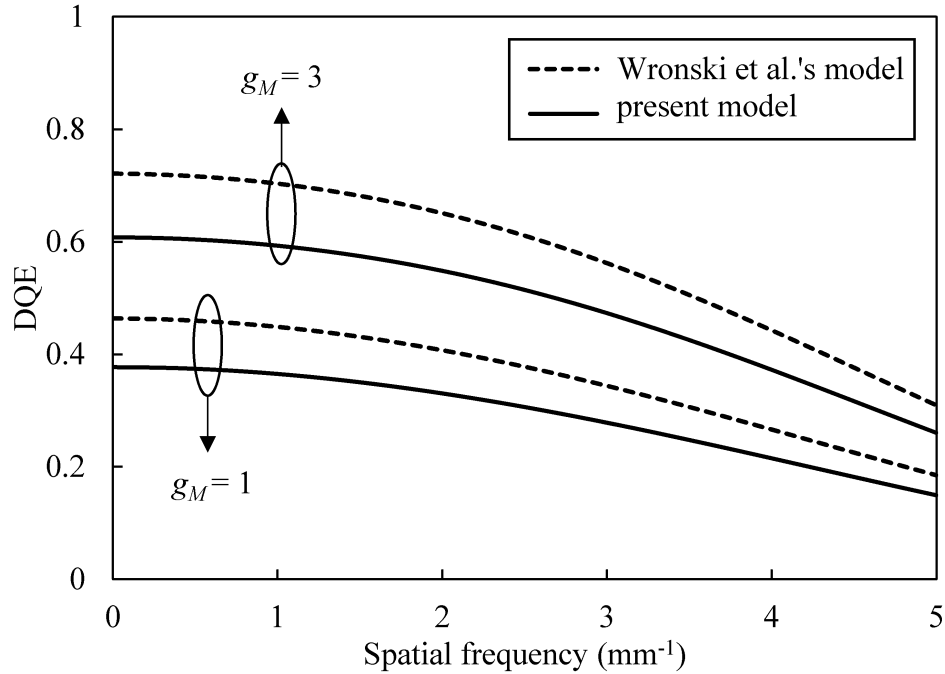


Figure 4.5 Comparison between Wronski et al.'s [124] model and the proposed model for different avalanche gains. The x-ray exposure is 1 μ R.

It is evident from Figure 4.5 that charge carrier trapping and non-zero weighting potential in the absorption layer have a significant effect on the $DQE(f)$ performance of the detector. Therefore, considering the charge collection efficiency and blurring due to carrier trapping in the absorption layer is very important to determine the actual characteristics of the direct-conversion multilayer avalanche detector.

The x-ray photons are absorbed exponentially. Therefore, the x-ray generated electrons do not travel a long distance before being collected by the top electrode as compared to the generated holes that travel to the mesh electrodes. Thus, the electron transport properties have a minimal effect on the $DQE(f)$ performance of the detector. The trapped holes contribute a fraction of the total charge collection due to a non-zero weighting potential in the absorption layer. Figure 4.6

shows the effect of carrier trapping in absence of avalanche gain ($g_M = 1$). It shows that the hole lifetime has to be in the order of $\sim 100 \mu\text{s}$ or more to neglect the trapping effect.

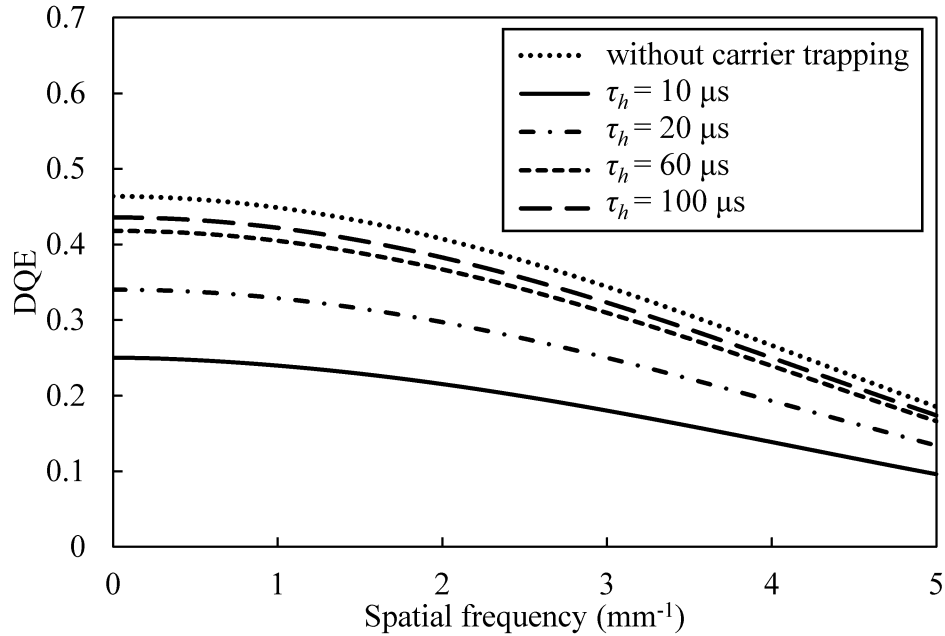


Figure 4.6 Effect of hole lifetime on $DQE(f)$ when $N_e = 1500 \text{ e/pixel}$. The dotted line represents the $DQE(f)$ without carrier trapping.

Non-zero weighting potential in the absorption layer has a significant effect on the $DQE(f)$ performance of the x-ray detector. Figure 4.7 shows the effect of actual weighting potential in the absorption layer on the $DQE(f)$ using the proposed cascaded linear system model (Figure 4.2). The values of all parameters are the same as mentioned earlier.

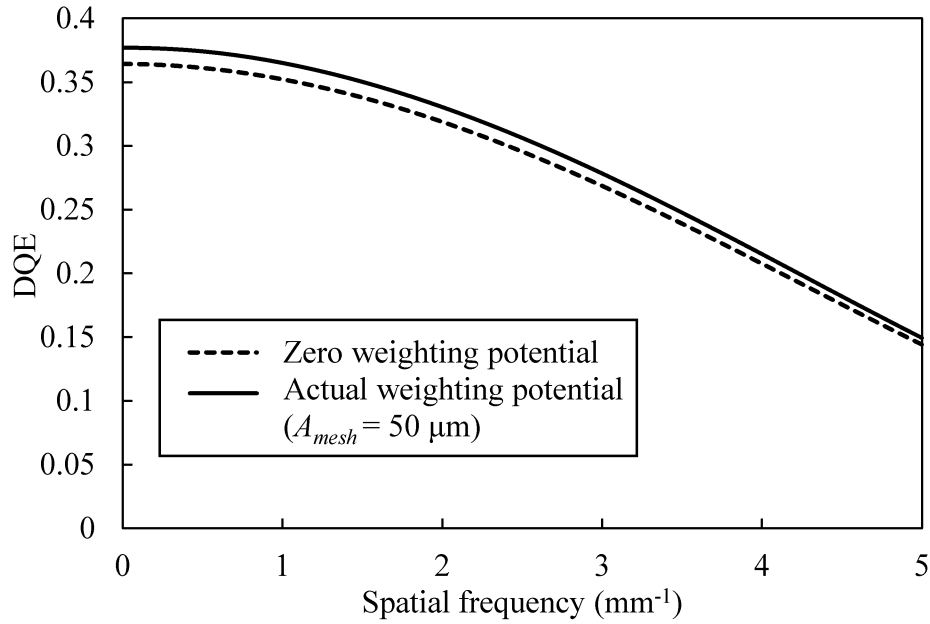


Figure 4.7 Effect of non-zero weighting potential in the absorption layer on the $DQE(f)$ at $X = 1 \mu R$ and the value of g_M is set to 1.

In Figure 4.7, the solid and dashed lines show the $DQE(f)$ in presence of actual weighting potential ($A_{mesh} = 50 \mu m$) and in absence of weighting potential in the absorption layer, respectively. The $DQE(f)$ performance increases due to the actual weighting potential in the absorption layer. As seen in Figure 4.4, weighting potential decreases when the A_{mesh} decreases. However, the fill factor depends on the value of A_{mesh} . When the A_{mesh} decreases, Wronski et al. [124] have shown that the fill factor also decreases.

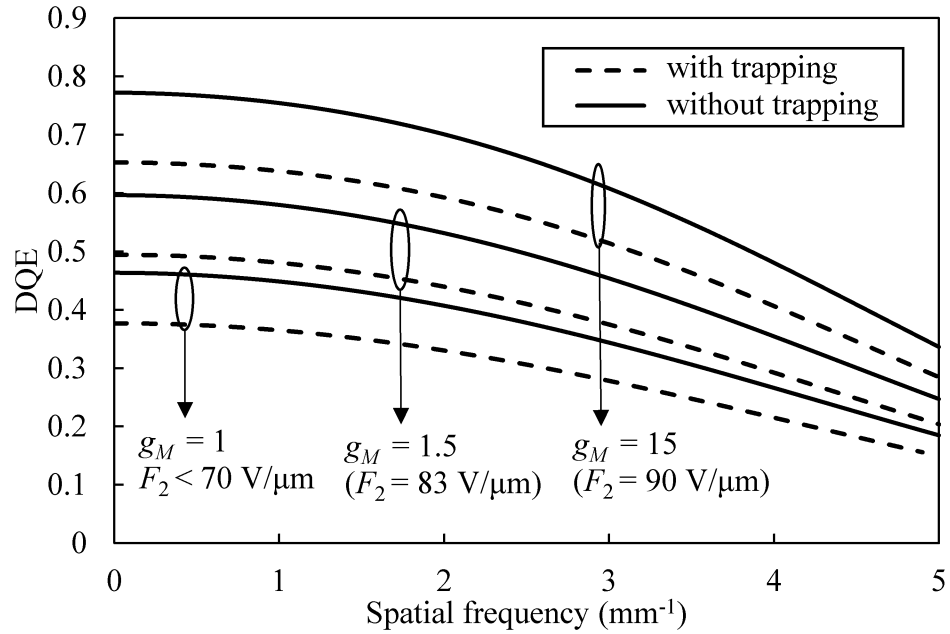


Figure 4.8 DQE(f) at different electric fields hence different avalanche gains.

Avalanche multiplication offers the gain which helps the detector to increase the DQE even when carriers are trapped in the absorption layer. Figure 4.8 shows DQE(f) at different electric fields when $N_e = 1500$ e/pixel, $X = 1$ μ R and $\tau_h = 30$ μ s. The dashed and solid lines represent DQE with and without carrier trapping, respectively. The DQE at Nyquist frequency, f_N (5 mm^{-1}) drops from 0.19 to 0.15 due to the carrier trapping, when F_2 (in the gain region) less than 70 $\text{V}/\mu\text{m}$. The avalanche gain improves the detector performance with increasing the field thereafter. It is evident from the Figure 4.8 that an electric field of 90 $\text{V}/\mu\text{m}$ (corresponds to an avalanche gain of ~ 15 when L_2 is 50 μm) improves the DQE(f_N) to 0.34.

Figure 4.9 shows the DQE(f) of a multilayer direct conversion x-ray detector with grid electrode at different avalanche gains. The lower end of the dose range in fluoroscopy (0.1 μ R of x-ray exposure per frame) is considered. The dots represent the DQE(f) without electronic noise ($N_e =$

0). An avalanche gain of 35 (corresponds to the field of ~ 91 V/ μm when L_2 is $50\mu\text{m}$) overcomes the adverse effect of the electronic noise of 1500 e/pixel whereas the required gain is 20 (electric field of 90 V/ μm for $L_2 = 50 \mu\text{m}$) to overcome the effect of the electronic noise of 700 e/pixel. From the results, we can conclude that avalanche gain improves the signal strength and overcomes the adverse effect of carrier trapping and electronic noise.

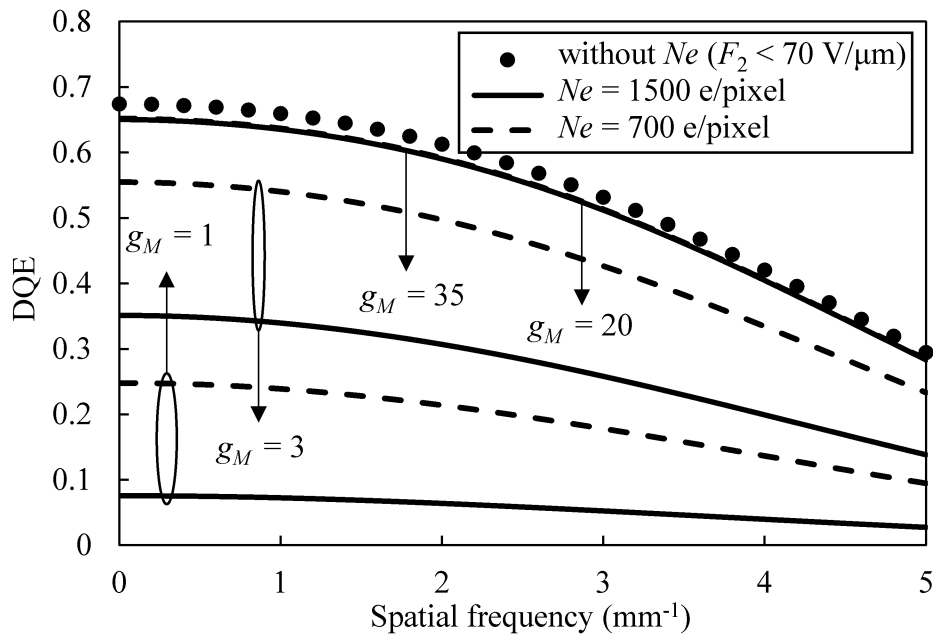


Figure 4.9 Calculated DQE(f) at different avalanche gains. The solid ($g_m = 35$) and dashed ($g_m = 20$) lines overlap.

Figure 4.10 shows the effects of the applied electric field (F_2) in the gain region on DQE(0) at different exposures. The DQE(0) saturates when electric field goes beyond 92 V/ μm . The DQE(0) improves significantly with increasing exposure. It is evident from the Figure 4.10 that the avalanche gain is more important at low exposure and/or higher electronic noise.

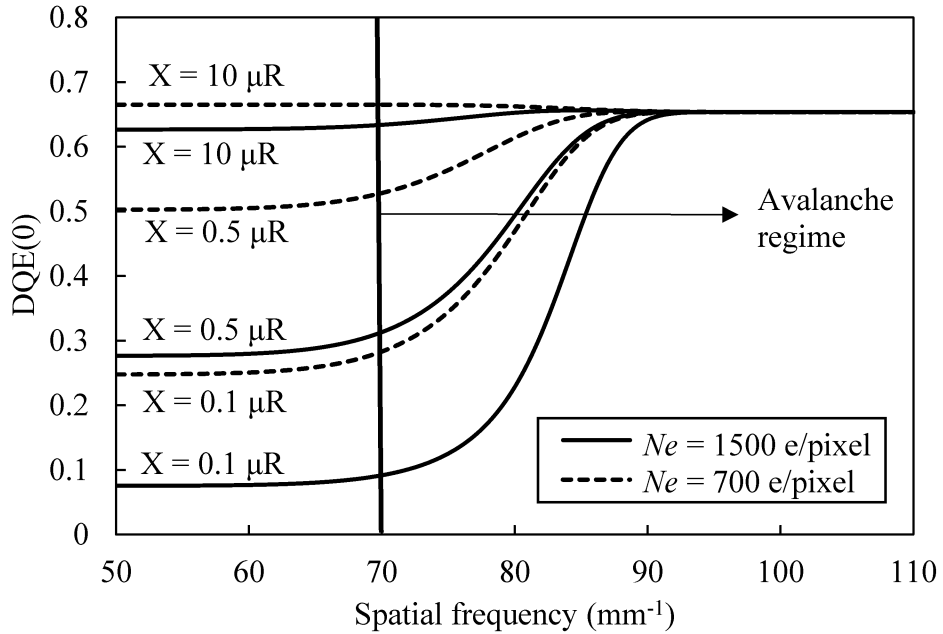


Figure 4.10 DQE(0) as a function of applied electric field for different fluoroscopic exposures.

4.5 Summary

A cascaded linear-system model including collection efficiency assuming the actual weighting potential, blurring due to carrier trapping and K -fluorescence reabsorption is developed for a-Se based multilayer direct conversion avalanche x-ray detector in this paper. It is found that the charge carrier trapping and non-zero weighting potential in the absorption layer have pronounced effect on the performance of the detector. However, the trapping effect becomes negligible when the hole lifetime is increased in the range of 100 μ s or above. An avalanche gain of 35 and 20 are sufficient to overcome the effect of carrier trapping (when hole lifetime is 30 μ s) together with the effect of electronic noise of 1500 and 700 e/pixel, respectively.

CHAPTER 5

A Novel Amorphous Selenium Avalanche Detector Structure for Low Dose Medical X-ray Imaging

The contribution of this chapter has recently been published [131]. Most of the materials are taken from the published manuscript.*

A novel structure for direct conversion avalanche detector is proposed for low dose medical x-ray imaging, such as tomography. The structure contains a hole trapping layer (hereinafter trapping layer) which separates the absorption layer from the gain region. The trapping layer changes the potential profile across the detector by trapping positive charges (injected holes) and hence increases the electric field in the gain region up to a value that is required for avalanche multiplication of x-ray generated holes. This eliminates the necessity of the intermediate electrodes to obtain avalanche multiplication without gain fluctuation. A numerical model is developed using the Semiconductor Module of COMSOL Multiphysics to analyze the device performance. We have simulated the electric field profile as a function of various device parameters. A detailed analysis of the transient electric field considering carrier injection in the presence of blocking and trapping layers is performed. The model is then used to predict the dark current behavior as a

* S. M. Arnab, and M. Z. Kabir. "A Novel Amorphous Selenium Avalanche Detector Structure for Low Dose Medical X-ray Imaging." *IEEE Transactions on Radiation and Plasma Medical Sciences* (2019)

function of time. A cascaded linear-system model that considers the effect of reabsorption of K -fluorescent x-rays, carrier trapping in bulk and trapping layer and avalanche multiplication of charge carrier is used to calculate the spatial frequency dependent detective quantum efficiency, $DQE(f)$ and modulation transfer function (MTF) of the proposed structure. The $DQE(f)$ of the proposed structure is compared with published experimental results of a commercially available detector at low x-ray exposures (e.g., exposures used in tomosynthesis). The model evaluates the impacts of avalanche gain on the proposed device performance at various frequencies. The effect of average electric field in different layers on zero frequency, $DQE(0)$ is also evaluated. The simulation results show the feasibility of the proposed structure for low dose direct conversion x-ray detectors.

5.1 Introduction

Amorphous selenium (a-Se) based direct conversion (i.e., the x-ray photons directly create electron-hole pair, EHP, in the photoconductor layer) active matrix flat panel imagers (AMFPI) have made a significant progress in mammography industry [98][105][129]. However, in very low exposure applications (i.e., fluoroscopy and tomography), the performance of FPI is not adequate [92]. Tomosynthesis is a promising and relatively new advancement in mammography. It increases the visibility of overlapped masses (called calcifications) in the breast. In breast tomosynthesis a sequence of images is captured while the x-ray tube is positioned at different angles with respect to the breast and the total dose for all the images in the sequence is kept same as that of a single

image in regular screening mammography. The average x-ray exposure of each image depends on the total number of views (e.g., 25) [132]. Therefore, the exposure used for each image in tomosynthesis is significantly reduced [133], [134]. As a result, the detector can be vulnerable to the electronic noise (N_e) caused by the readout circuitry. The objective of this work is to improve the DQE for the same exposure levels so that the image quality can be potentially enhanced.

Problems arising from the electronic noise can be solved either by reducing the electronic noise itself or by increasing the internal gain of the imaging system [94][118][135]. The CMOS active pixel sensor (APS) shows almost an order of magnitude lower electronic noise (per pixel) than the commonly used a-Si technology when the pixel size is very small (~ 25 μm) [94]. However, larger CMOS APS sensors show higher electronic noise [95]. Moreover, the APS is vulnerable to the radiation damage [136].

On the other hand, replacing the commonly used photoconductor (i.e., a-Se) with the high conversion gain photoconductor such as HgI_2 , PbO or Perovskites can increase the internal gain [137][138][139]. However, none of these high gain photoconductors are systematically examined for long term performance stability. The internal gain can also be increased with the help of avalanche multiplication technique [115]. In this case, exponential x-ray absorption over thick layer causes a huge avalanche gain fluctuation noise [118]. Therefore, a thin layer is required for avalanche and it has to be separated from the x-ray absorption layer. An indirect conversion (i.e., x-ray photons create light photons in a phosphor layer and these light photons are then detected by photodiodes) detector is suitable for avalanche gain [88]. However, the resolution in terms of the modulation transfer function (MTF) of indirect conversion detectors is inferior compared to that

of direct conversion detectors due to the omni-directional propagation of light photons in the phosphor [88].

Wronski and Rowlands [97] proposed a partitioned a-Se structure that consists of a thick x-ray absorption layer and a subsequent thin region for avalanche multiplication by inserting intermediate electrodes and utilizing two voltage supplies for direct conversion x-ray detectors [88]. The structure is too complicated, and its practical feasibility and performance are yet to be determined. A feasible and simple structure for direct conversion avalanche detector is therefore required.

In a-Se based direct conversion avalanche detectors, an electric field of ~ 10 V/ μm in the absorption layer is necessary for obtaining a reasonable EHP creation energy and collecting the photo-generated EHPs [69]. At the same time, a very high electric field (above ~ 70 V/ μm) is required for holes to initiate avalanche multiplication in the gain region [140]. Due to the applied electric field, a current flow across the detector in absence of x-ray irradiation which is known as dark current. The dark current acts as a source of noise and reduces the dynamic range of the detector [141]. Therefore the dark current in direct conversion avalanche detector, which operates at very high electric field, is of major concern because of the avalanche nature of the dark current [82]. It is assumed that the main source of the dark current is the carrier injection due to Schottky emission of charge carriers from the contact electrodes [87]. As a solution to this problem, blocking layers are deposited next to the electrodes. The blocking layers trap the injected carrier from the contacts, reduce the electric field at the contacts and thus reduce the dark current [82].

5.2 Structure of direct-conversion multilayer avalanche x-ray detector with trapping layer

Figure 5.1 shows the cross section of the proposed structure of an a-Se based direct-conversion multilayer avalanche detector with trapping layer. The figure also shows the electric field distribution along the thickness of the detector. It is assumed that, initially (right after applying the bias voltage), the electric field remains constant (F_0) throughout the detector [50]. As time elapses, two different levels of electric fields, a) the field (F_1) for collecting the photo generated EHPs in the absorption layer and, b) the field (F_2) for avalanche multiplication of holes in the gain region, are formed. The electric field at the radiation receiving electrode (top electrode) and pixel electrodes are F_{te} and F_{pe} , respectively.

The detector is designed for mammographic applications. Therefore, it consists of a thick ($L_2 = 200 \mu\text{m}$) absorption layer. In order to avoid crystallization in the absorption layer, a-Se is usually alloyed with small fraction of As (i.e., a- $\text{Se}_{1-m}\text{As}_m$, where $m = 0.003$) and doped with 5-20 ppm Cl [82][81]. The absorption layer is followed by the trapping layer. The thickness of trapping layer (L_3) is $5 \mu\text{m}$. The trapping layer is then followed by the avalanche gain region which has a thickness (L_4) of $20 \mu\text{m}$. An n -like blocking layer (L_1) is deposited between the top electrode and absorption layer to block the hole injection and a p -like blocking layer (L_5) is deposited between the gain and pixel electrodes to block the electron injection. These blocking layers are not same as conventional p -type and n -type layers. These blocking layers are doped in such a way that they transport only one charge carrier (i.e., either electrons or holes) [50][81]. This means that the p -like and n -like blocking layers have very high concentration of deep electron and hole trap centers, respectively.

The p -like blocking layer is usually $a\text{-As}_2\text{-Se}_3$ and the n -like blocking and trapping layers are alkali metal (e.g., sodium) doped $a\text{-Se}$. The n -like blocking and trapping layers are also alloyed with up to 10% As to prevent crystallization [81][142]. The hole trap density in these layers depends on the doping level. For simplicity, the p -like and n -like blocking layers is referred as p -layer and n -layer, respectively in this paper. The thickness of the blocking layers is $6\ \mu\text{m}$.

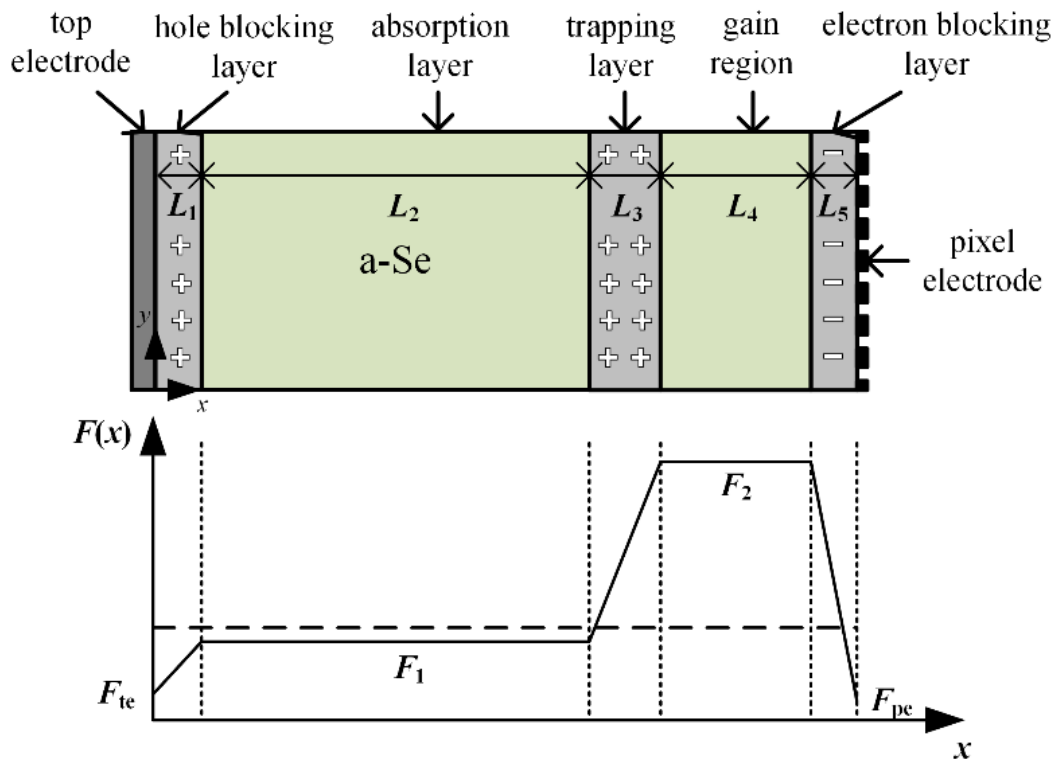


Figure 5.1 Cross sectional diagram showing an $a\text{-Se}$ based direct-conversion multilayer avalanche x-ray detector with trapping layer and the time dependent electric field profile. The dashed line shows the initial electric field (F_0) and the solid line shows the electric field profile as the time elapses. Drawing is not to scale.

The x-rays are absorbed and EHPs are created in the absorption layer under an electric field (F_1) of $\sim 10\ \text{V}/\mu\text{m}$ [50]. The trapping layer sets up a high electric field, F_2 ($\sim 70\text{-}110\ \text{V}/\mu\text{m}$) within the

gain region to initiate the avalanche multiplication of x-ray generated holes. When the top electrode is positively biased, the x-ray photon generated holes travel towards the trapping layer and undergo avalanche multiplication in the gain region while travelling towards the pixel electrodes.

5.3 Modeling by numerical calculations

The mathematical equations required to explain the behavior of the detector, are highly nonlinear. Therefore, a numerical model to predict the behavior of the proposed direct conversion avalanche detector is presented. The simulations are performed using Semiconductor Module of COMSOL Multiphysics.

The Semiconductor Module of COMSOL Multiphysics solves Poisson's equation in conjunction with the continuity equations for the charge carriers. The Poisson's equation is given below [143],

$$\nabla \cdot (\epsilon_s \nabla V) = -q(p - n + N_f) \quad (5.1)$$

where V is the electric potential, p and n are the free hole and electron concentrations, $\epsilon_s (= \epsilon_o \epsilon_r)$ is the permittivity of a-Se, q is the elementary charge, N_f is the concentration of additional fixed charges which originates from impurities and/or trapped carriers. The continuity equations are given by

$$\frac{\partial n}{\partial t} = \frac{1}{q} (\nabla \cdot J_e) - U_e \quad (5.2)$$

$$\frac{\partial p}{\partial t} = \frac{1}{q} (\nabla \cdot J_h) - U_h \quad (5.3)$$

where t is the instantaneous time, J is the current density and U is the net recombination rate. The subscripts, e and h stand for electron and hole, respectively. The net recombination is calculated from all generation (G) and recombination (R) mechanisms and given by,

$$U = \sum_i R_i - \sum_i G_i \quad (5.4)$$

The electron and hole conduction current densities are given by the following equations,

$$J_e = qn\mu_e \nabla E_c + \mu_e k_B T \nabla n \quad (5.5)$$

$$J_h = qp\mu_h \nabla E_v + \mu_h k_B T \nabla p \quad (5.6)$$

where E_c and E_v are the conduction and valance band energies, respectively, T is the temperature, k_B is the Boltzmann constant and μ is the carrier mobility.

5.3.1 Carrier Injection

The contacts used in the detectors are usually blocking in nature. Therefore, the carrier injection from the contacts mainly depends on the transportation of carriers over the potential barrier between contact and photoconductor, which can be described by the diffusion theory [144]. The electron and hole injection current densities are as follows [143],

$$J_e^{inj} = -qv_e (n - n_0) \quad (5.7)$$

$$J_h^{inj} = qv_h(p - p_0) \quad (5.8)$$

According to diffusion theory the instantaneous drift velocity of the injected electron and hole are given by, $v_{e(h)} = \mu_{e(h)} F_{pe(te)}$. In Eq. (5.7) and Eq. (5.8), n_0 and p_0 are the quasi-equilibrium carrier densities at the contacts and given by the following equations [82][144].

$$n_0 = N_C \exp \left[-\frac{\phi_e - \Delta\phi_e(F_{pe})}{k_B T} \right] \quad (5.9)$$

$$p_0 = N_V \exp \left[-\frac{\phi_h - \Delta\phi_h(F_{te})}{k_B T} \right] \quad (5.10)$$

where, ϕ_e and ϕ_h are the effective electron and hole barrier heights considering the effects of surface states at the pixel and top electrodes, respectively. In Equations 5.9 and 5.10, the term $\Delta\phi$ within the exponentials represents the field dependent barrier lowering. The barrier lowering depends on numerous physical phenomena such as rearrangement in the interfacial layer, image force induced potential barrier lowering and/or trap-assisted tunneling. In this work, we have considered image force barrier lowering and therefore $\Delta\phi$ becomes $\sqrt{q^3 F / 4\pi\epsilon_s}$. The total dark current density thus becomes, $J_d = J_e^{inj} + J_h^{inj}$.

5.3.2 Carrier trapping in different layers

In a-Se photoconductor, defect states appear in the mobility gap. These defect states act as trapping or recombination centers for charge carriers. In this work, the energy distribution of the defect

states is assumed to be discrete. The proposed model considers shallow and deep defect states in a-Se for both charge carriers. The shallow traps capture the carriers for a small amount of time and thus only alter the effective mobility of the carriers. In the blocking and trapping layers, a single energy state of the deep trap is considered. The exact position of the energy states depends on the fabrication technique, degree of doping impurities and the evaluation technique [145]. The electron (r_e) and hole (r_h) trapping rates are given by the following equations [144],

$$r_e = C_n N_t [n - n f_t - n_1] \quad (5.11)$$

$$r_h = C_p N_t [p f_t + (p_1 f_t - p_1)] \quad (5.12)$$

where C_n and C_p are the constants proportional to electron and hole-capture cross section, respectively, N_t is the total density of deep trap centers, and $f_t = 1/[1 + \exp(E_t - E_f)]$ is the probability of a trap state to be occupied by an electron where E_t and E_f are the trap energy level and the Fermi energy level, respectively. The parameters $n_1 = n_i \exp[(E_t - E_i)/k_B T]$ and $p_1 = n_i \exp[(E_i - E_t)/k_B T]$, where n_i is the intrinsic carrier concentration. The rate of change of the number of trapped electrons at energy E_t is

$$N_t \frac{\partial f_t}{\partial t} = r_e - r_h \quad (5.13)$$

The charge density in the blocking and trapping layers depend on trap occupancy. The trap densities in the n , p and trapping layers are N_t^h , N_t^e and N_t^t , respectively.

5.3.3 Electric field profile

After applying the bias voltage, trapping of the injected holes at the n -layer and the injected electrons at the p -layer, create positive and negative space charge regions near the top and pixel electrodes, respectively. Similarly, the injected holes which survive trapping at the n -layer, create a positive space charge region at the trapping layer. The trap density in the n -layer is assumed to be less than that of the trapping layer so that the injected holes can contribute to the space charge region formed at the trapping layer. The integral of the electric field distribution across the detector is equal to the applied voltage. Therefore, the field across the detector depends on the charge distribution which is related to the trap densities and occupancy (as mentioned in section 5.3.2). As positive space charge builds up in the trapping layer, the electric field in the gain region starts increasing and, consequently, the electric field in the absorption layer decreases, as shown in Figure 5.3. The increasing electric field (after a certain value) initiates impact ionization of the holes in the gain region.

5.3.4 Avalanche gain

The avalanche multiplication caused by impact ionization of charge carriers increases the signal strength. However, it can also increase the noise by multiplying the dark current density. Impact-ionization coefficients (β) of charge carrier is used to identify the impact-ionization rate. It describes the number of EHPs created per unit distance traveled by a charge carrier. While the

electric field in the gain region is within a range of 70-120 V/ μm , only holes participate in the avalanche multiplication process [106]. The avalanche gain depends on L_4 and given by [140],

$$g_M = \exp[\beta L_4] \quad (5.15)$$

5.3.5 Blurring due to charge carrier trapping

The charge carrier trapping reduces the charge collection efficiency and also reduces the MTF by inducing charges on the neighboring pixels. The analytical model developed by Kabir and Kasap [120] have been used to evaluate the MTF, $T_{tr_L_2}(E, f)$ due to distributed carrier trapping in L_2 .

The carrier trapping in L_3 also reduces the overall MTF of the system. The following equation is used to calculate the MTF, $T_{tr_L_3}(L, f)$ due to carrier trapping in L_3 [146], [147],

$$T_{tr_L_3}(L, f) = \left[\frac{(1-p_{nt_L_3}) \sinh(2\pi f L_2)}{\sinh\{2\pi f (L_2+L_4)\}} + p_{nt_L_3} \right] / \left[\frac{(1-p_{nt_L_3}) L_2}{(L_2+L_4)} + p_{nt_L_3} \right] \quad (5.16)$$

where, $p_{nt_L_3} = \exp\left[-L_3 / (\mu_h \tau_h' F_2)\right]$ is the probability of a hole to successfully cross L_3 without being trapped. The lifetime of the x-ray generated holes in L_3 depends on the density of the unoccupied traps.

5.4 Cascaded Linear System Model

In this paper, we have modified our previously developed cascaded linear-system model to adapt with the current structure and evaluate the DQE(f) and MTF performance of the proposed structure [115]. Figure 5.2 represents the imaging processes involved in the proposed detector structure. It assumes that the absorption layer is distinct from the gain region. The hole trapping in the absorption (L_2) and trapping (L_3) layers is taken into consideration as only the holes that survive in these layers participate in the avalanche multiplication process in the gain region. The decision stages called “Trap” decide the probability of holes that participates in the avalanche gain multiplication. Due to the facts that the carriers travel a very short distance and high electric field exists in the gain region, carrier trapping is not considered in the gain region. A detailed description of the model and the processes involved can be found in Ref. [115]. This paper contains the changes that are made in the model to make it applicable to the proposed structure.

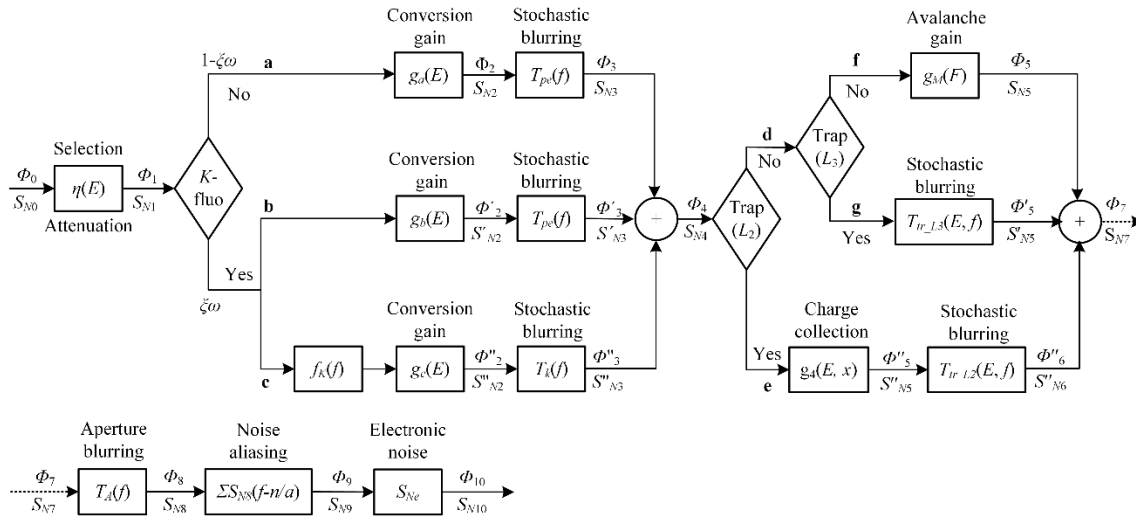


Figure 5.2 Diagram showing the flow of signal and noise power spectrum in the cascaded linear system model. Here ξ is the probability of K -shell interaction, ω is the probability of K -

fluorescence production and f_k is the average reabsorption probability of K -fluorescent x-ray photons within the photoconductor volume.

The equations to compute the signal and noise power spectrum (NPS) up to the third stage of the cascaded linear-system model (Figure 5.2) remain the same as the previous model. Therefore, the expressions of $\phi_4(f)$ and $S_{N4}(f)$ are taken from Ref. [115]. After summing the signal and NPS from path f , g and e , the resultant $\phi_7(f)$ and $S_{N7}(f)$ are

$$\phi_7(f) = \phi_4(f) \left[p_{nt_L2} \left\{ p_{nt_L3} g_M + T_{tr_L3} (1 - p_{nt_L3}) \right\} + T_{tr_L2} g_4 (1 - p_{nt_L2}) \right] \quad (5.17)$$

$$\begin{aligned} S_{N7}(f) = & p_{nt_L2} p_{nt_L3} \left[g_M^2 \{ S_{N4}(f) + \phi_4 \} - g_M \phi_4 \right] \\ & + p_{nt_L2} (1 - p_{nt_L3}) \left[T_{tr_L3}^2 \{ S_{N4}(f) - \phi_4 \} + \phi_4 \right] \\ & + (1 - p_{nt_L2}) \left[T_{tr_L2}^2 \{ g_4^2 S_{N4}(f) + \sigma_{g_4}^2 \phi_4 - g_4 \phi_4 \} \right. \\ & \left. + g_4 \phi_4 \right] \end{aligned} \quad (5.18)$$

where, p_{nt_L2} is the average probability of a hole reaching to the trapping layer, g_M is the avalanche gain, g_4 is the mean collection efficiency and $\sigma_{g_4}^2$ is the mean charge collection gain variance [115].

After aperture blurring, the signal and NPS becomes,

$$\phi_8(f) = T_A(f) \phi_7(f) \quad (5.19)$$

$$S_{N8}(f) = T_A^2(f) S_{N7}(f) \quad (5.20)$$

The resulting noise after aliasing stage is given by,

$$S_{N9}(f) = S_{N8}(f) + \sum_{n=-\infty}^{\infty} S_{N8}\left(f - \frac{n}{a}\right) \quad (5.21)$$

After adding the electronic noise power, S_{Ne} , to the total noise power, the signal and noise at the output of the tenth stage (electronic noise) are,

$$\phi_{10}(f) = \phi_8(f) \quad (5.22)$$

$$S_{N10}(f) = S_{N9}(f) + S_{Ne} \quad (5.23)$$

The input NPS, $S_{n0} = \phi_0$, is the mean photon fluence. Thus, the frequency dependent $DQE(f)$, can be written as,

$$DQE(f) = \frac{\phi_{10}^2(f)}{\phi_0 S_{N10}(f)} = \frac{[G \times MTF(f)]^2}{\phi_0 S_{N10}(f)} \quad (5.24)$$

where G is the pixel response.

5.5 Results and discussion

A 1-Dimensional (1-D) model of the structure mentioned in Sec. II has been developed using the Semiconductor Module of COMSOL Multiphysics. The model is then discretized using Finite Element Method (FEM).

Kabir and Imam [148] has estimated the traps concentrations at discrete trap energy levels (within the energy bandgap) in the n -layer by fitting experimental results. Frey et al. [81] have also fitted the same set of experimental results using a similar model considering carrier trapping in both n and p -layers. The trap concentration in these layers heavily depend on the fabrication processes. Therefore, in our simulations, we have kept the values of these parameters within an acceptable range around the previously published values.

Figure 5.3 shows the transient behavior of the electric field across the proposed a-Se based direct-conversion multilayer avalanche detector with trapping layer. The values of the parameters N_t^e , N_t^h and N_t^t are assumed to be 5×10^{15} , 4×10^{15} and 10^{16} cm^{-3} , respectively. The concentration of the shallow and deep traps in a-Se for both electrons and holes are 4×10^{14} and 8×10^{12} cm^{-3} , respectively [82][149]. The thicknesses of different regions are, $L_1 = 6$ μm , $L_2 = 200$ μm , $L_3 = 5$ μm , $L_4 = 20$ μm and $L_5 = 6$ μm . The applied voltage is 4.7 kV. The effective barrier to electron injection at the pixel electrode and to hole injection at the top electrode is assumed to be ~ 0.75 eV [148]. The used values of all other parameters are shown in Table 5.1. Unless stated otherwise, the mentioned values of the parameters are fixed for all the theoretical calculations.

Table 5.1 Parameters used in the simulations

Parameters	Values
Relative permittivity, Ref [82]	6.7
Bandgap (E_g), Ref [82]	2.2 eV
Deep trapping capture coefficient (C_t), Ref [150]	5×10^{-8} cm^3/s
Hole mobility (μ_p), Ref [137]	0.12 $\text{cm}^2/\text{V}\cdot\text{s}$
Electron mobility (μ_n), Ref [137]	0.003 $\text{cm}^2/\text{V}\cdot\text{s}$
Effective DOS in valence band (N_V), Ref [82]	1×10^{19} cm^{-3}
Effective DOS in conduction band (N_C), Ref [82]	1×10^{19} cm^{-3}

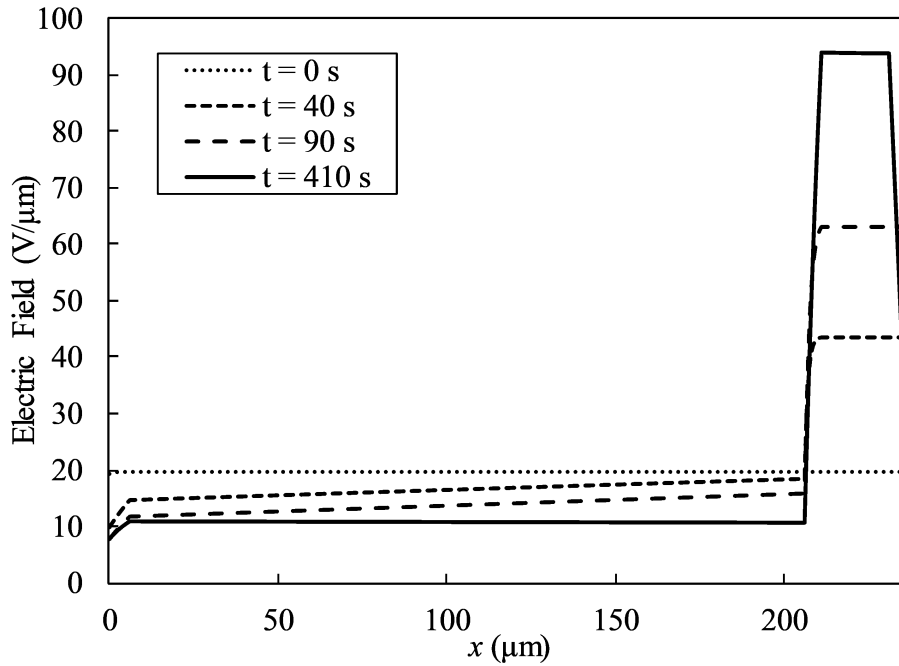


Figure 5.3 Electric field distribution at different times. The electric field is uniform across the detector at $t = 0$ s.

The dark current is mainly governed by hole injection from the positive electrode [50]. The injection is reduced by lowering the electric field at the contact between metal and semiconductor. In Figure 5.3, it is shown that the electric field remains constant throughout the detector right after applying bias voltage (i.e., $t = 0$). Over the time, formation of space charge region alters the electric field profile and hence the value of F_{te} . The space charge formation in the blocking and trapping layers depends on the trapping and de-trapping rate of charge carriers in these layers. A steady state is achieved when the trapping and de-trapping rate at each layer becomes equal. In steady state condition, the average electric fields in the absorption ($F_{1,avg}$) and gain ($F_{2,avg}$) regions are ~ 10.8 V/ μm and ~ 94 V/ μm , respectively.

A minimum of ~ 70 V/ μm of electric field in the gain region is required to initiate avalanche multiplication of x-ray generated holes [140][151]. Therefore, the values of the parameters governing F_2 have to be carefully determined. It is observed that L_3 and N_t^t have significant effects on the transient behavior of F_2 . Figure 5.4 and 5.5 show the impact of L_3 and N_t^t on the average value of the electric field in the gain region ($F_{2,avg}$), respectively.

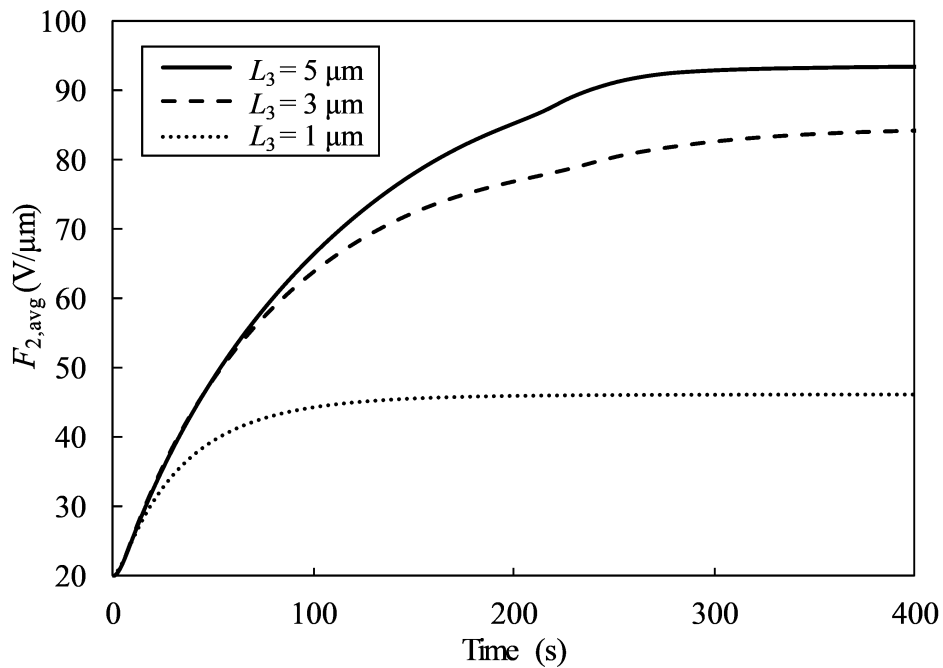


Figure 5.4 Average electric field in the gain region after applying bias voltage for different thicknesses of trapping layer.

In Figure 5.4, the applied bias voltage is changed for each value of L_3 to keep the applied initial electric field to a fixed value of 19.8 V/ μm . The thicknesses of all other regions are kept unchanged. It is observed that the saturated value of $F_{2,avg}$ decreases when L_3 is reduced. The value of $F_{2,avg}$ saturates at ~ 94 and ~ 46 V/ μm when L_3 is 5 and 1 μm , respectively. Therefore, the

optimum thickness of the trapping layer should be fixed considering the desired avalanche gain and the operating voltage. The value of $F_{2,avg}$ increases after applying the bias voltage and depending on L_3 , it becomes stable after a certain time.

Figure 5.5 shows the effect of trap density in the trapping layer on $F_{2,avg}$. The steady state value of $F_{2,avg}$ decreases from ~ 94 to ~ 34 V/ μm when N_t^t is decreased from 1×10^{16} to 1×10^{15} cm^{-3} , respectively. On the other hand, it takes ~ 65 and ~ 370 s to obtain a steady value of $F_{2,avg}$ when N_t^t is 1×10^{15} and 1×10^{16} cm^{-3} , respectively. Although reducing the trap density in the trapping layer lessens the time required to achieve the steady state condition, it reduces the steady state value of electric field in the gain region which in turn reduces the avalanche gain.

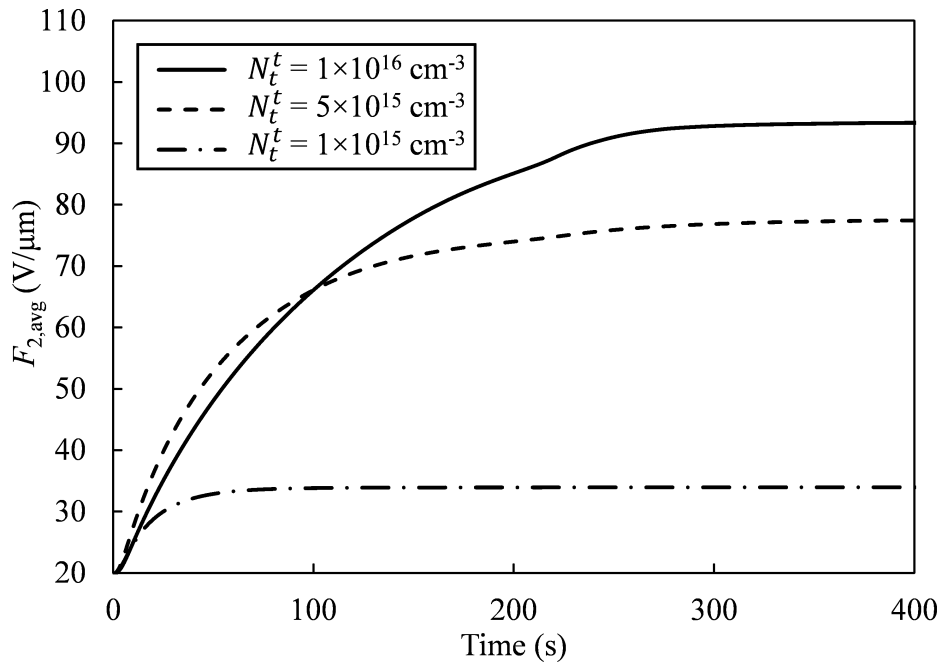


Figure 5.5 Average electric fields in the gain region as functions of time after applying bias voltage of 4.7 kV for different values of N_t^t . The trapping layer thickness is 5 μm .

Not only the x-ray generated holes participate in the avalanche multiplication process, but also the injected holes take part in this process. As a result, impact ionization of holes enhances the dark current density. Figure 5.6 shows the effect of impact ionization of holes on the dark current density when $L_3 = 5 \mu\text{m}$ and $N_i' = 10^{16} \text{cm}^{-3}$.

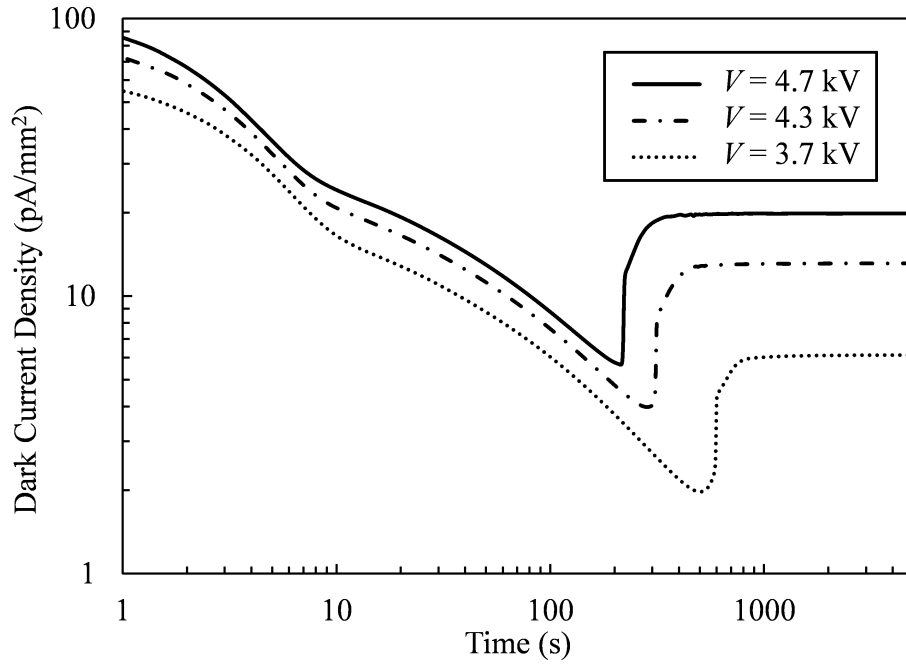


Figure 5.6 Effect of applied bias voltage on the dark current density as a function of time.

It is evident from Figure 5.6 that the dark current decreases rapidly after applying the bias voltage and a sudden rise occurs when a significant number of charge carriers are generated in the gain region due to impact ionization (see Figure 5.4 and 5.5). It is also observed that the dark current saturates at a lower value when the voltage is decreased from 4.7 to 3.7 kV. However, it takes a longer time to achieve steady state when the voltage is reduced. Although the dark current is higher than previously reported values [81], it is still in the same order of magnitude. Assuming the time between two subsequent readouts to be 0.8 s [152], the additive electronic noise due the dark

current density (~ 20 pA/mm²) increases by only 140 e/pixel when the total electronic noise (from other sources) is assumed to be 2500 e/pixel.

The DQE(f) is the most commonly used metric of imaging performance of a detector. In this paper, DQE(f) of the proposed structure is evaluated by considering a standard mammography energy spectrum (28 kVp with tungsten target and 50 μ m rhodium filter) in order to ensure better signal to noise ratio for tomosynthesis [152]. In the simulations, the x-ray exposures is kept very low, such as, 0.41 and 1.02 mR [132]. The values of W_{\pm} for varying electric field in the absorption layer are taken from Ref. [153]. The electron and hole lifetimes are 200 and 30 μ s in the absorption layer, respectively [137].

In Figure 5.7, the DQE(f) performance of the direct-conversion multilayer avalanche detector is compared with published experimental results of an a-Se based direct conversion detector used in tomosynthesis at low x-ray exposures. The pixel size is 85 μ m and the absorption layer thickness is 200 μ m.

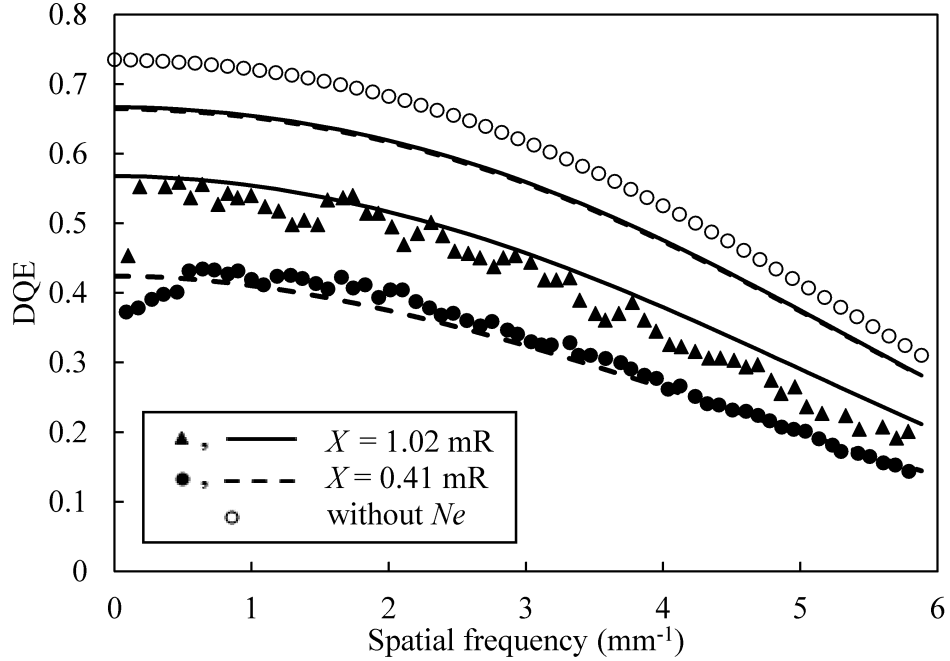


Figure 5.7 Comparison between $DQE(f)$ of an a-Se based direct conversion detector used in tomosynthesis and that of the proposed structure calculated using the cascaded linear system model. The solid symbols are the measured $DQE(f)$ at different x-ray exposures. The solid and dashed lines are $DQE(f)$ calculated using the developed model at 1.02 and 0.41 mR, respectively. These lines overlap when avalanche multiplication is considered in the proposed structure. The measured values are obtained from Ref. [132].

The solid symbols represent the measured DQE as a function of spatial frequency at different x-ray exposures. The figure also shows the theoretical fit to the experimental findings. The value of N_e is considered to be 2500 e/pixel and the hole blocking layer is assumed to be 12 μm , which are exaggerated from the true values to account for the additional noise due to image correction as described in Ref. [152]. The cascaded linear system model without avalanche multiplication and charge trapping in L_3 agrees well with the measured $DQE(f)$ at different x-ray exposures. The model is then used to plot the $DQE(f)$ of the proposed structure (i.e., including avalanche multiplication) at similar x-ray exposures. The unoccupied trapping states in L_3 trap some fraction

of the x-ray generated holes and reduce the x-ray signal. The value of p_{m-L_3} is calculated to be 0.94 when L_3 is 5 μm . It shows that the proposed structure uses avalanche gain ($g_M = 11$ when $L_4 = 20 \mu\text{m}$ and $F_{2,avg} = 94 \text{ V}/\mu\text{m}$) to improve the $\text{DQE}(f)$ by overcoming the effect of electronic noise at low exposures. The $\text{DQE}(f)$ of the proposed structure is close to the calculated $\text{DQE}(f)$ without electronic noise (open symbols in Figure 5.7), when the x-ray exposures are as low as 0.41 and 1.02 mR.

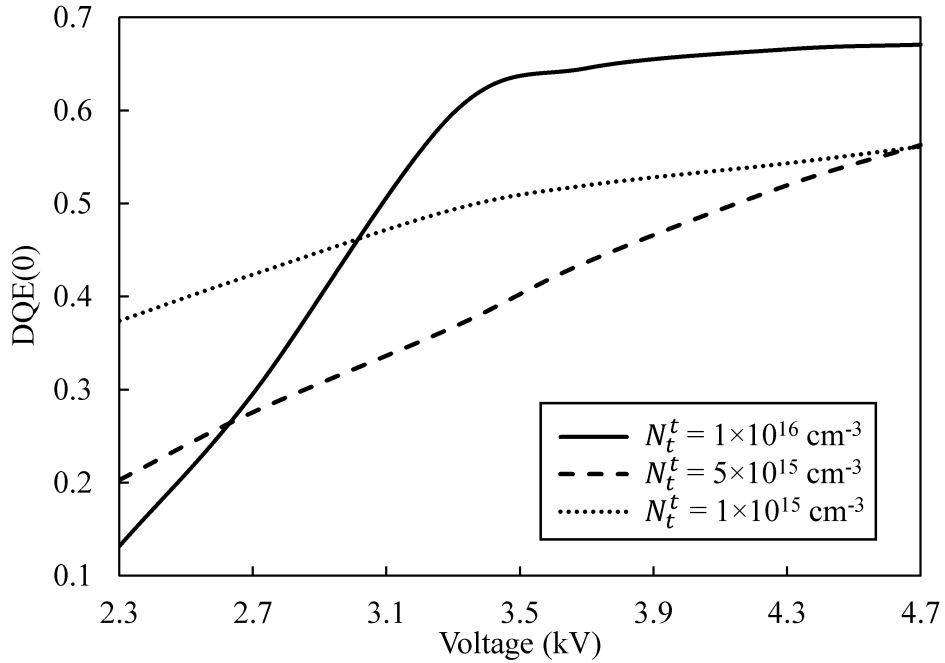


Figure 5.8 DQE(0) vs applied voltage for different trap densities in trapping layer. The x-ray exposure is 0.41 mR.

Figure 5.8 shows the DQE at zero frequency, $\text{DQE}(0)$ as a function of applied voltage for different trap densities in the trapping layer when the x-ray exposure is 0.41 mR. The values of the parameter used in the model to fit the experimental results are kept the same. The average values of F_1 and F_2 change when the applied voltage is varied. In the simulations, the values of W_{\pm} and g_M are

adjusted according to field variation. A sharp rise in DQE(0) at an applied voltage of 2.7 kV ($F_{2,avg} = 84.1 \text{ V}/\mu\text{m}$) is observed when N_t^t is $1 \times 10^{16} \text{ cm}^{-3}$. This rise is attributed to avalanche multiplication of the holes in the gain region. However such rapid increase in DQE(0) is not observed when N_t^t is 5×10^{15} and $1 \times 10^{15} \text{ cm}^{-3}$. It is due to the fact that the value of $F_{2,avg}$ is inadequate to obtain a substantial avalanche gain. It becomes ~ 77 and $\sim 34 \text{ V}/\mu\text{m}$ at $V = 4.7 \text{ kV}$ when N_t^t is 5×10^{15} and $1 \times 10^{15} \text{ cm}^{-3}$, respectively (see Figure 5.5). The avalanche gain remains as low as 1.2 and 1 when $F_{2,avg}$ is equal to ~ 77 and $\sim 34 \text{ V}/\mu\text{m}$, respectively. The smooth rise in DQE(0) is attributed to decreasing W_{\pm} with increasing field. It is also evident that at lower voltage (2.3 kV), the DQE(0) is higher when N_t^t is lower. It is because, in the absorption layer, the electric field decreases and W_{\pm} increases with increasing N_t^t . However, at higher voltages, avalanche gain compensates the increment of W_{\pm} .

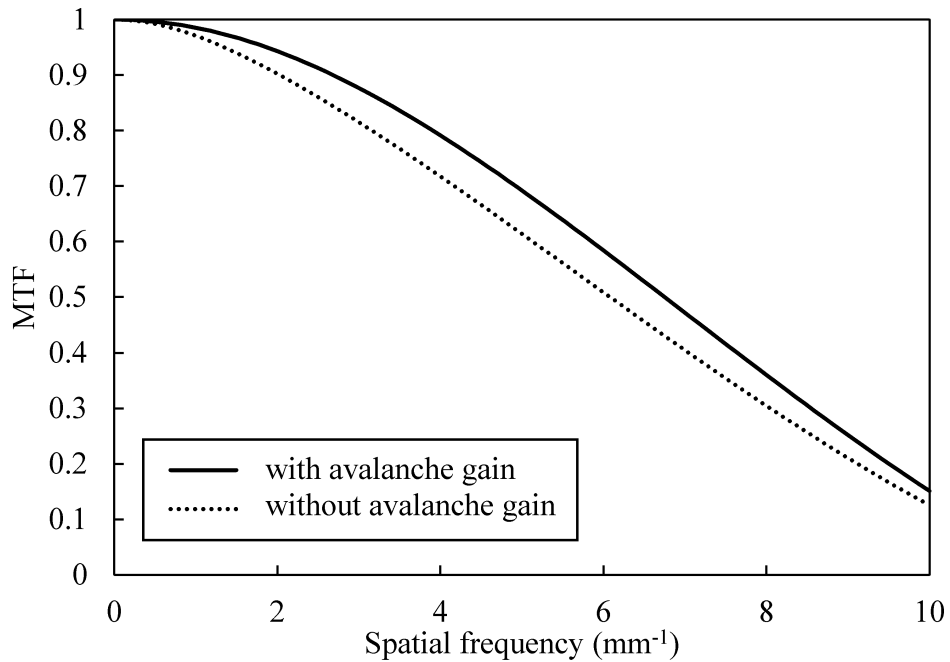


Figure 5.9 The effect of avalanche gain on presampling MTF. The solid and dotted lines represent the presampling MTF with and without avalanche gain, respectively.

The x-ray generated holes may get trapped in the trapping layer and induce charges in the neighboring pixels. Therefore, the trapped holes affect the MTF of the detector. Figure 5.9 shows the presampling MTF comparisons of the proposed and conventional structures considering charge carrier trapping in the trapping layer. The parameters in this figure are the same as in Figure 5.7. The avalanche gain compensates the loss of MTF due to trapping in L_3 as evident in Figure 5.9.

5.6 Summary

The feasibility of a simple multilayer avalanche a-Se detector structure for low-dose, such as, tomosynthesis direct-conversion x-ray imaging is investigated. The structure contains a hole trapping layer which separates the absorption layer from the gain region in which the charge undergoes avalanche multiplication. A numerical model is developed to analyze the transient electric field distribution across the detector and the dark current due to carrier injection. Although the dark current is higher in the proposed structure, it is in the same order of magnitude of previously reported values. The imaging performance, such as, $DQE(f)$ and MTF of the detector is evaluated using a cascaded linear system model. The results show that the direct-conversion multilayer avalanche detector ensures better imaging performance in terms of DQE compared to commercially available x-ray detectors. The proposed structure remains close to quantum noise limited detector even at very low x-ray exposures (0.41 mR) for breast tomosynthesis. This structure may also show high DQE for other low dose medical imaging applications.

CHAPTER 6

Comparison between different detector structures

In previous chapters, different digital x-ray detector structures are modeled. It has been shown that the avalanche multiplication of charge carriers enhances the imaging performance of those detectors. However, the relative performance of these detector structures will influence their clinical effectiveness. Therefore, it is necessary to assess and compare the performance of these detectors for different x-ray imaging modalities. The purpose of this chapter is to compute and compare the imaging performance of these avalanche detectors.

The Lubberts effect, which arises from the exponential x-ray absorption, adversely affects the performance of indirect conversion x-ray detectors. This effect is more pronounced when the thickness of the scintillator increases. The required thickness of the scintillator depends on the x-ray energy that varies with the imaging modality. On the other hand, charge carrier trapping in the absorption layer hinders the performance of a direct conversion x-ray detectors. Again, the severity of carrier trapping varies with the thickness of the absorption layer and the applied electric field. Since avalanche multiplication improves the signal strength and overcomes the effect of depth dependent x-ray absorption and carrier trapping, the required avalanche gain would vary for different imaging technique.

The electronic noise arising from the readout circuitry also plays a vital role on the performance of different detectors. The minimum required exposure in order to ensure quantum noise limited performance depends on the level of electronic noise. However, the minimum exposure level can be reduced by avalanche gain.

This chapter compares the imaging performance under various conditions of the following three detectors.

- a) Indirect conversion avalanche x-ray detector,
- b) Direct conversion avalanche x-ray detector with grid electrode,
- c) Direct-conversion multilayer avalanche x-ray detector with trapping layer.

In this chapter, the indirect conversion avalanche x-ray detector, the direct conversion avalanche x-ray detector with grid electrode, the direct-conversion multilayer avalanche x-ray detector with trapping layer are referred as indirect detector, direct detector with grid and direct detector with trapping layer, respectively.

The characteristics in terms of spatial frequency dependent detective quantum efficiency, $DQE(f)$ and modulation transfer function, MTF of these detectors are computed under different conditions and requirements of various imaging modalities, such as fluoroscopy and tomosynthesis. Both these imaging techniques requires very low x-ray exposures. Therefore, performance of a detector evaluated under the condition used for tomosynthesis would show better performance in mammography because the average exposure in mammography is higher than that in

tomosynthesis. Same for chest radiography, detector performance would be better in chest radiographic applications than in fluoroscopic applications. The considered imaging conditions and detector parameters for different detectors are shown in Table 6.1.

Table 6.1 Different parameters used for comparing the imaging performance of different avalanche detectors.

Clinical task	Tomosynthesis	Fluoroscopy
Pixel size	85 $\mu\text{m} \times 85 \mu\text{m}$	200 $\mu\text{m} \times 200 \mu\text{m}$ [154]
X-ray spectrum	30 kVp	70 kVp
X-ray exposure	0.41 mR	0.1 μR
Electronic noise	1500 e/pixel	1500 e/pixel

6.1 Performance comparison of detectors for fluoroscopic applications

The performance of the three aforementioned detectors are simulated using the models described in the previous chapters. The x-ray tube target/filter combination is tungsten/ aluminum and operated at 70 kVp. The thickness of the filter is 23.5 mm. Therefore, the average x-ray energy becomes 52 keV. The used values of the parameters for the detectors are tabulated in Table 6.2.

The quantum efficiency depends on the thickness and absorption coefficient of the absorption layer. In this chapter, the simulations are performed by considering similar quantum efficiencies for different detectors. In order to do so, the thicknesses of different absorption layers are varied.

The thickness of the absorption layer (i.e., a-Se) in direct detectors is assumed to be 1000 μm and the thickness of scintillator (i.e., CsI) in indirect detector is 385 μm . These values of thicknesses ensure a quantum efficiency of ~ 0.77 for all the detectors. The thicknesses of the rest of the layers are unchanged. The avalanche multiplication parameters β_1 and β_2 are $5.5 \times 10^3 \mu\text{m}^{-1}$ and $1.029 \times 10^3 \text{V}/\mu\text{m}$, respectively. The K -fluorescent x-ray photon reabsorption probability is calculated using the method of Dance and Day.

Table 6.2 Parameters used in the simulations

Parameters (unit)	Direct conversion	Indirect conversion
K -fluorescent X-ray energy (keV)	12.7	30.37
Probability of K -shell interaction	0.864	0.83
Probability of K -fluorescence production	0.596	0.88
EHP creation energy (eV)	~ 40	17
Electron mobility ($\text{cm}^2/\text{V}\cdot\text{s}$)	0.003	-
Electron lifetime (μs)	200	-
Hole mobility ($\text{cm}^2/\text{V}\cdot\text{s}$)	0.12	-
Hole lifetime (μs)	30	-

In indirect detector, the coupling efficiency between CsI and a-Se is assumed to be 0.8. The reciprocal of the photon relaxation and mean absorption length in CsI are 40 and 5 mm^{-1} , respectively. The reflectivity parameters of the CsI layer at the entrance and output are 0 and 1, respectively. The thickness of the avalanche gain region is 15 μm . On the other hand, the thicknesses of the avalanche gain regions in direct detectors with grid and trapping layer are 50

and 20 μm , respectively. The thickness of the trapping layer in direct detector with trapping layer is kept fixed at 5 μm .

Figure 6.1 shows the $\text{DQF}(f)$ of indirect detector (solid line), direct detector with grid (dotted line) and direct detector with trapping layer (dashed line) at an x-ray exposure of 0.1 μR . The electronic noise is assumed to be 1500 e/pixel . The applied avalanche gain is ~ 20 . In order to achieve the gain, the electric fields in the gain regions of indirect detector, direct detector with grid and direct detector with trapping layer are 100.5, 90 and 98 $\text{V}/\mu\text{m}$, respectively. The thicknesses of the gain regions of different detectors are mentioned earlier.

It is observed that the indirect direct shows higher DQE at low spatial frequency compared to the direct detectors. However, at higher frequencies, more than $\sim 2 \text{ mm}^{-1}$, the DQE of the direct detectors becomes higher. The poor DQE performance of indirect detectors at higher frequencies is attributed to the light photon spreading in the CsI layer. Between the direct detectors, the detector with grid shows slightly higher DQE than the detector with trapping layer. It is due to the fact that some fraction of the x-ray generated carriers is trapped in the trapping layer.

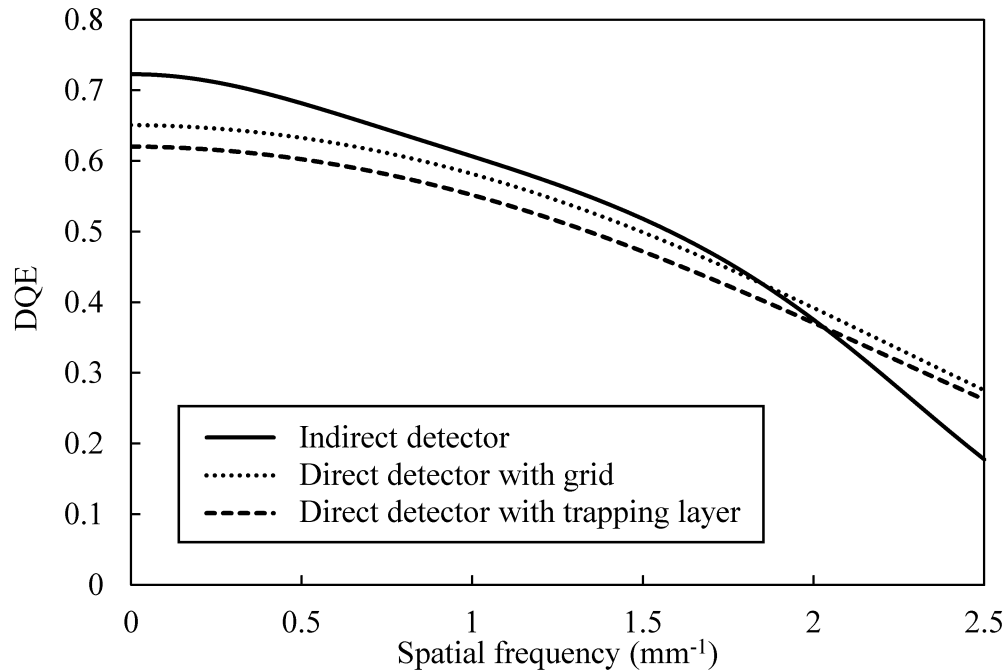


Figure 6.1 DQE(f) of different detectors with avalanche gain for fluoroscopic applications.

DQE(0) is also a performance indicator of a detector. It shows the output signal strength of a detector without considering the spreading of signal. Figure 6.2 shows the effect of avalanche gain on the DQE(0) at different x-ray exposures.

It is evident from the figure that without avalanche gain, the DQE(0) decreases rapidly when the x-ray exposure is decreased. However, when avalanche multiplication is activated, the detectors maintain a high DQE(0) over a long range of exposures. DQE(0) starts decreasing when the exposures goes below 0.01 μ R. Figure 6.2 also illustrates that without avalanche gain, the DQE(0) of direct detector with grid is inferior to that of direct detector with trapping layer. It is because, without avalanche multiplication of the x-ray generated holes, the effect of carrier trapping is more pronounced in the direct detector with grid due to very low weighting potential in the absorption layer.

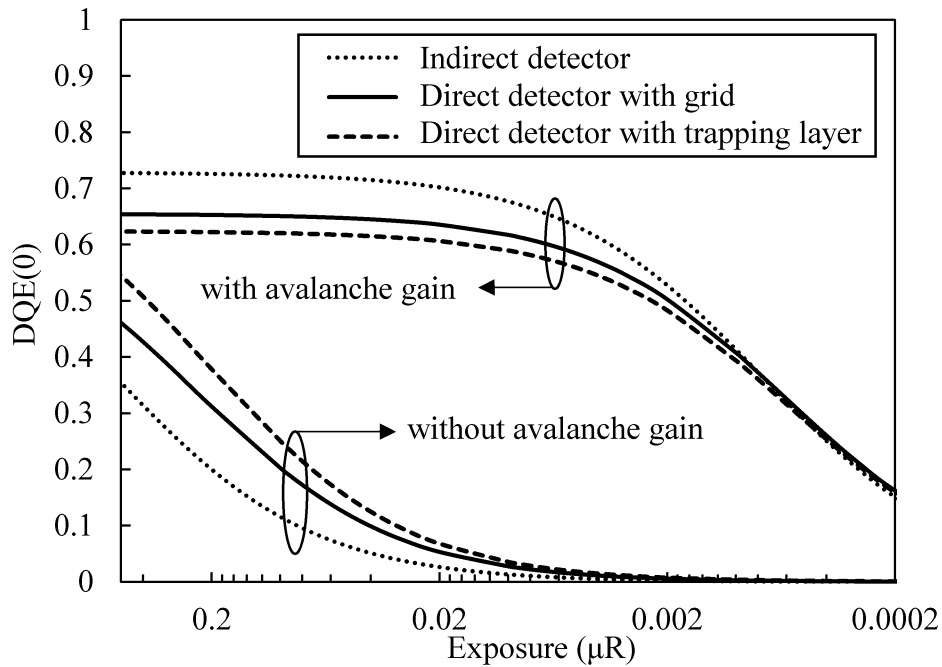


Figure 6.2 DQE(0) of different detectors for fluoroscopic applications as a function of x-ray exposure with and without avalanche gain.

Figure 6.3 shows that the direct detectors perform better than indirect detector in terms of resolution. It is evident that the MTF of indirect detector drops quickly compared to that of direct detectors. At Nyquist frequency ($f_N = 2.5 \text{ mm}^{-1}$), the MTF of indirect direct is 0.081, whereas, the MTFs of direct detector with grid and direct detector with trapping layer are 0.62 and 0.6, respectively. The MTF of direct detector with trapping layer is slightly lower than that of direct detector with grid. It is because, the x-ray generated holes may get trapped in the trapping layer and induce charges in the neighboring pixels. As a result, the trapped holes effect the overall MTF of the detector.

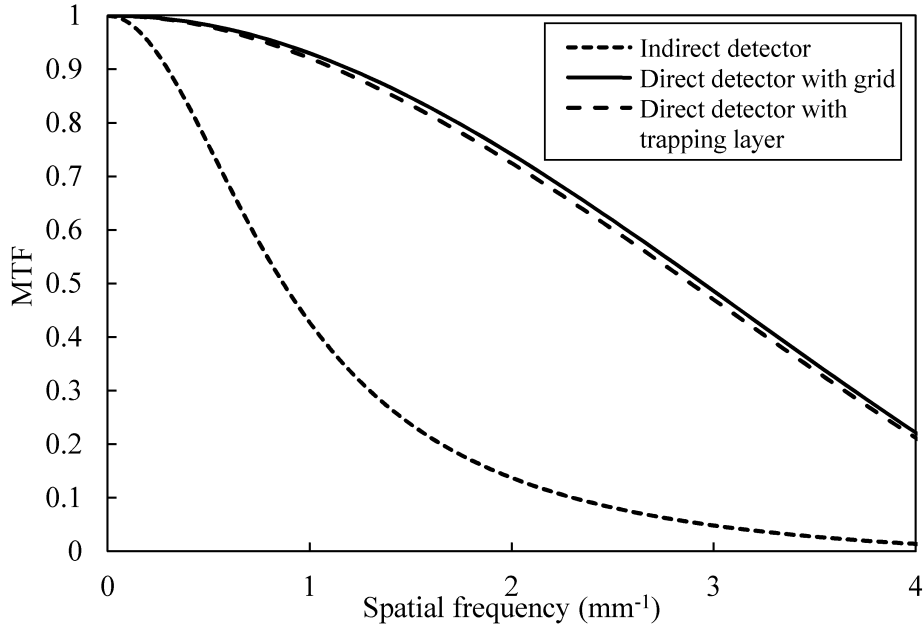


Figure 6.3 MTF of different structures for fluoroscopic application.

6.2 Performance comparison of detectors for tomosynthesis

The operating condition depends on the imaging application. For breast tomosynthesis, a standard mammography energy spectrum (28 kVp with tungsten target and 50 μm rhodium filter) is considered. Therefore, the average x-ray energy becomes 21 keV. The thickness of the absorption layer (i.e., a-Se) in direct detectors is assumed to be 200 μm and the thickness of scintillator (i.e., CsI) in indirect detector is ~ 470 μm . These values of thicknesses ensure a quantum efficiency of ~ 0.97 for all the detectors. The thickness of the rest of the layers are unchanged. The parameter values given in Table 6.2 are used for the following simulations. Unless mentioned otherwise, the values of all parameters are the same as mentioned earlier.

Figure 6.4 shows the $DQE(f)$ comparison between indirect detector (dotted line), direct detector with grid (solid line) and direct detector with trapping layer (dashed line) at an x-ray exposure of 0.41 mR. The electronic noise is kept fixed at 1500 e/pixel. The applied avalanche gain is ~ 10 . In order to achieve the gain, the electric fields in the gain regions of indirect detector, direct detector with grid and direct detector with trapping layer are 98, 88 and 95.5 V/ μm , respectively.

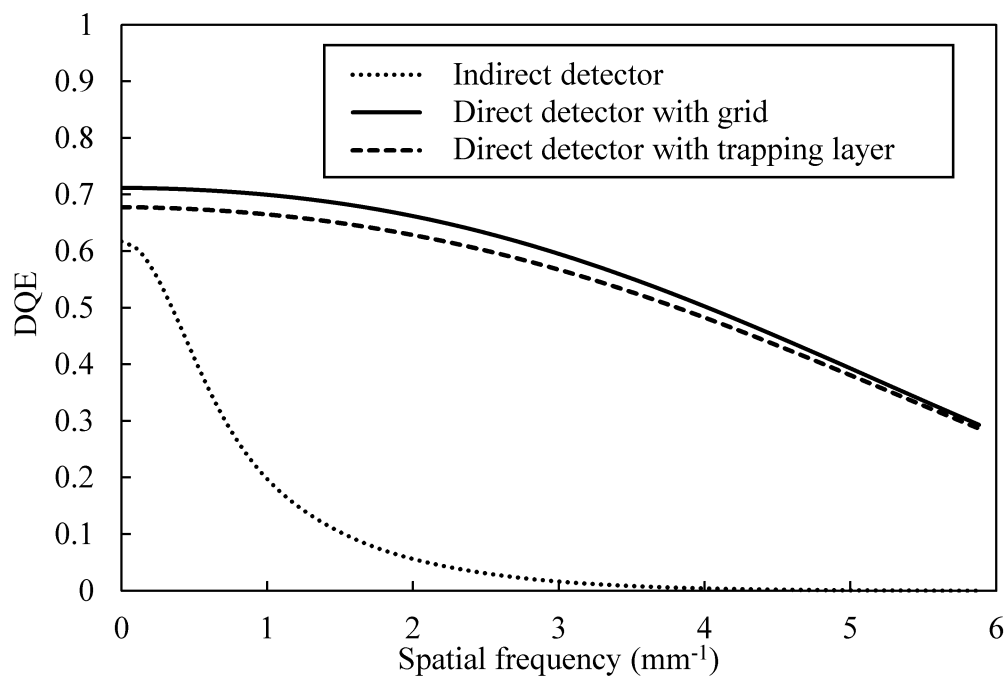


Figure 6.4 $DQE(f)$ of different detectors with avalanche gain for tomosynthesis.

It is evident from the figure that the DQE performance of the direct detectors are superior compared to that of indirect detector. In indirect detector, the DQE at Nyquist frequency ($f_N = 5.88 \text{ mm}^{-1}$) is close to zero. Whereas in case of direct detectors (with grid and with trapping layer), the detective quantum efficiency at Nyquist frequency is ~ 0.29 . However, at lower frequencies, the DQE of direct detector with trapping layer is slightly lower due to carrier trapping in the trapping layer.

Figure 6.5 shows the effect of avalanche gain on the DQE(0) at different x-ray exposures. Without avalanche gain, the DQE(0) decreases rapidly when the x-ray exposure decreases. It is also observed that the DQE(0) of indirect detector remains less than that of direct detectors at different x-ray exposures.

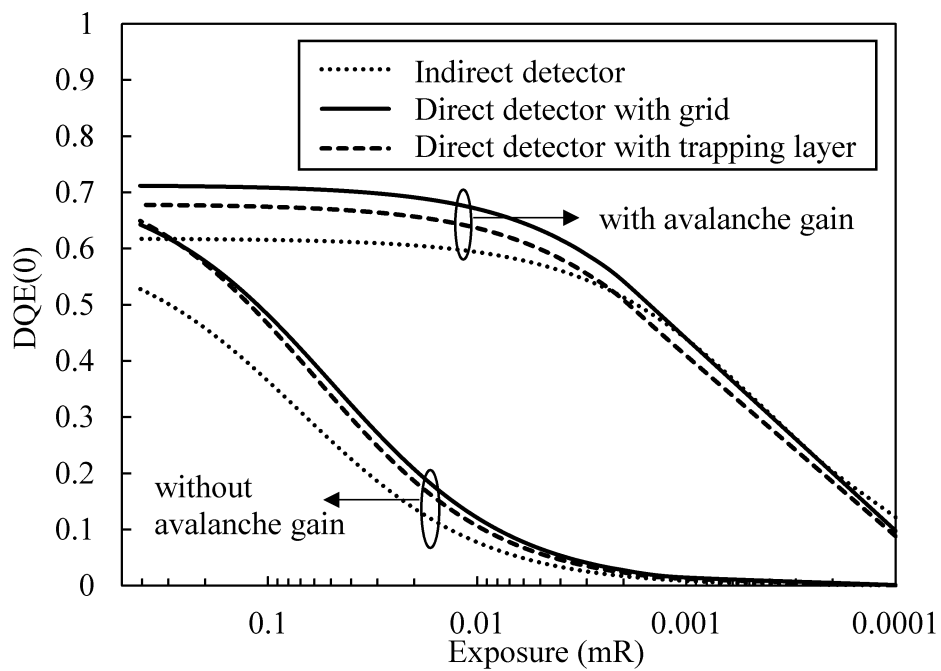


Figure 6.5 DQE(0) of different detectors for tomosynthesis as a function of x-ray exposure with and without avalanche gain.

The detectors shows better performance when a high electric field is applied (initiating avalanche multiplication of charge carriers) across the gain region. The avalanche gain improves the DQE(0) of the detectors at low doses.

Figure 6.6 shows that the MTF performance of the detectors. It shows that the direct detectors perform better than indirect detector in terms of MTF. The MTF of indirect detector drops drastically compared to that of direct detectors.

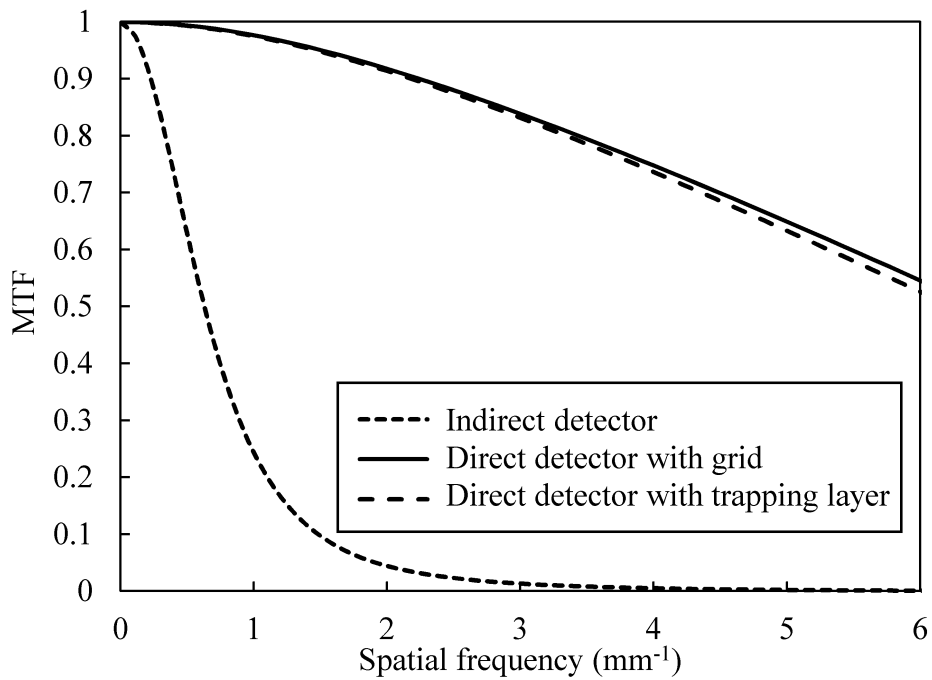


Figure 6.6 MTF of different structures for tomosynthesis

At Nyquist frequency ($f_N = 5.88 \text{ mm}^{-1}$), the MTF of indirect direct is almost zero, whereas, the MTFs of direct detector with grid and direct detector with trapping layer are 0.56 and 0.54, respectively. The MTF of direct detector with trapping layer is slightly lower than that of direct detector with grid. It is due to the fact that the trapped holes in the trapping layer degrades the resolution of the direct detector with trapping layer.

6.3 Summary

The developed models for different x-ray detector structures, namely, a) indirect conversion avalanche x-ray detector, b) direct conversion avalanche x-ray detector with grid electrode, and c) direct-conversion multilayer avalanche x-ray detector with trapping layer, are used to compare their imaging performance under the conditions used in fluoroscopy and tomosynthesis. In fluoroscopic applications, the indirect conversion avalanche detector shows higher DQE in low spatial frequencies (less than 2 mm^{-1}) than the direct conversion avalanche detectors. However, the direct conversion avalanche detectors show better DQE performance than the indirect conversion avalanche detectors in the higher frequencies. Due to avalanche multiplication, the detectors maintain a high DQE(0) over a long range of exposures. DQE(0) starts decreasing when the exposures goes below $0.01 \mu\text{R}$ when the electronic noise is assumed to be 1500 e/pixel. On the other hand, in tomosynthesis, the DQE performance of the direct conversion avalanche detectors are superior compared to that of indirect conversion avalanche detector. In indirect detector, the DQE at Nyquist frequency approaches to zero. It is also shown that the MTF of indirect detector in both applications (i.e., tomosynthesis and fluoroscopy) drops drastically at higher spatial frequency whereas the MTF of direct conversion detectors remain high

CHAPTER 7

Conclusions, contributions and future Work

7.1 Conclusions

The commercial AMFPIs are not quantum noise limited at low exposures due to the electronic noise originated from the readout circuitry. In this work, physics-based models have been developed to study the feasibility of avalanche gain to overcome the adverse effect of electronic noise in both direct and indirect conversion detectors. The work also includes a novel device structure for a-Se based direct conversion avalanche x-ray detector.

This work has mainly focused on the impact ionization of charge carriers in a-Se. Among other photoconductors, a-Se is chosen because it is an established material for x-ray detection. Moreover, avalanche multiplication of charge carrier in a-Se is currently used in highly sensitive cameras. Therefore, introducing avalanche multiplication in AMFPIs can increase the signal gain and hence the performance at low x-ray exposures.

The developed models for direct and indirect conversion avalanche detectors calculate the detective quantum efficiency, modulation transfer function, transient electric field profile and dark current density considering charge transport properties of the photoconductor, depth dependent light spreading in the scintillator, operating condition and detector geometry and design. The models are also used to compare the imaging performance of different detectors. The following subsections summarize the contribution and key findings presented in this research work.

7.1.1 Effect of depth dependent x-ray absorption in indirect conversion avalanche detector

In indirect conversion detector, the spreading of light photons depends on the depth of x-ray absorption, which is known as Lubberts effect. The exponential x-ray absorption in the scintillator or phosphor determines the signal and noise transfer in indirect conversion detector. Therefore, the normalized MTF is not just proportional to the normalized NPS at the output of the scintillator. In this thesis, a cascaded linear-system model has been developed by considering Lubberts effect in x-ray absorbing scintillator (i.e., CsI). The required avalanche gain in a-Se based photodiode to overcome the effect of electronic noise and depth dependent x-ray absorption (Lubberts effect) is also calculated. The model includes scattering due to *K*-fluorescence reabsorption.

It is found that the effect of depth dependent x-ray absorption is more pronounced in thicker detectors. It is observed that, at the Nyquist frequency (2.5 mm^{-1}), the presampling MTF of CsI deteriorates from 0.75 to 0.1 due to Lubberts effect in a CsI layer having thickness of 0.6 mm. At

the same frequency, the DQE drops from 0.037 to 0.01 at a field of 60 V/ μm due to Lubberts effect. The Lubberts fraction decreases with increasing the field thereafter. The avalanche gain enhances the signal strength and improves the frequency dependent $\text{DQE}(f)$ by overcoming the Lubberts effect and as well as the effect of the electronic noise. It is observed that an avalanche gain of 45 is sufficient to overcome the effect of electronic noise of 1500 e/pixel.

7.1.2 Carrier trapping in a-Se based direct conversion avalanche detector

A fraction of the x-ray generated charge carriers is trapped in the absorption layer of a-Se based direct conversion avalanche detectors with grid electrode. As a result, the charge collection efficiency reduces. However, due to certain mesh aperture, a trapped carrier induces a fraction of its total charge. This fraction depends on the existing weighting potential across the detector. The charging carrier trapping not effects the charge collection efficiency, but also increases the blurring in the final x-ray images. It is because the trapped carriers induce charges to the neighboring pixels. Therefore, it is necessary to consider the effect of carrier trapping in a-Se based direct conversion avalanche detectors.

A cascaded linear system model is developed to determine the detective quantum efficiency (DQE) considering trapping of charge carriers in the absorption layer of amorphous selenium multilayer direct conversion avalanche detector. This model considers the effects of charge carrier trapping and reabsorption of K -fluorescent x-rays on the frequency-dependent $\text{DQE}(f)$. A 2-D simulation is

performed to calculate the actual weighting potential in the absorption layer, which is used to calculate the amount of collected charge. It is observed that the $DQE(f=0)$ reduces from 0.46 to 0.38 due to charge carrier trapping in the absorption layer having a thickness of 1000 μm when the electronic noise is 1500 electrons per pixel. The avalanche gain enhances the signal strength and improves the frequency dependent $DQE(f)$ by overcoming the effect of carrier trapping and as well as the effect of the electronic noise. The simulations suggest that avalanche gain of 35 and 20 are required to overcome the effect of the electronic noise of 1500 and 700 electrons per pixel, respectively.

7.1.3 Novel structure for a-Se based direct conversion avalanche detector

The image resolution in terms of MTF of indirect conversion detectors is affected by the Lubberts effect due to omni-directional light spreading in x-ray absorbing scintillators (e.g., CsI). Whereas, in a-Se based direct conversion detectors, the x-ray to light conversion step is missing and therefore these detectors show a better performance in terms of resolution. However, large EHP creation energy in a-Se based direct conversion detectors, makes these detectors vulnerable to electronic noise. In this thesis, it has been shown that the avalanche gain can overcome the effect of electronic noise in direct conversion detectors. The direct conversion avalanche detectors that are mentioned in the literature use grid electrodes to reduce the avalanche gain fluctuation. Implementing and operating this kind of grid-based structures are not only difficult, but also costly. Therefore, a simple structure for direct conversion avalanche detector with minimum gain fluctuation will help to increase the image quality even at low doses (e.g., doses used in tomosynthesis and fluoroscopy)

A novel amorphous selenium (a-Se) avalanche detector structure for low dose direct-conversion flat-panel x-ray detector is proposed. The proposed structure contains blocking layers to reduce carrier injection from metal electrodes and hole trapping layer to separate x-ray absorption layer from avalanche gain region. The trapping layer enhances the electric field in the gain region to initiate avalanche multiplication of charge carriers which improves the signal strength. The feasibility of the structure for avalanche gain with negligible avalanche noise is studied by using the Semiconductor Module of COMSOL Multiphysics together with a cascaded linear system. The model considers carrier injection from electrodes and charge carrier transport through various layers of multilayer a-Se structure in order to analyze the transient and steady state electric field distribution across the detector. It has been shown that average electric fields of $\sim 10.8 \text{ V}/\mu\text{m}$ and $\sim 94 \text{ V}/\mu\text{m}$ can be achieved in the absorption and gain regions, respectively. Although the dark current is higher than previously reported values, it is still in the same order of magnitude and therefore does not significantly increase the electronic noise. A cascaded linear system model that includes reabsorption of *K*-fluorescent x-rays and avalanche multiplication of charge carrier is used to calculate the frequency-dependent detective quantum efficiency, $\text{DQE}(f)$ of the proposed structure. The avalanche gain enhances the signal strength and improves the $\text{DQE}(f)$ by overcoming the effect of electronic noise. The structure is applied for breast tomosynthesis and observed that the proposed structure offers the required avalanche gain to ensure quantum noise limited operation at reduced exposures.

7.1.4 Performance comparison of different detectors

The relative performance of the a-Se avalanche detector structures (direct and indirect conversion) will influence their clinical effectiveness. Therefore, the performances of the detector structures mentioned in this thesis are assessed and compared for different x-ray imaging modalities (i.e., tomosynthesis and fluoroscopy).

In fluoroscopic applications, when the spatial frequency is less than $\sim 2 \text{ mm}^{-1}$, the DQE performance of indirect conversion avalanche detector is higher compared to that of the direct conversion avalanche detectors. With avalanche gain and an electronic noise of 1500 e/pixel, the DQE(0) of indirect conversion avalanche detector, direct conversion avalanche detector with grid electrode and with trapping layer are 0.72, 0.65 and 0.62 respectively when the dose is kept fixed at $0.1 \mu\text{R}$. In tomosynthesis, the DQE of direct conversion avalanche detectors at all relevant frequencies remain higher compared to that of indirect conversion avalanche detector. The MTF at Nyquist frequency ($f_N = 5.88 \text{ mm}^{-1}$), the MTF of indirect direct is almost zero, whereas, the MTFs of direct detector with grid and direct detector with trapping layer are 0.56 and 0.54, respectively.

7.2 Contributions

A cascaded linear-system model is proposed to find the required electric field to overcome the effect of electronic noise and depth dependent x-ray absorption (Lubberts effect) in amorphous

selenium based indirect conversion avalanche detectors. The model shows good agreement with the published experimental results compared to the previously published models. This work (chapter 3) has been published in journal [88] and conference papers.

- ❖ S. M. Arnab and M. Z. Kabir, “Impact of Lubberts Effect on Amorphous Selenium Indirect Conversion Avalanche Detector for Medical X-Ray Imaging,” *IEEE Transactions on Radiation and Plasma Medical Sciences*, 1(3), 221-228, 2017.
- ❖ S. M. Arnab and M. Z. Kabir, “A comprehensive study on spatial frequency response of CsI based x-ray detectors using linear cascaded system with depth-dependent noise”, 7th International Conference on Optical, Optoelectronic and Photonic Materials and Applications 2016, Montreal, Canada.

A cascaded linear system model is developed to determine the detective quantum efficiency (DQE) considering trapping of charge carriers in the absorption layer of an amorphous selenium multilayer direct conversion avalanche detector. The effect of carrier trapping in charge collection and image blurring is calculated by computing the actual weighting potential across the device structure. The optimal design parameters and operational condition for a-Se based direct-conversion multilayer avalanche x-ray detectors are described. This work (chapter 4) has been published in journal [115] and conference papers.

- ❖ S. M. Arnab and M. Z. Kabir, "Impact of charge carrier trapping on amorphous selenium direct conversion avalanche x-ray detectors," *J. Appl. Phys.*, vol. 122, no. 13, pp. 134502-134508, 2017.

- ❖ S. M. Arnab and M. Z. Kabir, “Effects of carrier trapping on direct conversion amorphous selenium avalanche detector for x-ray Imaging”, 18th Canadian Semiconductor Science and Technology Conference 2017, Waterloo, Canada.

A novel amorphous selenium (a-Se) avalanche detector structure for low dose direct-conversion flat-panel x-ray detector is proposed. The proposed structure has a simple structure compared to the previously proposed direct conversion avalanche detectors. The feasibility of the structure for avalanche gain with negligible avalanche noise is studied by using the Semiconductor Module of COMSOL Multiphysics together with a cascaded linear system. The proposed structure shows better performance in terms of DQE compared to the commercially available direct conversion detectors for low dose applications (e.g., tomosynthesis). This work (chapter 5) has been published in journal [131].

- ❖ S. M. Arnab and M. Z. Kabir, “A novel amorphous selenium direct conversion avalanche detector structure for low dose medical x-ray imaging”, IEEE Transactions on Radiation and Plasma Medical Sciences – accepted, 2019

7.3 Future work

A numerical model is developed to estimate the electric field and dark current of the proposed direct conversion avalanche detector. The model considers a uniform trap distribution in different layers, namely, blocking layers and trapping layers. However, the model does not consider the effects of interface trap density. Therefore, the model can be updated by considering trap densities at the interfaces between different layers.

The dark current mainly depends on the carrier injection, however, the thermal generation rate can increase exponentially with field due to Poole–Frenkel or thermally assisted tunneling. Therefore, the developed numerical model can be improved by incorporating the effects of thermal generation on dark current of direct conversion avalanche detectors.

It is required to maintain a high frame rate in x-ray imaging modalities, such as, fluoroscopy and tomosynthesis. Therefore, the effects of lag (residual signal) and ghost (change of sensitivity) on the imaging performance are crucial for these modalities. The trapped charges in the trapping layer may play a vital role in the imaging performance of direct conversion avalanche detector with trapping layer in terms of lag and ghost. A model can be developed to calculate the lag and ghost in the proposed structure.

REFERENCES

- [1] M. J. Yaffe, J. G. Mainprize, and R. A. Jong, "Technical developments in mammography," *Health Physics*, vol. 95, no. 5, pp. 599-611, 2008.
- [2] M. Uffmann and C. Schaefer-Prokop, "Digital radiography: the balance between image quality and required radiation dose," *European Journal of Radiology*, vol. 72, no. 2, pp. 202-208, 2009.
- [3] D. Oborska-Kumaszyńska and S. Wiśniewska-Kubka, "Analog and digital systems of imaging in roentgenodiagnosics," *Polish Journal of Radiology*, vol. 75, no. 2, pp. 73-81, 2010.
- [4] P. J. Allisy-Roberts and J. Williams, *Farr's physics for medical imaging*. St Louis, MO: Saunders, 2007.
- [5] A. R. Cowen, A. G. Davies, and S. M. Kengyelics, "Advances in computed radiography systems and their physical imaging characteristics," *Clinical Radiology* vol. 62, no. 12, pp. 1132-1141, 2007.
- [6] S. Kasap, J. B. Frey, G. Belev, O. Tousignant, H. Mani, J. Greenspan, L. Laperriere et al., "Amorphous and polycrystalline photoconductors for direct conversion flat panel x-ray image sensors," *Sensors*, vol. 11, no. 5, pp. 5112-5157, 2011.
- [7] N. Shah, N. Bansal, and A. Logani, "Recent advances in imaging technologies in dentistry," *World journal of Radiology*, vol. 6, no. 10, pp. 794-807, 2014.
- [8] M. Korner, C. H. Weber, S. Wirth, K-J. Pfeifer, M. F. Reiser, and M. Treitl, "Advances in digital radiography: physical principles and system overview," *Radiographics*, vol. 27, no. 3, pp. 675-686, 2007.
- [9] D. C. Hunt, O. Tousignant, and J. A. Rowlands, "Evaluation of the imaging properties of an amorphous selenium-based flat panel detector for digital fluoroscopy," *Medical Physics*, vol. 31, no. 5, pp. 1166-1175, 2004.
- [10] B. Ren, C. Ruth, J. Stein, A. Smith, I. Shaw, and Z. Jing, "Design and performance of the prototype full field breast tomosynthesis system with selenium based flat panel detector," In *Medical Imaging 2005: Physics of Medical Imaging*, vol. 5745, no. pp. 550-561, 2005.

- [11] M. Bissonnette, M. Hansroul, E. Masson, S. Savard, S. Cadieux, P. Warmoes, D. Gravel et al., "Digital breast tomosynthesis using an amorphous selenium flat panel detector," In *Medical Imaging 2005: Physics of Medical Imaging*, vol. 5745, pp. 529-540, 2005.
- [12] R. S. Livingstone, D. Chase, A. Varghese, P. V. George, and O. K. George, "Transition from image intensifier to flat panel detector in interventional cardiology: impact of radiation dose," *Journal of Medical Physics/Association of Medical Physicists of India*, vol. 40, no. 1, pp. 24-28, 2015.
- [13] R. K. Swank, "Absorption and noise in x-ray phosphors," *Journal of Applied Physics*, vol. 44, no. 9, pp. 4199-4203, 1973.
- [14] C. E. Dick and J. W. Motz, "Image information transfer properties of x-ray fluorescent screens," *Medical Physics*, vol. 8, no. 3, pp. 337-346, 1981.
- [15] J. H. Harris, W. H. Harris, and R. A. Novelline, *The radiology of emergency medicine*, Philadelphia: Lippincott Williams & Wilkins, 2000.
- [16] M-Y, Jeung, A. Gangi, B. Gasser, C. Vasilescu, G. Massard, J-M, Wihlm, and C. Roy, "Imaging of chest wall disorders," *Radiographics* vol. 19, no. 3, pp. 617-637, 1999.
- [17] K. K. Amrami and R. A. Berger, "Radiology corner: review of plain radiographs," *Journal of Hand Surgery*, vol. 5, no. 1, pp. 4-7, 2005.
- [18] M. J. Yaffe and J. A. Rowlands, "X-ray detectors for digital radiography," *Physics in Medicine & Biology*, vol. 42, no. 1, pp. 1-39, 1997.
- [19] S. Vecchio, A. Albanese, P. Vignoli and A. Taibi. "A novel approach to digital breast tomosynthesis for simultaneous acquisition of 2D and 3D images." *European Radiology*, vol. 21, no. 6, pp. 1207-1213, 2011.
- [20] M. L. Zuley, B. Guo, V. J. Catullo, D. M. Chough, A. E. Kelly, A. H. Lu, G. Y. Rathfon et al., "Comparison of two-dimensional synthesized mammograms versus original digital mammograms alone and in combination with tomosynthesis images," *Radiology*, vol. 271, no. 3, pp. 664-671, 2014.
- [21] M. Kitagawa and Y. Kouno, "Development of x-ray fluoroscopy devices," In *Respiratory endoscopy*. Singapore: Springer, 2017.
- [22] L. Lança and A. Silva, "Digital radiography detectors: a technical overview," In *Digital imaging systems for plain radiography*, New York: Springer, 2013.

- [23] N. Matsuura, W. Zhao, Z. Huang, and J. A. Rowlands, "Digital radiology using active matrix readout: Amplified pixel detector array for fluoroscopy," *Medical Physics*, vol. 26, no. 5, pp. 672-681, 1999.
- [24] S. O. Kasap, and J. A. Rowlands, "Direct-conversion flat-panel x-ray image detectors," *IEE Proceedings-Circuits, Devices and Systems*, vol. 149, no. 2, pp. 85-96, 2002.
- [25] J. Yorkston, "Recent developments in digital radiography detectors," In *Nuclear Instruments and Methods in Physics Research Section A: Accelerators, Spectrometers, Detectors and Associated Equipment*, vol. 580, no. 2, pp. 974-985, 2007.
- [26] D. L. Y. Lee, K. Lawrence, Cheung, and L. S. Jeromin, "New digital detector for projection radiography," In *Medical Imaging 1995: Physics of Medical Imaging*, vol. 2432, pp. 237-249, 1995.
- [27] S. O. Kasap, M. Z. Kabir, and J. A. Rowlands, "Recent advances in x-ray photoconductors for direct conversion x-ray image detectors," *Current Applied Physics*, vol. 6, no. 3, pp. 288-292, 2006.
- [28] R. D. Gould, S. Kasap, and A. K. Ray, "Thin Films," In *Springer handbook of electronic and photonic materials*, Cham: Springer, 2017.
- [29] C. Michail, I. Valais, I. Seferis, N. Kalyvas, G. Fountos, and I. Kandarakis, "Experimental measurement of a high resolution CMOS detector coupled to CsI scintillators under x-ray radiation," *Radiation Measurements*, vol. 74, pp. 39-46, 2015.
- [30] D. M. Schlosser, M. Huth, R. Hartmann, A. Abboud, S. Send, T. Conka-Nurdan, M. Shokr, U. Pietsch, and L. Strüder, "Direct and indirect signal detection of 122 keV photons with a novel detector combining a pnCCD and a CsI (Tl) scintillator," *Nuclear Instruments and Methods in Physics Research Section A: Accelerators, Spectrometers, Detectors and Associated Equipment*, vol. 805, pp. 55-62, 2016.
- [31] T. Jing, C. A. Goodman, J. Drewery, G. Cho, W. S. Hong, H. Lee, S. N. Kaplan, V. Perez-Mendez, and D. Wildermuth, "Detection of charged particles and x-rays by scintillator layers coupled to amorphous silicon photodiode arrays," *Nuclear Instruments and Methods in Physics Research Section A: Accelerators, Spectrometers, Detectors and Associated Equipment*, vol. 368, no. 3, pp. 757-764, 1996.
- [32] B. A. Schueler, "The AAPM/RSNA physics tutorial for residents general overview of fluoroscopic imaging." *Radiographics*, vol. 20, no. 4, pp. 1115-1126, 2000.
- [33] J. Jacobs and H. Berger, "Large-area photoconductive x-ray pickup-tube performance," *Electrical Engineering*. vol. 75, no. 2, pp. 158-161, 1956.

- [34] R. Luhta, and J. A. Rowlands, "Feasibility of a large area x-ray sensitive vidicon for medical fluoroscopy: Signal and noise factors," *Medical Physics*, vol. 24, no. 5, pp. 609-620, 1997.
- [35] R. Hofstetter, M. Slomczykowski, M. Sati, and L-P. Nolte, "Fluoroscopy as an imaging means for computer-assisted surgical navigation," *Computer Aided Surgery*, vol. 4, no. 2, pp. 65-76, 1999.
- [36] A. Trianni, "Fluoroscopy: physics and technology," In *Handbook of X-ray Imaging: Physics and Technology*, Florida: CRC press, 2017.
- [37] D. Soimu, B. Cristian and N. Pallikarakis, "A novel approach for distortion correction for X-ray image intensifiers," *Computerized Medical Imaging and Graphics*, vol. 27, no. 1, pp. 79-85, 2003.
- [38] J. A. Rowlands and J. Yorkston, *Flat panel detectors for digital radiography*. Handbook of medical imaging, Washington: SPIE Press, 2000.
- [39] U. W. Schiebel, N. Conrads, N. Jung, M. Weibrecht, H. K. Wiczorek, T. T. Zaengel, M. J. Powell, I. D. French, and C. Glasse, "Fluoroscopic x-ray imaging with amorphous silicon thin-film arrays," *Medical Imaging 1994: Physics of Medical Imaging*, vol. 2163, pp. 129-140, 1994.
- [40] J. Chabbal, C. Chaussat, T. Ducourant, L. Fritsch, J. Michailos, V. Spinnler, G. Vieux et al., "Amorphous silicon x-ray image sensor," *Medical Imaging 1996: Physics of Medical Imaging*, vol. 2708, pp. 499-510, 1996.
- [41] N. Jung, P. L. Alving, F. Busse, N. Conrads, H. J. Meulenbrugge, W. Ruetten, U. W. Schiebel, M. Weibrecht, and H. K. Wiczorek, "Dynamic x-ray imaging system based on an amorphous silicon thin-film array," *Medical Imaging 1998: Physics of Medical Imaging*, vol. 3336, pp. 396-407, 1998.
- [42] W. Zhao, I. Blevis, S. Germann, J. A. Rowlands, D. Waechter, and Z. Huang, "Digital radiology using active matrix readout of amorphous selenium: Construction and evaluation of a prototype real-time detector," *Medical Physics*, vol. 24, no. 12, pp. 1834-1843, 1997.
- [43] T. Graeve and G. P. Weckler, "High-resolution CMOS imaging detector," *Medical Imaging 2001: Physics of Medical Imaging*, vol. 4320, pp. 68-76, 2001.
- [44] M. Esposito, T. Anaxagoras, A. C. Konstantinidis, Y. Zheng, R. D. Speller, P. M. Evans, N. M. Allinson, and K. Wells, "Performance of a novel wafer scale CMOS active pixel sensor for bio-medical imaging," *Physics in Medicine & Biology*, vol. 59, no. 13, pp. 3533-3554, 2014.
- [45] M. Esposito, T. Anaxagoras, A. Fant, K. Wells, A. Konstantinidis, J. P. F. Osmond, P. M. Evans, R. D. Speller, and N. M. Allinson, "DynAMITE: a wafer scale sensor for biomedical applications," *Journal of Instrumentation*, vol. 6, no. 12, pp. C12064, 2011.

- [46] S. E. Bohndiek, A. Blue, J. Cabello, A. T. Clark, N. Guerrini, P. M. Evans, E. J. Harris et al., "Characterization and testing of LAS: a prototypelarge area sensor with performance characteristics suitable for medical imaging applications," *IEEE Transactions on Nuclear Science*, vol. 56, no. 5, pp. 2938-2946, 2009.
- [47] A. C. Konstantinidis, M. B. Szafraniec, L. Rigon, G. Tromba, D. Dreossi, N. Sodini, P. F. Liaparinos et al., "X-ray performance evaluation of the Dexela CMOS APS x-ray detector using monochromatic synchrotron radiation in the mammographic energy range." *IEEE Transactions on Nuclear Science*, vol. 60, no. 5, pp. 3969-3980, 2013.
- [48] M. Z. Kabir and S. Kasap. "Photoconductors for x-ray image detectors," In *Springer Handbook of Electronic and Photonic Materials*, Cham: Springer, 2017.
- [49] Dance, D. R., S. Christofides, A. D. A. Maidment, I. D. McLean, and K. H. Ng. "Diagnostic radiology physics." *International Atomic Energy Agency* (2014).
- [50] S. A. Mahmood and M. Z. Kabir, "Dark current mechanisms in stabilized amorphous selenium based *n-i* detectors for x-ray imaging applications," *Journal of Vacuum Science & Technology A: Vacuum, Surfaces, and Films*, vol. 29, no. 3, pp. 031603-6, 2011.
- [51] G. Zentai, L. Partain, R. Pavlyuchkova, C. Proano, B. N. Breen, A. Taieb, O. Dagan, M. Schieber, H. Gilboa, and Jerry Thomas, "Mercuric iodide medical imagers for low-exposure radiography and fluoroscopy," *Medical Imaging 2004: Physics of Medical Imaging*, vol. 5368, pp. 200-210, 2004.
- [52] Z. Su, L. E. Antonuk, Y. El-Mohri, L. Hu, H. Du, A. Sawant, Y. Li, Y. Wang, J. Yamamoto, and Q. Zhao, "Systematic investigation of the signal properties of polycrystalline HgI₂ detectors under mammographic, radiographic, fluoroscopic and radiotherapy irradiation conditions," *Physics in Medicine & Biology*, vol. 50, no. 12, pp. 2907-2928, 2005.
- [53] X. Zhu, H. Sun, D. Yang, J. Yang, X. Li, and X. Gao, "Fabrication and characterization of x-ray array detectors based on polycrystalline PbI₂ thick films," *Journal of Materials Science: Materials in Electronics*, vol. 25, no. 8, pp. 3337-3343, 2014.
- [54] M. Simon, R. A. Ford, A. R. Franklin, S. P. Grabowski, B. Menser, G. Much, A. Nascetti, M. Overdick, M. J. Powell, and D. U. Wiechert, "PbO as direct conversion x-ray detector material," *Medical Imaging 2004: Physics of Medical Imaging*, vol. 5368, pp. 188-199, 2004.
- [55] J. Berashevich, O. Semeniuk, O. Rubel, J. A. Rowlands, and A. Reznik, "Lead monoxide α -PbO: electronic properties and point defect formation," *Journal of Physics: Condensed Matter*, vol. 25, no. 7, pp. 075803-7, 2013.

- [56] S. Tokuda, H. Kishihara, S. Adachi, and T. Sato, "Preparation and characterization of polycrystalline CdZnTe films for large-area, high-sensitivity X-ray detectors," *Journal of Materials Science: Materials in Electronics*, vol. 15, no. 1, pp. 1-8, 2004.
- [57] A. Reznik, S. D. Baranovskii, O. Rubel, G. Juska, S. O. Kasap, Y. Ohkawa, K. Tanioka, and J. A. Rowlands, "Avalanche multiplication phenomenon in amorphous semiconductors: Amorphous selenium versus hydrogenated amorphous silicon," *Journal of Applied Physics*, vol. 102, no. 5, pp. 053711-4, 2007.
- [58] K. Kikuchi, Y. Ohkawa, K. Miyakawa, T. Matsubara, K. Tanioka, M. Kubota, and N. Egami, "Hole-blocking mechanism in high-gain avalanche rushing amorphous photoconductor (HARP) film," *Physica Status Solidi (c)*, vol. 8, no. 9, pp. 2800-2803, 2011.
- [59] S. Abbaszadeh, A. Tari, W. S. Wong, and K. S. Karim, "Enhanced dark current suppression of amorphous selenium detector with use of IGZO hole blocking layer," *IEEE Transactions on Electron Devices*, vol. 61, no. 9, pp. 3355-3357, 2014.
- [60] L. E. Antonuk, K-W. Jee, Y. El-Mohri, M. Maolinbay, S. Nassif, X. Rong, Q. Zhao, J. H. Siewerdsen, R. A. Street, and K. S. Shah, "Strategies to improve the signal and noise performance of active matrix, flat-panel imagers for diagnostic x-ray applications," *Medical Physics*, vol. 27, no. 1, pp. 289-306, 2000.
- [61] Y. Yatsu, Y. Kuramoto, J. Kataoka, J. Kotoku, T. Saito, T. Ikagawa, R. Sato, N. Kawai, S. Kishimoto, K. Mori, T. Kamae, Y. Ishikawae, and N. Kawabatae, "Study of avalanche photodiodes for soft x-ray detection below 20 keV." *Nuclear Instruments and Methods in Physics Research Section A: Accelerators, Spectrometers, Detectors and Associated Equipment*, vol. 564, no. 1, pp. 134-143, 2006.
- [62] K. Iniewski and T. Astill. "Semiconductor sensors for direct x-ray conversion," In *Sensors for Diagnostics and Monitoring*, New York: CRC Press, 2018.
- [63] W. Zhao, D. C. Hunt, K. Tanioka, and J. A. Rowlands, "Indirect flat-panel detector with avalanche gain," *Medical Imaging 2004: Physics of Medical Imaging*, vol. 5368, pp. 150-161, 2004.
- [64] F. E. Zink, "X-ray tubes," *Radiographics*, vol. 17, no. 5, pp. 1259-1268, 1997.
- [65] S. Kasap, *Optoelectronics and Photonics: Principles and Practices*, India: Pearson Education, 2009.
- [66] J. M. Boone, "X-ray production, interaction, and detection in diagnostic imaging," In *Handbook of Medical Imaging*, Washington: SPIE Press, 2000.

- [67] Physical Reference Data, NIST, 2016. [Online]. Available: <https://physics.nist.gov/PhysRefData/>.
- [68] G. F. Knoll, *Radiation Detection and Measurement*, New York: John Wiley and Sons, 2000.
- [69] N. Hijazi, D. Panneerselvam, and M. Z. Kabir, "Electron–hole pair creation energy in amorphous selenium for high energy photon excitation," *Journal of Materials Science: Materials in Electronics*, vol. 29, no. 1, pp. 486-490, 2018.
- [70] I. M. Blevis, D. C. Hunt, and J. A. Rowlands, "Measurement of x-ray photogeneration in amorphous selenium," *Journal of Applied Physics*, vol. 85, no. 11, pp. 7958-7963, 1999.
- [71] D. Mah, J. A. Rowlands, and J. Alan Rawlinson, "Sensitivity of amorphous selenium to x rays from 40 kVp to 18 MV: Measurements and implications for portal imaging," *Medical Physics*, vol. 25, no. 4, pp. 444-456, 1998.
- [72] O. Bubon, K. Jandieri, S. D. Baranovskii, S. O. Kasap, and A. Reznik, "Columnar recombination for X-ray generated electron-holes in amorphous selenium and its significance in a-Se x-ray detectors," *Journal of Applied Physics*, vol. 119, no. 12, pp. 124511-8, 2016.
- [73] S. O. Kasap, "X-ray sensitivity of photoconductors: application to stabilized a-Se," *Journal of Physics D: Applied Physics*, vol. 33, no. 21, pp. 2853-2865, 2000.
- [74] M. J. Yaffe, "Digital mammography," In *Handbook of Medical Imaging*, Washington: SPIE Press, 2000.
- [75] N. Hijazi and M. Z. Kabir, "Mechanisms of temperature-and field-dependent effective drift mobilities and impact ionization coefficients in amorphous selenium," *Canadian Journal of Physics*, vol. 93, no. 11, pp. 1407-1412, 2015.
- [76] O. Rubel, A. Potvin, and D. Laughton, "Generalized lucky-drift model for impact ionization in semiconductors with disorder," *Journal of Physics: Condensed Matter*, vol. 23, no. 5, pp. 055802(7pg), 2011.
- [77] W. Shockley, "Currents to conductors induced by a moving point charge," *Journal of Applied Physics*, vol. 9, no. 10, pp. 635-636, 1938.
- [78] Z. He, "Review of the Shockley–Ramo theorem and its application in semiconductor gamma-ray detectors," *Nuclear Instruments and Methods in Physics Research Section A: Accelerators, Spectrometers, Detectors and Associated Equipment*, vol. 463, no. 1-2, pp. 250-267, 2001.
- [79] T. H. Wilmshurst, *Signal recovery from noise in electronic instrumentation*, New York: CRC Press, 1990.

- [80] H. G. E. Beck and W. P. Spruit. "1/f noise in the variance of Johnson noise." *Journal of Applied Physics*, vol. 49, no. 6, pp. 3384-3385, 1978.
- [81] J. B. Frey, G. Belev, O. Tousignant, H. Mani, L. Laperriere, and S. O. Kasap, "Dark current in multilayer stabilized amorphous selenium based photoconductive x-ray detectors," *Journal of Applied Physics*, vol. 112, no. 1, pp. 014502-8, 2012.
- [82] M. Z. Kabir, "Dark current mechanisms in amorphous selenium-based photoconductive detectors: an overview and re-examination," *Journal of Materials Science: Materials in Electronics*, vol. 26, no.7, pp. 4659-4667, 2015.
- [83] H. H. Barrett and W. Swindell, *Radiological imaging: the theory of image formation, detection, and processing*, San Diego: Academic Press, 1996.
- [84] D. C. Hunt, O. Tousignant, Y. Demers, L. Laperriere, and J. A. Rowlands, "Imaging performance of an amorphous selenium flat-panel detector for digital fluoroscopy," *Medical Imaging 2003: Physics of Medical Imaging*, vol. 5030, pp. 226-234, 2003.
- [85] M. L. Giger, K. Doi, and C. E. Metz, "Investigation of basic imaging properties in digital radiography. 2. Noise Wiener spectrum," *Medical Physics*, vol. 11, no. 6, pp. 797-805, 1984.
- [86] I. A. Cunningham, "Applied linear-systems theory," In *Handbook of Medical Imaging*, Washington: SPIE Press, 2000.
- [87] M. Z. Kabir, "Modeling of x-ray photoconductors for x-ray image detectors," PhD diss., University of Saskatchewan, 2005.
- [88] S. M. Arnab, & M. Z. Kabir, "Impact of Lubberts Effect on Amorphous Selenium Indirect Conversion Avalanche Detector for Medical X-Ray Imaging," *IEEE Transactions on Radiation and Plasma Medical Sciences*, vol. 1, no. 3, pp. 221-228, 2017.
- [89] A. R. Cowen, A. G. Davies, and M. U. Sivananthan, "The design and imaging characteristics of dynamic, solid-state, flat-panel x-ray image detectors for digital fluoroscopy and fluorography," *Clinical Radiology*, vol. 63, no. 10, pp. 1073-1085, 2008.
- [90] J. A. Rowlands and W. Zhao, "Towards a digital radiology roadmap," *ECS Transactions*, vol. 54, no. 1, pp. 293-303, 2013.
- [91] M. Z. Kabir, M. W. Rahman, and W. Y. Shen, "Modelling of detective quantum efficiency of direct conversion x-ray imaging detectors incorporating charge carrier trapping and K-fluorescence," *IET Circuits, Devices & Systems*, vol. 5, no. 3, pp. 222-231, 2011.
- [92] M. Z. Kabir and S. O. Kasap, "DQE of photoconductive x-ray image detectors: application to a-Se," *Journal of Physics D: Applied Physics*, vol. 35, no. 21, pp. 2735-2743, 2002.

- [93] K. S. Karim, Y. K. Vygranenko, D. A. Striakhilev, A. Nathan, S. Germann, J. A. Rowlands, G. Belev, C. Koughia, R. Johanson, and S. O. Kasap, "Active pixel image sensor for large-area medical imaging," *Proc. SPIE Medical Imaging*, vol. 5030, pp. 38-47, 2003.
- [94] C. D. Arvanitis, S. E. Bohndiek, G. Royle, A. Blue, H. X Liang, A. Clark, M. Prydderch, R. Turchetta, and R. Speller, "Empirical electro-optical and x-ray performance evaluation of CMOS active pixel sensors for low dose, high resolution x-ray medical imaging," *Medical Physics*, vol. 34, no. 12, pp. 4612-4612, 2007.
- [95] M. Farrier, T. G. Achterkirchen, G. P. Weckler, and A. Mrozack, "Very large area CMOS active-pixel sensor for digital radiography," *IEEE Transactions on Electron Devices*, vol. 56, no. 11, pp. 2623-2631, 2009.
- [96] A. C. Konstantinidis, M. B. Szafraniec, R. D. Speller, and A. Olivo, "The Dexela 2923 CMOS X-ray detector: A flat panel detector based on CMOS active pixel sensors for medical imaging applications," *Nuclear Instruments and Methods in Physics Research Section A: Accelerators, Spectrometers, Detectors and Associated Equipment*, vol. 689, pp. 12-21, 2012.
- [97] M. M. Wronski and J. A. Rowlands, "Direct-conversion flat-panel imager with avalanche gain: feasibility investigation for HARP-AMFPI," *Medical Physics*, vol. 35, no. 12, pp. 5207-5218, 2008.
- [98] G. Hajdok, J. J. Battista, and I. A. Cunningham, "Fundamental x-ray interaction limits in diagnostic imaging detectors: Spatial resolution," *Medical Physics*, vol. 35, no. 7, pp. 3180-3193, 2008.
- [99] A. Badano, R. M. Gagne, B. D. Gallas, R. J. Jennings, J. S. Boswell, and K. J. Myers, "Lubberts effect in columnar phosphors," *Medical Physics*, vol. 31, no. 11, pp. 3122-3131, 2004.
- [100] R. V. Metter and M. Rabbani, "An application of multivariate moment-generating functions to the analysis of signal and noise propagation in radiographic screen-film systems," *Medical Physics*, vol. 17, no. 1, pp. 65-71, 1990.
- [101] R. K. Swank, "Calculation of modulation transfer functions of x-ray fluorescent screens," *Applied Optics*, vol. 12, no. 8, pp. 1865-1870, 1973.
- [102] W. Zhao, D. Li, A. Reznik, B. J. Lui, D. C. Hunt, J. A. Rowlands, Y. Ohkawa, and K. Tanioka, "Indirect flat-panel detector with avalanche gain: fundamental feasibility investigation for SHARP-AMFPI (scintillator HARP active matrix flat panel imager)," *Medical Physics*, vol. 32, no. 9, pp. 2954-2966, 2005.

- [103] S. Suryanarayanan, A. Karellas, S. Vedantham, and I. Sechopoulos, "Theoretical analysis of high-resolution digital mammography," *Physics in Medicine and Biology*, vol. 51, no. 12, pp. 3041-3055, 2006.
- [104] W. Zhao, G. Ristic, and J. A. Rowlands, "X-ray imaging performance of structured cesium iodide scintillators," *Medical Physics*, vol. 31, no. 9, pp. 2594-2605, 2004.
- [105] J. R. Scheuermann, A. H. Goldan, O. Tousignant, S. Léveillé, and W. Zhao, "Development of solid-state avalanche amorphous selenium for medical imaging," *Medical Physics*, vol. 42, no. 3, pp. 1223-1226, 2015.
- [106] M. Wronski, W. Zhao, K. Tanioka, G. DeCrescenzo, and J. A. Rowlands, "Scintillator high-gain avalanche rushing photoconductor active-matrix flat panel imager: Zero-spatial frequency x-ray imaging properties of the solid-state SHARP sensor structure," *Medical Physics*, vol. 39, no. 11, pp. 7102-7109, 2012.
- [107] I. A. Cunningham, "Linear-Systems modeling of parallel cascaded stochastic processes: The NPS of radiographic screens with reabsorption of characteristic X radiation," *Medical Imaging 1998: Physics of Medical Imaging*, vol. 3336, pp. 220-230, 1998.
- [108] M. Rabbani, R. Shaw, and R. V. Metter, "Detective quantum efficiency of imaging systems with amplifying and scattering mechanisms," *Journal of the Optical Society of America*, vol. 4, no. 5, pp. 895-901, 1987.
- [109] D. M. Pai and R. C. Enck, "Onsager mechanism of photogeneration in amorphous selenium," *Physical Review B*, vol. 11, no. 12, pp. 5163-5174, 1975.
- [110] N. Hijazi and M. Z. Kabir, "Mechanisms of charge photogeneration in amorphous selenium under high electric fields," *Journal of Materials Science: Materials in Electronics*, vol. 27, no. 7, pp. 7534-7539, 2015.
- [111] W. Sockley, "Problems related to p-n junction in silicon," *Solid-State Electronics*, vol. 2, no. 2, pp. 81-121, 1961.
- [112] W. Que and J. A. Rowlands, "X-ray imaging using amorphous selenium: Inherent spatial resolution," *Medical Physics*, vol. 22, no. 4, pp. 365-374, 1995.
- [113] A. Ganguly, S. Rudin, D. R. Bednarek, and K. R. Hoffmann, "Microangiography for neurovascular Imaging, part II: Cascade Model Analysis," *Medical Physics*, vol. 30, no. 11, pp. 3029-3039, 2003.
- [114] D. R. Dance and G. J. Day, "Escape probabilities for fluorescent x-rays," *Physics in Medicine and Biology*, vol. 30, no. 3, pp. 259-262, 1985.

- [115] S. M. Arnab and M. Z. Kabir, "Impact of charge carrier trapping on amorphous selenium direct conversion avalanche X-ray detectors," *Journal of Applied Physics*, vol. 122, no. 13, pp. 134502-8, 2017.
- [116] J. R. Scheuermann, Y. Miranda, H. Liu, and W. Zhao, "Charge transport model in solid-state avalanche amorphous selenium and defect suppression design," *Journal of Applied Physics*, vol. 119, no. 2, pp. 024508-8, 2016.
- [117] S. Kasap, C. Koughia, J. Berashevich, R. Johanson, and A. Reznik, "Charge transport in pure and stabilized amorphous selenium: re-examination of the density of states distribution in the mobility gap and the role of defects," *Journal of Materials Science: Materials in Electronics*, vol. 26, no. 7, pp. 4644-4658, 2015.
- [118] D. C. Hunt, K. Tanioka, & J. A. Rowlands, "X-ray imaging using avalanche multiplication in amorphous selenium: Investigation of depth dependent avalanche noise," *Medical Physics*, vol. 34, no. 12, pp. 4654-4663, 2007.
- [119] J. G. Mainprize, D. C. Hunt, and M. J. Yaffe, "Direct conversion detectors: The effect of incomplete charge collection on detective quantum efficiency," *Medical Physics*, vol. 29, no. 6, pp. 976-990, 2002.
- [120] M. Z. Kabir and S. O. Kasap, "Modulation transfer function of photoconductive x-ray image detectors: effects of charge carrier trapping," *Journal of Physics D: Applied Physics*, vol. 36, no. 19, pp. 2352-2358, 2003.
- [121] J. R. Scheuermann, A. H. Goldan, O. Tousignant, S. Léveillé, and W. Zhao, "Development of solid-state avalanche amorphous selenium for medical imaging," *Medical Physics*, vol. 42, no. 3, pp. 1223-1226, 2015.
- [122] D. L. Lee, "Selenium detector with a grid for selenium charge gain," *Medical Imaging 2005: Physics of Medical Imaging*, vol. 5745, pp. 216-222, 2005.
- [123] Y. Giomataris, P. Rebourgeard, J. P. Robert, and G. Charpak, "MICROMEGAS: a high-granularity position-sensitive gaseous detector for high particle-flux environments," *Nuclear Instruments and Methods in Physics Research Section A: Accelerators, Spectrometers, Detectors and Associated Equipment*, vol. 376, no. 1, pp. 29-35, 1996.
- [124] M. M. Wronski and J. A. Rowlands, "Direct-conversion flat-panel imager with avalanche gain: Feasibility investigation for HARP-AMFPI," *Medical Physics*, vol. 35, no. 12, pp. 5207-5218, 2008.

- [125] O. Maslyanchuk, M. Solovan, V. Brus, V. Kulchynsky, P. Maryanchuk, I. Fodchuk, et al., "Capabilities of CdTe-based Detectors with MoO_x Contacts for Detection of X- and γ -radiation," *IEEE Transactions on Nuclear Science*, vol. 64, no. 5, pp. 1168-1172, 2017.
- [126] K. Kanaya and S. Okayama, "Penetration and energy-loss theory of electrons in solid targets," *Journal of Physics D: Applied Physics*, vol. 5, no. 1, pp. 43-58, 1972.
- [127] S. Ramo, "Currents induced by electron motion," *Proceedings of the IRE*, vol. 27, no. 9, pp. 584-585, 1939.
- [128] A. Göök, F. J. Hamsch, A. Oberstedt, and S. Oberstedt, "Application of the Shockley–Ramo theorem on the grid inefficiency of Frisch grid ionization chambers," *Nuclear Instruments and Methods in Physics Research Section A: Accelerators, Spectrometers, Detectors and Associated Equipment*, vol. 664, no. 1, pp. 289-293, 2012.
- [129] W. Zhao, D. Li, A. Reznik, B. J. M. Lui, D. C. Hunt, J. A. Rowlands and K. Tanioka, "Indirect flat-panel detector with avalanche gain: fundamental feasibility investigation for SHARP-AMFPI (scintillator HARP active matrix flat panel imager)," *Medical Physics*, vol. 32, no. 9, pp. 2954-2966, 2005.
- [130] R. J. McIntyre, "Multiplication noise in uniform avalanche diodes," *IEEE Transactions on Electron Devices*, vol. 13, no. 1, pp. 164-168, 1966.
- [131] S. M. Arnab and M. Z. Kabir, "A Novel Amorphous Selenium Direct Conversion Avalanche Detector Structure for Low Dose Medical X-ray Imaging," *IEEE Transactions on Radiation and Plasma Medical Sciences* – accepted, 2019.
- [132] B. Zhao, and W. Zhao, "Imaging performance of an amorphous selenium digital mammography detector in a breast tomosynthesis system," *Medical Physics*, vol. 35, no. 5, pp. 1978-1987, 2008.
- [133] A. Sarno, M. Masi, N. Antonelli, F. D. Lillo, G. Mettivier, R. Castriconi, P. Russo, "Dose Volume Distribution in Digital Breast Tomosynthesis: A Phantom Study," *IEEE Transactions on Radio and Plasma Medical Sciences*, vol. 1, no. 4, pp. 322-328, 2017.
- [134] E. Meyblum, F. Gardavaud, T. H. Dao, V. Fournier, P. Beaussart, F. Pigneur, L. Baranes, A. Rahmouni, A. Luciani, "Breast tomosynthesis: dosimetry and image quality assessment on phantom," *Diagnostic and Interventional Imaging*, vol. 96, no. 9, pp. 931-939, 2015
- [135] A. Parsafar, C. C. Scott, A. El-Falou, P. M. Levine, K. S. Karim, "Direct-Conversion CMOS X-Ray Imager with 5.6 μm \times 6.25 μm Pixels," *IEEE Electron Device Letters*, vol. 36, no. 5, pp. 481-483, 2015.

- [136] J. Bogaerts, D. Bart, M. Guy, and U. Dirk, "Total dose and displacement damage effects in a radiation-hardened CMOS APS," *IEEE Transactions on Electron Devices*, vol. 50, no. 1, pp. 84-90, 2003.
- [137] M. Z. Kabir, "Effects of charge carrier trapping on polycrystalline PbO x-ray imaging detectors," *Journal of Applied Physics*, vol. 104, no. 7, pp. 074506-9, 2008.
- [138] H. Jiang, Q. Zhao, L. E. Antonuk, Y. El-Mohri, T. Gupta, "Development of active matrix flat panel imagers incorporating thin layers of polycrystalline HgI₂ for mammographic x-ray imaging," *Physics in Medicine & Biology*, vol. 58, no. 3, pp. 703-714, 2013.
- [139] Y. Kim, K. H. Kim, D. Y. Son, D. N. Jeong, J. Y. Seo, Y. S. Choi, I. T. Han, S. Y. Lee, N. G. Park, "Printable organometallic perovskite enables large-area, low-dose x-ray imaging," *Nature*, vol. 550, no. 7674, pp. 88-91, 2017.
- [140] G. Juška and K. Arlauskas, "Impact ionization and mobilities of charge carriers at high electric fields in amorphous selenium," *Physica Status Solidi (A)*, vol. 59, no. 1, pp. 389-393, 1980.
- [141] S. Abbaszadeh, N. Allec, K. Wang, and K. S. Karim, "Low dark-current amorphous selenium metal–semiconductor–metal photodetector," *IEEE transactions on Electron devices*, vol. 32, no. 9, pp. 1263-1265, 2011.
- [142] G. Belev, S. Kasap, J. A. Rowlands, D. Hunter, and M. Yaffe. "Dependence of the electrical properties of stabilized a-Se on the preparation conditions and the development of a double layer X-ray detector structure." *Current Applied Physics*, vol. 8, no. 3-4, pp. 383-387, 2008.
- [143] "Semiconductor Module User's Guide, version 5.3", COMSOL, Inc, www.comsol.com
- [144] S. M. Sze, *Physics of Semiconductor Devices*, New York: Wiley, 1981.
- [145] S. Siddiquee and M. Z. Kabir, "Modeling of photocurrent and lag signals in amorphous selenium x-ray detectors," *Journal of Vacuum Science & Technology A: Vacuum, Surfaces, and Films*, vol. 33, no. 4, pp. 041514-7, 2015.
- [146] M. Z. Kabir, S. O. Kasap, W. Zhao, and J. A. Rowlands. "Direct conversion x-ray sensors: Sensitivity, DQE and MTF," *IEE Proceedings-Circuits, Devices and Systems*, vol. 150, no. 4, pp. 258-266, 2003.
- [147] M. Z. Kabir, L. Chowdhury, G. DeCrescenzo, O. Tousignant, S. O. Kasap, and J. A. Rowlands, "Effect of repeated x-ray exposure on the resolution of amorphous selenium based x-ray imagers," *Medical Physics*, vol. 37, no. 3, pp. 1339-1349, 2010.

- [148] M. Z. Kabir and S.-A. Imam, "Determination of deep trapping states of the hole blocking layer in multilayer amorphous selenium X-ray detectors using transient dark current analysis," *Canadian Journal of Physics*, vol. 92, no. 7/8, pp. 641-644, 2014.
- [149] M. Abkowitz, "Density of States in a-Se from Combined Analysis of Xerographic Potentials and Transient Transport Data," *Philosophical Magazine Letters*, vol. 58, no. 1, pp. 53-57, 1988.
- [150] K. Koughia, Z. Shakoor, S. O. Kasap, and J. M. Marshall, "Density of localized electronic states in a-Se from electron time-of-flight photocurrent measurements," *Journal of Applied Physics*, vol. 97, no. 3, pp. 033706-11, 2005.
- [151] M. Z. Kabir and N. Hijazi, "Temperature and field dependent effective hole mobility and impact ionization at extremely high fields in amorphous selenium," *Applied Physics Letters*, vol. 104, no. 19, pp. 192103-4, 2014.
- [152] B. Zhao and W. Zhao, "Three-dimensional linear system analysis for breast tomosynthesis," *Medical Physics*, vol. 35, no. 12, pp. 5219-5232, 2008.
- [153] M. F. Stone, W. Zhao, B. V. Jacak, P. O'connor, B. Yu, and P. Rehak, "The x-ray sensitivity of amorphous selenium for mammography," *Medical Physics*, vol. 29, no. 3, pp. 319-324, 2002.
- [154] R. M. Manjeshwar and D. L. Wilson, "Optimization of detector pixel size for interventional x-ray fluoroscopy," *Medical Imaging 2001: Image Perception and Performance*, vol. 4324, pp. 23-34, 2001.